# AIRFOIL AERODYNAMIC PERFORMANCE ENHANCEMENT BY MANIPULATION OF TRAPPED VORTICITY CONCENTRATIONS USING ACTIVE FLOW CONTROL

A Dissertation
Presented to
The Academic Faculty

by

Michael Edward DeSalvo

In Partial Fulfillment
of the Requirements for the Degree
Doctor of Philosophy in Mechanical Engineering
in the George W. Woodruff School of Mechanical Engineering

Georgia Institute of Technology
August 2015

# AIRFOIL AERODYNAMIC PERFORMANCE ENHANCEMENT BY MANIPULATION OF TRAPPED VORTICITY CONCENTRATIONS USING ACTIVE FLOW CONTROL

Approved by:

| | |
|---|---|
| Dr. Ari Glezer, Advisor<br>School of Mechanical Engineering<br>*Georgia Institute of Technology* | Dr. Marilyn Smith<br>School of Aerospace Engineering<br>*Georgia Institute of Technology* |
| Dr. Marc Smith<br>School of Mechanical Engineering<br>*Georgia Institute of Technology* | Dr. Mark Costello<br>School of Aerospace Engineering<br>*Georgia Institute of Technology* |
| Dr. Bojan Vukasinovic<br>School of Mechanical Engineering<br>*Georgia Institute of Technology* | Dr. Edward Whalen<br>*The Boeing Company, Hazelwood MO* |

Date Approved: May 21, 2015

# ACKNOWLEDGEMENTS

I would like to gratefully acknowledge the people who have supported me in during my graduate work at the Woodruff School of Mechanical Engineering at Georgia Tech.

To begin with, I would like to give thanks to my advisor, Prof. Ari Glezer, director of the Fluid Mechanics Research Lab (FMRL), with whom I have worked since beginning my studies at Georgia Tech. It is because of Prof. Glezer's ongoing leadership efforts that the FMRL has been able to consistently achieve accomplishments that are the embodiment of scientific and technical excellence, leading to the success of both myself as well as my colleagues. I would also like to thank Drs. Bill Bower and Edward Whalen from The Boeing Company, who have fostered a mutually beneficial relationship with the FMRL for many years and generously supported several of the FMRL's research projects in which I was involved. I would also like to thank Dr. Whalen specifically for serving as a member of my Ph.D Committee. In addition, I would like to acknowledge Prof. Marc Smith and Dr. Bojan Vukasinovic from the School of Mechanical Engineering and Profs. Marilyn Smith and Mark Costello from the School of Aerospace Engineering for taking time out of their schedules to serve as members of my Ph.D. Committee.

Acknowledgements also go to the research engineers and students in the FMRL that I have gotten to know and work with over the years. I would particularly like to thank Mr. John Culp for his efforts in designing, implementing and maintaining the computer systems used in my research, as well as for his assistance in design and programming. I have also taken considerable inspiration from his interest in all things mechanical, electrical and computational. I would like to thank the FMRL members who preceded me, such as Miki Amitay and Andrew Honohan, as well as Dr. Vukasinovic and Tom Crittenden, both of whom remain with the FMRL to this day, all of whose prior efforts in development of laboratory techniques and equipment and in research have effectively served as a starting point for my own efforts. I am also glad to have been around past FMRL members such as Chris Rinehart, Dan Brzozowski and Dave Garth, who have been great friends and have led me to develop newfound interests.

I would also like to acknowledge the staff at Georgia Tech Research Institute Machine Services, particularly its management Dennis Denney, Dennis Brown and Jeff Wilkie, for their extensive contributions of precision machine work to my research. I am especially appreciative of how the shop successfully produced quality machine work on schedules that could be especially tight at times.

Finally, I would like to acknowledge the people from outside of Georgia Tech who have been a part of my life over the years. I am grateful for my family, especially my parents, because of all they have done for me over the years, especially because of the guidance and wisdom I have received from them, and for my brother, because it has been very rewarding for me to witness his successful progression through life and career. I am also glad for all of the various friends I have known over the years, who have brought so much to my life in so many different ways and of whom I will always be appreciative.

# TABLE OF CONTENTS

Page

# LIST OF TABLES

# LIST OF FIGURES

# LIST OF SYMBOLS

$\alpha$ = Angle of attack

$\beta$ = Falkner-Skan boundary layer parameter

$c$ = Airfoil chord

$C_\mathrm{L}$ = Three-dimensional (3-D) lift coefficient = $L / (0.5\rho U_\infty^2 cs)$

$C_\mathrm{l}$ = Two-dimensional (2-D) lift coefficient = $l / (0.5\rho U_\infty^2 c)$

$C_\mathrm{D}$ = 3-D drag coefficient = $\mathrm{D} / (0.5\rho U_\infty^2 cs)$

$C_\mathrm{d}$ = 2-D drag coefficient = $d / (0.5\rho U_\infty^2 c)$

$C_\mathrm{dp}$ = Pressure drag coefficient = $d_\mathrm{p} / (0.5\rho U_\infty^2 c)$

$C_\mathrm{df}$ = Wall friction drag coefficient = $d_\mathrm{f} / (0.5\rho U_\infty^2 c)$

$C_\mathrm{f}$ = Wall friction coefficient scaled by freestream speed = $2(u_* / U_\infty)^2$

$C_\mathrm{f}^*$ = Wall friction coefficient scaled by boundary layer edge speed = $2(u_* / U_\mathrm{e})^2$

$C_\mathrm{M}$ = 3-D spanwise pitching moment coefficient (about $c/4$) = $M / (0.5\rho U_\infty^2 c^2 s)$

$C_\mathrm{m}$ = 2-D spanwise pitching moment coefficient (about $c/4$) = $m / (0.5\rho U_\infty^2 c^2)$

$C_\mu$ = Momentum coefficient = $(0.5\rho u_\mathrm{j}^2 h_\mathrm{act}) / (0.5\rho U_\infty^2 c)$

$\hat{C}_\mathrm{l}$ = Change in lift coefficient scaled by baseline value = $\Delta C_\mathrm{l}/C_\mathrm{l0}$

$\hat{C}_\mathrm{dp}$ = Change in pressure drag coefficient scaled by baseline value = $\Delta C_\mathrm{dp}/C_\mathrm{dp0}$

$C_\mathrm{p}$ = Pressure coefficient

$D$ = Airfoil drag

$d$ = Airfoil drag per unit span

$d_\mathrm{f}$ = Airfoil wall friction drag per unit span

$d_\mathrm{p}$ = Airfoil pressure drag per unit span

$\delta$ = Flap deflection

$\delta^*$ = Boundary layer displacement thickness

$\Delta C_{\mathrm{dp}}$ = Change in pressure drag coefficient

$\Delta C_{\mathrm{l}}$ = Change in lift coefficient

$\Delta C_{\mathrm{m}}$ = Change in spanwise pitching moment coefficient

$f$ = Frequency

$f_{\mathrm{p}}$ = Force due to static pressure

$\theta^*$ = Boundary layer momentum thickness

$\gamma$ = Cross-stream gap

$\Gamma$ = Circulation

$\Gamma^*$ = Scaled circulation = $2\Gamma/(U_\infty c)$

$H$ = Boundary layer shape factor

$h$ = Height

$k$ = Number of adjacent active actuator jets per spanwise wavelength

$L$ = Control volume boundary; characteristic advection length; airfoil lift

$l$ = Airfoil lift per unit span; control volume boundary coordinate

$\ell$ = Coordinate tangent to wall

$\lambda$ = Spanwise wavelength

$M$ = Airfoil pitching moment

$m$ = Airfoil pitching moment per unit span

$\dot{m}$ = Mass flux

$n$ = Number of actuator jets per spanwise wavelength

$\hat{n}$ = Normal vector to control volume boundary

$\nu$ = Kinematic viscosity

$\dot{p}$ = Momentum flux

$\rho$ = Air density

$Re$ = Reynolds number = $U_\infty c/\nu$

$S$ = Stokes number = $h_{\mathrm{act}}(2\pi f_{\mathrm{act}} / \nu)^{0.5}$

$s$ = Airfoil span

$St$ = Strouhal number = $f_{\mathrm{act}} \cdot c/U_\infty$

$t$ = Time

$\tau$ = Convective timescale = $c/U_\infty$

$u$ = Speed; streamwise velocity

$u'$ = Streamwise turbulent fluctuation

$u_*$ = Friction velocity = $[\nu\ (\partial u / \partial y)_{\mathrm{w}}]^{1/2}$

$U_\infty$ = Free stream speed

$v$ = Cross-stream velocity

$\vec{v}$ = Velocity vector

$w$ = Spanwise velocity

$\omega$ = Vorticity

$x$ = Streamwise distance from airfoil leading edge

$y$ = Cross-stream distance from airfoil wall

$y_+$ = Wall length scale = $yu_*/\upsilon$

$z$ = Spanwise distance from spanwise reference location

Subscripts

$0$ = baseline

$a$ = actuated

$act$ = actuator

$c$ = chord

$conv$ = convective

$e$ = edge, boundary layer

$f$ = flap

$in$ = inlet

$j$ = jet

$L$ = left

$l$ = lower

$mod$ = modulation

$out$ = outlet

$ref$ = reference

$p$ = pressure surface

$R$ = right

$s$ = suction surface

$u$ = unactuated, upper

$w$ = wall

# SUMMARY

The mechanisms of aerodynamic flow control over lifting surfaces in which global, large-scale changes in aerodynamic characteristics are engendered by momentum injection across the flow boundary using surface-mounted fluidic actuators are investigated in wind tunnel experiments. The utility of this approach for aerodynamic flow control in the absence of moving control surfaces is demonstrated in the limits of fully-attached and separated cross flows. In the present investigations, the actuation frequency is selected to be sufficiently high to be decoupled from global flow instabilities. The changes in the aerodynamic loads are attained by leveraging the generation and regulation of "trapped" vorticity concentrations near the surface to alter its aerodynamic shape. Diagnostics include measurements of the aerodynamic forces and moments and of distributions of static pressure on the airfoil surface, and particle image velocimetry (PIV) of the flow over the airfoil and in its near wake. The present investigations have demonstrated that when the base flow is fully attached (at low angle of attack) fluidic actuation alters the aerodynamic characteristics of an airfoil leading to controlled changes in lift and pitching moment along with a significant reduction in form drag. The effectiveness of actuation for mitigation of the adverse effects of separation is demonstrated on a high-lift flap system. It is anticipated that flow control augmentation of the performance of current and future flight platforms will ultimately enable significant mechanical simplification with savings in both weight and maintenance costs.

# CHAPTER 1

# INTRODUCTION

The aerodynamic characteristics of lifting surfaces, and thereby the flight characteristics of air vehicles, have traditionally been controlled using sophisticated mechanical control surfaces that are actuated pneumatically or electromechanically. However, the utilization of such control surfaces poses significant penalties in terms of complexity, weight, maintenance costs and aerodynamic performance limitations. In recent decades, much attention has focused on the use of active flow control (Gad-el-Hak 2001), in which a flow is manipulated by one of a variety of methodologies without altering the flow boundary in order to achieve desired favorable changes such as mitigation of flow separation and alteration of boundary layer characteristics. By applying active flow control to aerodynamic flows, significant improvements in aerodynamic performance can be achieved, such as increased lift and reduced drag, that are beyond what is possible for conventional systems.

The present dissertation focuses on the application of novel, fluidic-based flow control methodologies in the absence of mechanical control surfaces for affecting aerodynamic control at two limits of the flight envelope, namely, when the flow over the lifting surfaces is attached, and in the presence of separation or stall. It is shown in Chapters 3-6 how active flow control enables the aerodynamic characteristics of an airfoil at low angle of attack (e.g., as for an aircraft in cruise configuration), to be altered fluidically (i.e. without moving control surfaces), leading to controlled changes in lift and pitching moment along with a significant reduction in form drag. Investigations of the application of aerodynamic flow control to the separated flow on a high-lift flap system is demonstrated in Chapters 7-9, by using fluidic actuation to overcome stall and loss of lift. It is anticipated that flow control augmentation of the performance of existing flap hardware will ultimately enable significant mechanical simplification with savings in both weight and maintenance costs.

### *1.1. Aerodynamic Flow Control of Separation on Simple Airfoils*

Strategies for active flow control over lifting surfaces with the objective of improving aerodynamic performance have primarily focused on mitigation of partial or complete flow separation over stalled wing sections. The separating shear layer is typically dominated by a strong coupling to the instability of the near wake that leads to the nominally time-periodic formation and shedding of large-scale vortices (e.g., Wu et al. 1998). Therefore, attempts to manipulate and ultimately control separation have mostly focused on coupling of flow control actuation to the narrow-band receptivity of a near-wake instability that is manifested by the formation and shedding of large-scale vortical structures. Since the characteristic scale of the wake is commensurate with the scale of the separated flow domain, the actuation Strouhal number $St_{\mathrm{act}} = L/u_c\, t_{\mathrm{act}}$ is O(1) where the actuation period $t_{\mathrm{act}}$ nominally corresponds to the convective time scale $\tau_{\mathrm{conv}}$ ($L$ and $u_c$ are the characteristic advection length and speed, respectively). Time-periodic actuation has been applied since the early 1980s using a variety of actuation approaches including acoustic (Ahuja & Burrin 1984), pulsating jets (Hsiao et al. 1990, and Seifert et al. 1993) and synthetic jets (Greenblatt & Wygnanski 2001, Margalit et al. 2005, Gilarranz et al. 2005, Smith, et al. 2006, Shmilovich & Yadlin 2006, Raju et al. 2008, and You et al. 2008). Because of the coupling to the near wake instability, the actuation typically leads to the formation of vortical structures that scale with the length of the separated flow domain. The ensuing changes in the rate of entrainment result in a Coanda-like deflection of the vortical structures towards the surface (Amitay & Glezer 2002, Glezer et al. 2005, and Greenblatt 2006).

Quasi-steady modification of the apparent aerodynamic shape of the surface by localized concentrations of trapped vorticity can also be effected by controlled interactions between active flow control actuators and the cross flow when the actuation period is at least an order of magnitude *shorter* than the relevant time scales of the base flow (e.g., $\tau_{\mathrm{conv}}$), and therefore effectively decoupled from its global instabilities (e.g., Glezer & Amitay 2002 and Glezer et al. 2005). The interaction between a surface-mounted synthetic jet and the local cross flow can lead to the formation of a quasi-steady concentration of trapped vorticity where the jet continuously regulates a balance between bound and shed vorticity (Smith & Glezer 1998, Honohan et al. 2000, Mittal & Rampunggoon 2002, and Honohan 2003). The cross stream scale of the trapped vorticity structure can exceed the local boundary layer thickness, and typically features a streamwise scale of several actuation wavelengths. When the trapped vorticity concentrations are formed upstream of a separating flow, the resulting alteration of the local pressure gradient can result in complete or partial bypass (or suppression) of separation (Amitay et al. 2001, Glezer et al. 2005, Timor et al. 2004, Rehman & Kontis 2006, and Watson et al. 2007). Control has been attained at actuation frequencies that are at least an order of magnitude higher than the characteristic flow frequency [$St_{\mathrm{act}} \sim O(10)$] and therefore can be decoupled from global flow instabilities (e.g., Wu et al. 1998).

Local concentrations of trapped vorticity (or separation bubbles) in which active flow control actuation is used to regulate the creation and streamwise advection and shedding of vorticity near the airfoil surface can also be used to vary the aerodynamic characteristics of lifting surfaces. Modification of the "apparent shape" of lifting surfaces with concentrations of trapped vorticity to achieve changes in the streamwise pressure distribution has been the subject of a substantial body of work since the 1940s. Trapped vortices on various scales relative to the chord of the airfoil have been engendered by inducing local closed recirculation bubbles using devices such as passive obstacles, conventional jets, cavities, and split flaps (Perkins & Hazen 1953, Ringleb 1960, Hurley 1960, and Chang 1976). The creation and manipulation of trapped vorticity concentrations for aerodynamic control of high-lift systems and configurations without large-scale separation is discussed in further detail in §1.2 and §1.3, respectively.

## *1.2. Aerodynamic Flow Control with Large-Scale Separation: High Lift*

The aerodynamic performance of a deployed trailing-edge flap on a high-lift airfoil is limited by large-scale separation of the flow over the suction surface. Active flow control has the potential to substantially enhance the performance of such high-lift systems, leading to significant improvements in aircraft performance with simplified high-lift mechanics. A study conducted in 1999 by Boeing and NASA (McLean et al. 1999) estimates that, among other things, a simplified high-lift system using active flow control can reduce the empty weight of a 737-class aircraft by 3.3%. This weight reduction, along with the aerodynamic advantages of a simplified high-lift design, such as the removal of fairings required for the external mechanisms of conventional high-lift systems, equate to a best-case cruise drag reduction of 3.2%. The authors also conclude that a further study is required to define the aerodynamic performance of high-lift systems using active flow control. Gomes et al. (2006) have concluded that it is possible to design a practical active-flow-control-enhanced high-lift system based on synthetic jets, and that the application of active flow control to the trailing-edge flap would yield the greatest benefit to the aircraft as far as high-lift system application is concerned.

The aerodynamic effects associated with high-lift systems are discussed extensively by Smith (1975) with emphasis on the mechanisms through which multi-element airfoil systems (e.g., Fowler flap) achieve higher maximum lift than simple, single-element airfoils. The flow through a cross-stream gap between the flap and main body can mitigate the effects of adverse pressure gradients on the flap by accelerating and coupling to the boundary layer on the main body and by forming a "fresh" boundary layer on the flap. These effects reduce the extent of separation on the flap and lead to increased circulation and lift. However, since the implementation of these effects requires the use of complex mechanical hardware, it is desirable to consider alternate, active-flow-control based approaches through which comparable (or better) high-lift performance can be attained with significantly reduced complexity.

Multi-element high-lift systems equipped with flow control have been studied in a number of earlier investigations, demonstrating significant practical benefits such as increased lift. Carrannanto et al. (1998) investigated numerically the effects of a small passive obstruction placed within the cove between the flap and the main body of a two-element airfoil and showed a significant increase in $C_L$ ($\Delta C_L \sim 0.5$). Active flow control using a wide variety of actuation strategies has been implemented in a number of studies for improving high-lift performance. Ciobaca et al. (2013) investigated experimentally and numerically the effects of slot blowing (steady and pulsed) on a high-lift configuration of a 3-D commercial aircraft wing model and observed lift increments of up to $\Delta C_L \sim 0.3$. In a numerical simulation of zero-net-mass-flux actuation on a Fowler-type multi-element wing section with a leading edge slat, Shmilovich and Yadlin (2009) assessed the effects of actuation from ten different locations on all three elements and demonstrated lift increments on the order of $\Delta C_L \sim 1$ for some conditions. Khodadoust and Washburn (2007) employed blowing, suction and zero net mass flux actuation on a Fowler-type high-lift wind tunnel model and reported lift increments as high as $\Delta C_L = 0.9$ at $Re_c = 9 \cdot 10^6$. Time-periodic, alternate blowing and suction near the juncture of a flap and main airfoil was used by Schatz et al. (2004) to increase lift by $\Delta C_L \sim 0.4$ (at a flap angle of $\delta = 32°$). Crowther (2006) used an array of vectored (non-oscillating) circular jets near the juncture of a Fowler-type flap and the main airfoil element to generate streamwise vorticity as a fluidic means of increasing $C_L$. Similar studies of flap performance augmentation have been conducted experimentally by Nishri and Wygnanski (1998) and numerically by Shmilovich and Yadlin (2006) who demonstrate how the improvement of flow attachment on the flap increases suction over the main element, contributing to increased $C_L$. They find that with multiple chordwise injection points flow reattachment to the flap trailing edge can be achieved at high flap deflections, leading to near-inviscid lift levels.

The high-lift performance of multi-element airfoils has also been enhanced using active flow control based on synthetic jets. Smith et al. (2006) investigated the application of low-frequency [$St \sim O(1)$] active flow control to enhance the high-lift characteristics of a SSTOL aircraft. Using voice-coil type synthetic jets, they achieved the required landing and takeoff performance $\Delta C_L$ increments of 0.2 and 0.5, respectively, on an 11%, powered model of a SSTOL airplane. The model used a full-span slat and a simple flap deflected to 40º in the takeoff case and 50º in the landing case. In 2-D testing, a similar system using a slat and a flap deflected to 40º has achieved a 20-40% increase in $C_L$, depending on angle of attack, at $Re_c = 7.5 \cdot 10^5$ and a blowing ratio of 3.6. Nagib et al. (2006) have achieved comparable results using an externally driven synthetic jet actuator, demonstrating how $C_L$ can be increased up to 20% at $\delta = 40^\circ$ by manipulating the flow near the suction surface juncture between the main element of an airfoil and a deflected single-element flap. Investigations have demonstrated the utility of "high-frequency" [i.e., $St_{act} \sim O(10)$] actuation that is effectively decoupled from the global instabilities of the base flow for improving airfoil aerodynamic performance. Kim and Kim (2006) have shown in numerical simulations how synthetic jets operating at $St_{act}$ up to 5 on a NACA 23012 airfoil with a trailing edge flap can be used to mitigate separation and improve high lift performance.

The investigations of DeSalvo and Glezer (2010, 2011, 2014) showed how spanwise arrays of fluidic oscillators can induce flow attachment on a highly deflected flap ($\delta = 40°$), yielding $\Delta C_L$ as high as 1.4 at $Re_c = 6.7 \cdot 10^5$. A wide variety of configurations were tested with different actuator cavity and orifice geometries as well as both single and multiple actuator arrays. These investigations showed how trapped vorticity concentrations engendered by the fluidic oscillators reduce (or eliminate entirely) flow separation on the suction surface of the flap, leading to increased lift. In another study on performance improvement of a high-lift airfoil with a simple flap using active flow control, DeSalvo et al. (2012) employed an array of high frequency, i.e.

$St_{act} \sim O(10)$, synthetic jets at the juncture between the flap and the main element to attain a lift increment of up to $\Delta C_L = 0.82$ relative to the unactuated flow. The performance of an aircraft vertical tail was improved by Seele et al. (2013) who used an array of fluidic oscillators near the juncture between the rudder and the main element to increase maximum side force by up to 50% relative to baseline levels.

### *1.3. Aerodynamic Flow Control in Predominantly Attached Flows*

While actuation at the unstable frequencies of the near wake are primarily effective when the base flow is separated, the use of trapped vorticity for flow control can also be effective when large parts of the flow are attached, namely at low angles of attack (e.g., an aircraft in cruise conditions). Chatlynne et al. (2001) and Amitay et al. (2001) showed that the formation of a stationary trapped vortex downstream of a miniature [cross-stream scale $O(0.01c)$], surface-mounted passive obstruction on the suction surface near the leading edge can lead to a reduction in pressure drag that is comparable to the magnitude of the pressure drag of the baseline configuration with minimal lift penalty. The extent and strength of the trapped vortex could be controlled to some extent by varying the actuation amplitude and frequency of a synthetic jet that was placed downstream of the obstruction and emanated normal to the surface of the airfoil.

DeSalvo et al. (2002) and DeSalvo and Glezer (2004, 2005, 2006, 2007) demonstrated the utility of a miniature $O(0.01c)$ hybrid actuator that is integrated with a synthetic jet module for effecting controlled concentrations of trapped vorticity. The presence of the passive element is leveraged to drastically reduce the required actuation power compared to the use of a synthetic jet alone. The regulation of trapped vorticity was improved compared to earlier implementations (e.g., Amitay et al. 2001) by modifying the orientation of the jet relative to the obstruction so the jet issues in the downstream direction from an orifice a short distance below the downstream edge of the obstruction. The actuation changes the scale of the trapped vorticity in a manner that results in flow acceleration upstream of the actuator and pressure recovery immediately downstream. The effectiveness of this actuation approach was demonstrated for reduction in pressure drag with minimal impact on lift (DeSalvo and Glezer 2005) and for alteration of the pitching moment (DeSalvo and Glezer 2006, 2007) over a broad range of angles of attack ($2^o < \alpha < 10^o$). From the standpoint of aerodynamic flow control, both $l/d_\mathrm{p}$ and the pitching moment $C_\mathrm{m}$ can be continuously adjusted by varying the actuation momentum coefficient.

### *1.4. Active Flow Control Methodologies and Actuators*

Active flow control has been implemented using a wide variety of actuation methodologies, including steady and pulsed blowing, steady and pulsed suction, zero-net-mass-flux actuators and plasma flow control, as discussed in the review by Cattafesta and Sheplak (2011). One active flow control technology that is particularly useful for aerodynamic performance improvement is the synthetic jet (Glezer and Amitay 2002, Glezer 2011), a zero-net-mass-flux device that has been demonstrated in a wide variety of applications. Synthetic jets are formed by the advection and interaction of trains of discrete vortical structures that are engendered by actuators integrated in the flow boundary. The fluid that is necessary to form the vortices that synthesize the jet is supplied by intermittent suction between consecutive ejections through an orifice in the flow boundary and is driven by the motion of a diaphragm that is built into one of the walls of an otherwise sealed cavity below the surface. Because synthetic jets are formed entirely from the working fluid of the flow system in which they are deployed, they can transfer linear momentum to the flow system without net mass injection. The formation and evolution of isolated synthetic jets in the absence of a cross flow have been investigated experimentally and numerically with emphasis on the near field formation, evolution, and advection of vortices for plane jets (Smith & Glezer 1998, Rizzetta et al. 1999, Lee & Goldstein 2002, Yao et al. 2006, Kotapati et al. 2007) and for circular jets (Cater & Soria 2002, Shuster & Smith 2007).

In addition to other methods of flow control, e.g. steady blowing or suction, pulsed blowing or suction, and synthetic jets, it has also been demonstrated that self-oscillating jets produced by fluidic oscillators can be used for aerodynamic performance improvement. Self-oscillating fluidic devices, which were investigated extensively as early as the 1950s, can generate spatially and temporally oscillating jets (e.g., Viets et al. 1975). More recently, small-scale, high-frequency fluidic oscillators have been characterized in detail by Gregory et al. (2007). Due to their simple, compact design, the absence of moving parts, and their ability to produce high-momentum, unsteady jet flows these oscillators are attractive actuators for a number of flow control applications where high-pressure air supply is available. In earlier studies, fluidic oscillators have been used for various applications including diversion of high-temperature flows (Gokoglu et al. 2009), suppression of cavity oscillations (Raman et al. 1999) and download alleviation (Seele et al. 2009). The aerodynamic effects of fluidic oscillators have been studied on an airfoil at low angles of attack (Cerretelli et al. 2009) and a hump diffuser model representing the suction surface of an airfoil at high angle of attack (Cerretelli et al. 2009) demonstrating an increase in lift and suppression of trailing-edge separation. Woszidlo et al. (2010) used fluidic oscillators in various configurations on an airfoil with multiple flap segments to increase lift by up to $\Delta C_L = 1.4$.

### *1.5. Dissertation Research Questions*

Earlier studies have demonstrated that active flow control can be utilized to alter vorticity concentrations near the airfoil surface (§1.3) as well as to mitigate larger-scale separation (§§1.1 and 1.2), resulting in significant improvements in aerodynamic performance. In order to realize these improvements, the present dissertation addresses several research questions that will lead to a better understanding of the underlying mechanisms of flow control over a lifting surface in the absence and presence of flow separation. As shown by earlier investigators (e.g. Amitay et al. 2001), trapped vorticity concentrations can have a profound effect on the flow over aerodynamic surfaces. The first part of the present dissertation focuses on the use of flow control for exploiting the interactions between the cross flow and controlled vorticity concentrations for altering the aerodynamic characteristics when the base flow is fully attached. Specifically, the dissertation addresses the following topics:

- How the interaction of active flow control actuation with a trapped vorticity concentration leads to changes in the scale of the concentration,
- How varying the size and scale of *local* trapped vorticity concentrations alters the *global* flow characteristics,
- Improvement of the aerodynamic performance of a lifting surface by manipulation of the global flow using active flow control,

- Use of active flow control for aerodynamic control by manipulation of the global flow without moving control surfaces,
- Whether the aerodynamic effects of multiple controlled trapped vorticity concentrations can be effectively superposed, and
- Optimization of the active flow control to reduce the actuation authority required to achieve these aerodynamic effects.

To answer these questions, a series of experimental studies has been conducted into the application of active flow control to the flow over an airfoil at low angles of attack, in which the flow is predominantly attached. Active flow control is implemented using one or more synthetic jet actuators on the surface of the airfoil, each located upstream of a small passive obstruction having a characteristic scale of $O(0.01c)$. A concentration of trapped vorticity forms downstream of the obstruction, and the synthetic jet is used to manipulate the strength and streamwise extent of the trapped vortex. Doing so alters the flow around the entire airfoil, resulting in changes to the lift, drag and pitching moment which are assessed from measurements of the static pressure distribution around the airfoil. High-resolution particle image velocimetry (PIV) measurements on the airfoil are used to assess the effects of the presence and operation of the hybrid actuator on the local velocity field and associated vorticity concentrations. The flow field in the vicinity of actuators is characterized, along with the boundary layer around the airfoil and the near wake. An investigation is also conducted into increasing the effectiveness of the active flow control by coupling to an instability of the near wake of the airfoil.

The second part of the dissertation focuses on another aerodynamic flow regime, namely, the utilization of active flow control for controlling large-scale separation. Studies are conducted using an airfoil with a deployed high-lift flap (and a separated flow domain over the flap suction surface) to address the following topics:

- How the use of active flow control actuation near a large-scale separated flow domain in an aerodynamic flow results in mitigation (or bypass) of separation,
- How varying the scale of separation alters the global flow around the airfoil,
- The improvement in high-lift performance that results from changes in the global flow field,
- The relative effectiveness of various actuation technologies at improving high-lift performance, and
- The use of active flow control as an alternative to the bleed flows between elements of a multi-element high-lift system that are necessary for its proper function.

These questions are addressed by a series of experimental investigations into the application of active flow control to the separated flow that develops over the suction surface of an airfoil with a deployed high-lift system. Active flow control is implemented using spanwise arrays of fluidically oscillating jets and synthetic jets issuing tangentially to the local surface. The interaction of the actuator jets with the wall leads to the formation of concentrations of streamwise vorticity which result in improved flow attachment over the suction surface of the flap, reducing the size of (or eliminating entirely) the large-scale separation domain that is otherwise present and increasing lift substantially as a result. Measurements of static pressure distribution and of aerodynamic forces and moments, along with PIV measurements of the flow over the airfoil suction surface and in the near wake, are used to characterize the effects of active flow control on the flow along with the resulting aerodynamic effects.

Chapters 2 through 8 of the dissertation demonstrate how controlled manipulation of the aerodynamic loads on lifting surfaces can be achieved using active flow control. In the absence of large-scale separation, active flow control is used to substantially reduce drag (Chapter 3) and alter pitching moment (Chapter 4). By coupling the flow control actuation to an instability of the near wake (Chapter 5) the actuation authority required to alter the aerodynamic characteristics is reduced substantially. Continuous, bi-directional changes in the pitching moment are achieved by alternating operation of two active flow control actuators near the trailing edge (Chapter 6). Active flow control is also demonstrated on aerodynamic flows in the presence of large-scale separation. The scale of flow separation over the suction surface of a flap of a high-lift airfoil is reduced substantially using active flow control to engender a large lift increase (Chapter 7) and a detailed study of the associated mechanism is presented in Chapter 8. Active flow control is also used to improve high-lift performance by enhancing the interaction between the elements of a multi-element high-lift airfoil (Chapter 9). Finally, concluding remarks are included in Chapter 10.

# CHAPTER 2

# EXPERIMENTAL APPARATUS AND TECHNIQUES

The present dissertation focuses on experimental investigations of the mechanisms of aerodynamic flow control over lifting surfaces in the absence and presence of large-scale separation where spanwise arrays of surface-mounted fluidic actuators interact with the local cross flow. Investigations of aerodynamic flow control in the absence of large-scale separation are conducted through wind tunnel testing of a simple airfoil model at low angle of attack that is equipped with surface-mounted synthetic jet actuators. Aerodynamic flow control is also applied to two configurations that include large-scale separated flow domains, namely an airfoil with a deflected trailing-edge simple flap, and an airfoil with an extended Fowler flap (e.g. high-lift airfoil configurations). In these configurations, actuation is applied using both fluidic oscillators and synthetic jets. The effects of the actuation are investigated using measurements of static pressure distributions, hot wire anemometry and particle image velocimetry (PIV).

## *2.1. Aerodynamic Models and Wind Tunnel Testing*

Experiments on configurations without large-scale separation are conducted using an airfoil model with a cross section that is based on a commercial aircraft configuration having a maximum thickness of $0.108c$ at $x/c = 0.4$ (described in more detail in Bower et al. 2004) and containing an inflection point on the pressure surface near the trailing edge, as shown in Figure 2.1a. The model is of a swept airfoil with a uniform cross section and a sweep angle of 27.1°. The chord length in the streamwise direction is $c = 501$ mm and

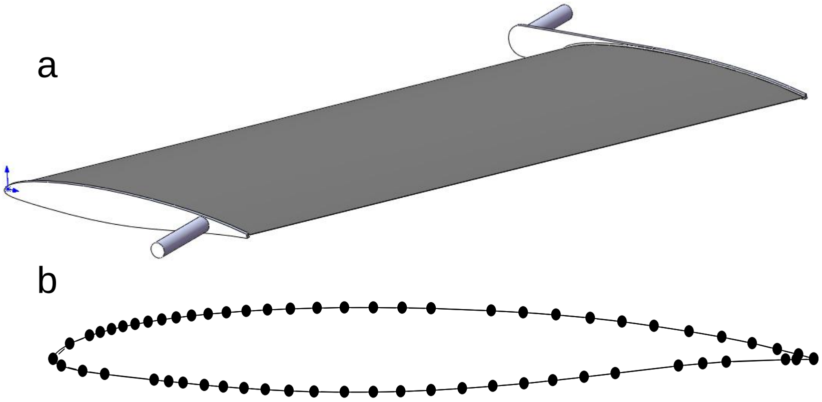

***Figure 2.1**. (a) Swept airfoil model and (b) centerline cross-section showing locations of pressure ports.*

the span is $s$ = 914 mm, corresponding to the width of the wind tunnel in which the model is installed.

Testing is conducted in the Woodruff Wind Tunnel at Georgia Tech, an open return wind tunnel having a square test section measuring 0.91 m on the side with a maximum speed of 42 m/s and a turbulence level less than 0.2%. The free stream speed is varied between $10 \leq U_\infty \leq 40$ m/s, with corresponding Reynolds numbers based on the airfoil chord of $3.3 \cdot 10^5 < Re_c < 1.3 \cdot 10^6$. Movable surfaces on opposing walls of the test section above and below the model can be adjusted to ensure uniform streamwise pressure. The model is attached to a pair of coaxial mounting holes in the side walls of the wind tunnel using pegs mounted to the end plates of the model. Angle of attack ($\alpha$) is adjusted by rotating the model about the axis of the mounting holes and is measured using a digital inclinometer with accuracy of $\pm 0.05°$ that is attached to the peg parallel to the airfoil chord line. The model is equipped with an array of 80 pressure ports located on the spanwise center line, the locations of which are shown in Figure 2.1b and listed numerically in Appendix A.

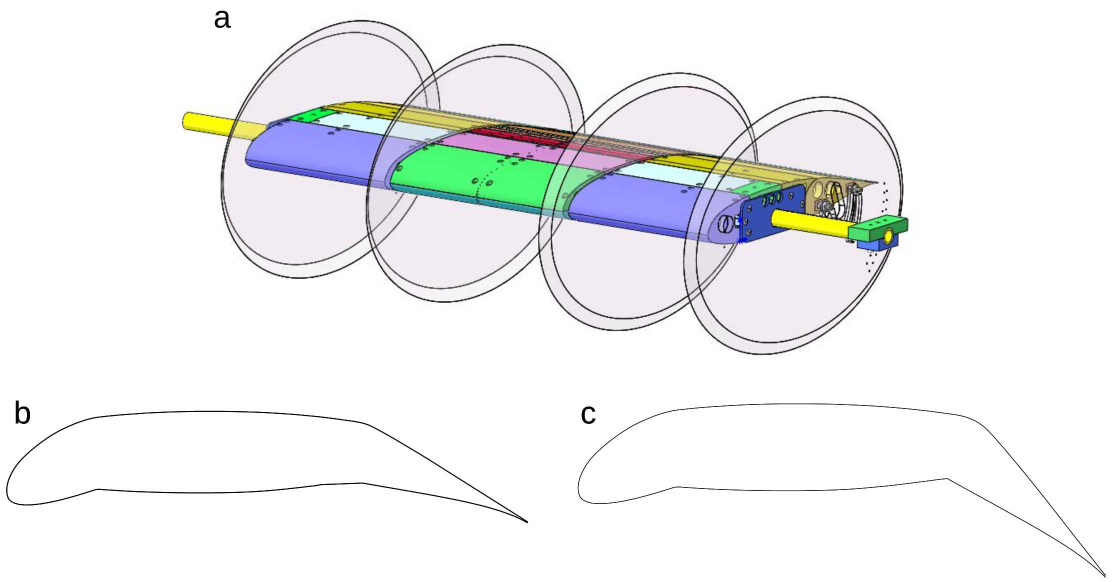

***Figure 2.2.*** *(a) ADVINT-based airfoil model with adjustable trailing edge flap and drooped leading edge. Centerline cross-sections: (b) $\delta$ = 20º and (c) $\delta$ = 40º.*

A subset of experiments on configurations with large-scale flap separation is conducted using an airfoil model based on the configuration used in the ADVINT program (Smith et al. 2006; Figure 2.2a) with a deployed trailing-edge simple flap having chord 0.35*c* and a drooped leading edge. The flap deflection, $\delta$, is fixed for a given configuration, but is easily interchangeable over a broad range (the resulting airfoil profile is shown in Figures 2.2b and c for $\delta$ = 20° and 40°, respectively). The model has a chord length of 457 mm and spans the entire width of the wind tunnel test section. The model consists of an internal structural assembly with replaceable outer surface segments that define the geometry of the airfoil and flap and enable flow control actuators to be integrated into the model in a wide variety of configurations. The midspan section of the airfoil (308 mm in width), bounded by a pair of fences extending ~0.2-0.3*c* into the free stream in all directions, is designed to have a nominally two-dimensional flow. A hollow

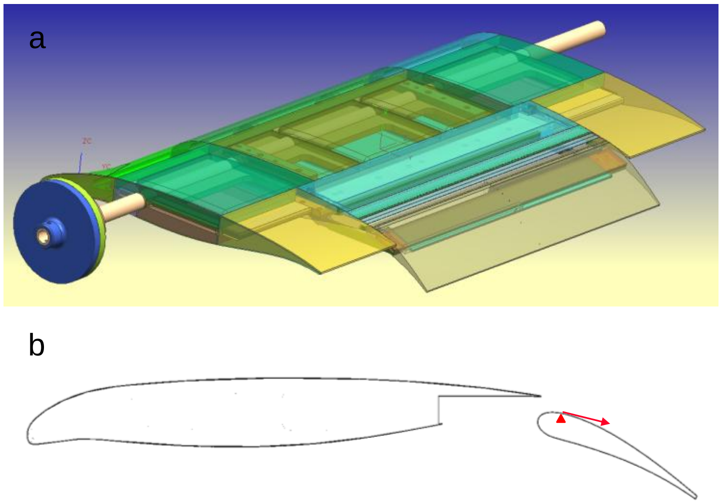

***Figure 2.3.*** *MD 30P-30N airfoil model with trailing edge flap and drooped leading edge. (a) Overview, (b) Centerline cross-section. Triangle and arrow denote flow control actuator location and orientation.*

bar passes through the structural assembly to attach the model to the wind tunnel and permit adjustment of the angle of attack. The interior of the model is hollow and accessible from outside the wind tunnel to provide fluid and electrical access for instrumentation and flow control actuation.

The remaining studies on configurations with large-scale separation over the flap are conducted using an MD 30P-30N airfoil model (Figure 2.3a) with a drooped leading edge and a trailing edge Fowler flap across 60% of the model span with a chord of 0.3*c* that is of similar construction to the simple flap model. The model has an overall chord length of 451 mm and spans the entire width of the wind tunnel test section. Figure 2.3b shows the centerline spanwise-normal cross section of the model, consisting of the main element and deployed Fowler flap. The structural assembly (within the flap and the main body) includes interchangeable components for adjusting the deflection, cross-stream gap and streamwise overlap of the flap in relation to the main element.

## 2.2. *Flow Control Actuators*

Aerodynamic flow control is demonstrated throughout the dissertation using surface-mounted actuators based on two distinct actuation methodologies to introduce momentum into the adjacent flow. In aerodynamic configurations lacking large-scale separation, hybrid actuators each consisting of a synthetic jet integrated into a backward-facing step are used to implement zero-net-mass-flux actuation. To mitigate separation in configurations with larger-scale separation, synthetic jets are integrated into the leading edge of a deployed high-lift flap. Separation control on flaps is also implemented using arrays of self-oscillating fluidic oscillators that produce spanwise-oscillating point jets which are directed into the boundary layer.

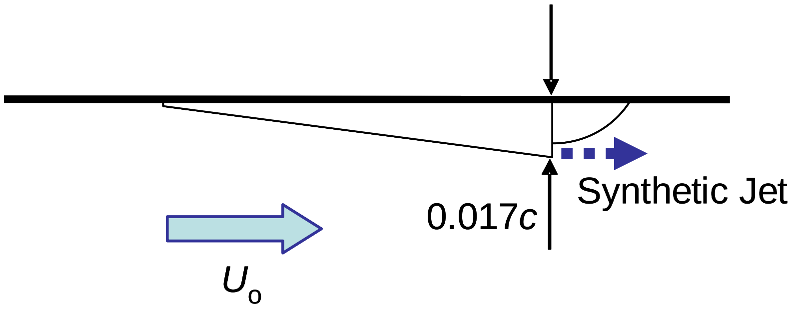

***Figure 2.4***. *Hybrid synthetic jet actuator configuration.*

Aerodynamic flow control in the absence of large-scale separation is investigated using hybrid actuators consisting of a synthetic jet integrated with a passive obstruction that are mounted to the surface of an airfoil at low angles of attack (cf. Chapter 2.1). Unlike earlier implementations of synthetic jet actuation (e.g., Amitay et al. 2001), the hybrid actuators used in the present studies include an obstruction that protrudes above the surface of the airfoil in the direction of the free stream to enable more effective control of trapped vorticity concentrations that are controlled by the jet. One or more actuators are mounted on the surface of the airfoil and have a uniform cross section along the sweep line. As shown in Figure 2.4, in the present experiments each actuator consists of a surface-mounted prismatic obstruction having a triangular cross section with cross stream height of 8.5 mm (0.017*c*) and streamwise length 55 mm (0.11*c*). A round Coanda surface having radius 13 mm and height 6.3 mm is attached along the downstream face of the prismatic obstruction and contains an array of closely spaced static pressure measurement ports. The obstruction is integrated with a synthetic jet actuator that is formed through a rectangular orifice (155 mm wide and $h_{\mathrm{act}} = 0.4$ mm high) in the downstream face, 1 mm below the edge of the top surface. The jet module is driven by an array of 32 mm diameter piezoelectric discs that are mounted 38 mm apart within a central cavity. The effects of the spanwise extent of the active actuator segment have been investigated using a 795 mm segment (0.87*s*) that is placed symmetrically about center span. As explained in further detail in Chapter 3, because only operation of the centermost actuator segment (155 mm; 0.17*s*) has a significant effect on the centerline pressure distribution, the majority of the study is conducted using actuation exclusively in the center of the model. In one series of experiments, a single actuator module is mounted on the pressure surface with its downstream edge located at $x/c = 0.21$ for proximity to the aerodynamic center of the airfoil so that changes in spanwise pitching moment due to the presence and operation of the actuator are minimized (Chapter 3). To demonstrate how pitching moment changes can be achieved, experiments have been conducted with the addition of a second actuator near the trailing edge at $x/c = 0.94$ (Chapters 4-5). To achieve bi-directional changes in pitching moment, a third configuration has been tested with actuators mounted to both the suction and pressure surfaces near the trailing edge (Chapter 6).

The jet actuator operates at a nominal frequency of $f_{act} = 2$ kHz, corresponding to a reduced frequency of $St_{act} = f_{act} \cdot c/U_\infty = 33$ at a free stream speed of $U_\infty = 30$ m/s. At this speed the maximum momentum coefficient is $C_\mu = (0.5 \rho u_j^2 h_{act}) / (0.5 \rho U_\infty^2 c) = 0.9 \cdot 10^{-4}$, where $u_j$ is the measured RMS jet velocity, and the Stokes number $S = h_{act}(2\pi f_{act} / \nu)^{0.5}$ is 11.1. The jet speed is nearly constant along 90% of the streamwise projection of each disk at the actuator orifice and is approximately 50% lower at the center of the gap between adjacent discs (6 mm wide). These spanwise variations are rapidly diminished by the evolution of streamwise vortices and small-scale 3D motions within the jet (cf. Smith and Glezer 1998).

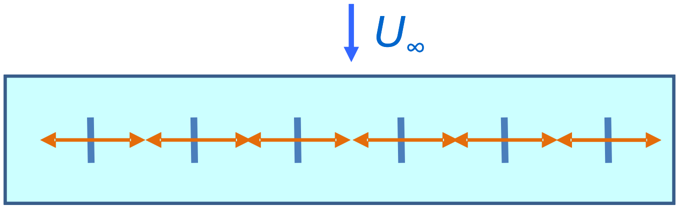

***Figure 2.5.*** *Schematic diagram of spanwise-oscillating fluidic oscillator orifices across a portion of the airfoil span.*

Variation of the size and scale of the large-scale separated flow domain over the suction surface of a deployed flap on a high-lift airfoil is demonstrated for both simple and Fowler flap configurations using active flow control based on an array of self-oscillating fluidic oscillators (e.g., Gregory et al. 2007). The actuation jets oscillate in the spanwise direction (Figure 2.5) and are placed near the leading edge of the suction surface of the flap immediately downstream of the cove between the flap and the main element. This particular location is chosen because the local flow (in the vicinity of the separation point) is susceptible to manipulation that can result in significant changes to the extent of separation. The exact streamwise position is selected based on separation location measurements from PIV measurements of the flow field on the suction surface of the flap in the absence of flow control hardware. The actuator jets are driven by an external air supply (through a mass flow meter) and issue into the boundary layer tangentially to the airfoil surface from orifices recessed into the model to minimize interference with the external flow when the actuators are not operating. The actuators are integrated into an interchangeable segment in the model as a complete spanwise array (across almost the entire flap span), including a common plenum through which air is supplied to all jets and the individual actuator cavities and orifices (with a 1.5 mm square cross section). The jets oscillate at a frequency of ~6 kHz which varies slightly with the mass flow rate. The actuation momentum coefficient $C_\mu$ is estimated from hot wire anemometry measurements in the vicinity of an oscillating jet as installed in the airfoil. The reduced actuation frequency (Strouhal number) based on the airfoil chord and free stream speed ($St_{\mathrm{act}} = f_{\mathrm{act}}c/U_\infty$) is on the order of ten or greater. On the airfoil with a simple flap (Chapter 7) the actuator orifices are located in the midspan section of the airfoil between the pair of fences (cf. §2.1). The actuator module contains 42 oscillating jets across the span having a total orifice area of 95 mm$^2$, yielding a momentum coefficient $C_\mu$ of up to 1.6% at $Re_{\mathrm{c}} = 6.7 \cdot 10^5$. On the airfoil with a Fowler flap (Chapter 9) there are no fences at the spanwise boundaries of the flap, and the actuator module contains 70 oscillating jets across the span having a total orifice area of 158 mm$^2$, yielding an actuator momentum coefficient $C_\mu$ of up to 1.9% at $Re_{\mathrm{c}} = 6.7 \cdot 10^5$. It should also be noted that because the changes in lift and drag due to fluidic actuation are sufficient to influence the upstream flow conditions, the tunnel operating parameters are adjusted in order to maintain the same free stream speed $U_\infty$.

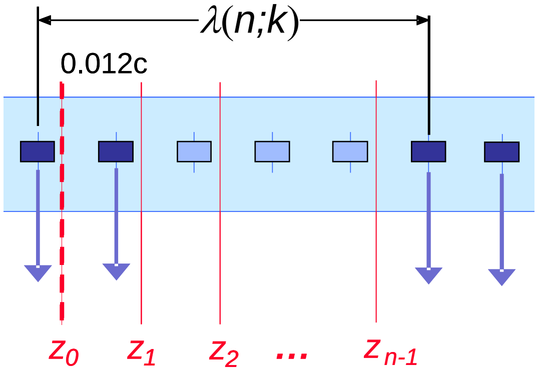

***Figure* 2.6.** *Schematic diagram of synthetic jet array on the airfoil model across a single spanwise period λ(n; k) spanning n jets, of which k adjacent jets are active. A total of 40 jets span the active section of the model. The relative positions of the spanwise period and the centerline pressure measurement array are denoted* $z_0$, …, $z_{n-1}$.

Manipulation of the large-scale separated flow domain over a deployed simple flap is also demonstrated using a modular spanwise array of synthetic jet actuators (Chapter 8). The array of jets is oriented in a direction that is nominally-tangential to the flap and is placed upstream of separation near the juncture between the flap and the main body. The individual jet orifices measure 1.0 x 1.6 mm, and their spanwise spacing can be varied by reconfiguring the modular array. The jet array is placed at $x/c = 0.63$ based on PIV measurements of the flow over the baseline airfoil in the absence of flow control hardware. The actuator module is placed in the midspan section of the airfoil between the pair of fences (cf. §2.1). The actuator array consists of 40 jet actuators across the span having a total orifice area of 65 mm$^2$, yielding an actuator momentum coefficient $C_\mu$ up to 2% at $Re_c = 3.3\cdot10^5$ (computed from hot wire measurements in the vicinity of individual actuator jets). Each jet actuator is driven by a pair of piezoelectric membrane modules on opposite sides of a central cavity that are operated at or near resonance at a frequency of 2.1 kHz, with a corresponding reduced frequency (Strouhal number $St_c = f\cdot c/U_\infty$) of $32 < St_c < 96$. The actuators layout within the module with respect to the free stream is illustrated schematically in Figure 2.6. Jets are selectively activated in spanwise-periodic configurations where the variable parameters are the actuation period $\lambda$ (spanning $n$ jet locations) and the number of adjacent active jets within the period $k$; this is denoted as $\lambda(n; k)$. The spanwise position of the circumferential streamwise array of static pressure ports is fixed relative to the actuator module at an offset of $0.003c$ from the center of the nearest jet orifice. In order to obtain a better estimate of the pressure distribution within a given actuation wavelength, the spanwise position of the pressure measurement plane is varied relative to the jets by successive shifting of the active jets within each period by a single jet "step" and the pressure measurements are repeated. These measurements yield "period-averaged" pressure distributions.

### ***2.3. Instrumentation***

Static pressure distributions around the airfoil model are measured using a circumferential array of pressure ports connected to a Pressure Systems 98RK pressure measurement system with an accuracy of ±4 Pa. There are up to 90 pressure ports located at mid-span on the main bodies of the models and additional ports located on flow control actuator modules for testing with actuation installed. The pressure port locations on the surface of each airfoil model tested are listed in Appendix A. Typical pressure measurements are averaged over a period of ~5 seconds. The aerodynamic forces and moments are estimated from pressure distributions by fitting a spline to the pressure measurements along the airfoil chord and computing numeric integrals (using Simpson's rule) as follows:

$$C_l = \int_0^1 \left(C_{p,l} - C_{p,u}\right) d\left(\frac{x}{c}\right)$$

$$C_{dp} = \int_0^1 \left(C_{p,l}\frac{dy}{dx}_l - C_{p,u}\frac{dy}{dx}_u\right) d\left(\frac{x}{c}\right)$$

$$C_{m,c/4} = \int_0^1 \left(C_{p,l} - C_{p,u}\right)\left(\frac{x}{c} - 0.25\right) d\left(\frac{x}{c}\right)$$

Based on the accuracy of the pressure measurement system, the airfoil geometry, and the pressure port locations, the errors in $C_\mathrm{l}$ and $C_\mathrm{dp}$ are estimated to be ±0.005 and ±0.001, respectively, computed from the total variance in $C_\mathrm{l}$ and $C_\mathrm{dp}$ that results from pressure measurement errors at each port. The aerodynamic forces and moments on the models with large-scale separation are measured directly using two six-axis load cells installed between the ends of the attachment bar and the walls of the wind tunnel. Measurements of lift and drag are accurate to within ±2 N, and pitching moment measurements have an accuracy of ±30 N·cm. Hot wire anemometry measurements of the frequency spectrum of streamwise velocity (Chapter 5) were conducted using a system consisting of a DISA anemometer and a 5 μm diameter probe tip, capable of measuring velocity fluctuations at frequencies up to 50 kHz.

### *2.4. Velocity Measurements using Particle Image Velocimetry (PIV)*

The structure of the airfoil wake and boundary layer are assessed using PIV measurements of the cross-stream velocity distribution near the surface and in the near wake. A PIV system based on hardware and software from LaVision Inc. is utilized, including a LaVision Imager Pro-X 2M camera and LaVision DaVis image acquisition and processing software, along with a double-pulse Nd-YAG laser and fog particle generator. The fog particles are generated using a ROSCO 1700 fog machine and introduced to the flow in the plenum of the wind tunnel. The fog orifice is located in the trailing edge of a vane having an airfoil-shaped cross section in order to minimize disturbance to the flow. The vane is oriented vertically spanning the full height of the wind tunnel and is placed near the centerline of the wind tunnel in these studies. A blower is used to inject the fog particles into the plenum at an adjustable flow rate. The particles are illuminated using a New Wave Research, Inc. Solo 120 Nd-YAG double-pulse laser, capable at operating at a repetition rate up to 15 Hz. The laser beam is expanded using an adjustable system of mirrors, spherical lenses and cylindrical lenses into a laser sheet with a nominal thickness of 1 mm which illuminates the particles within a cross section of the flow. The laser sheet is typically oriented to illuminate the flow in a plane normal to the spanwise axis of the airfoil model. Image pairs are captured using the LaVision Imager Pro-X 2M camera with a 1600 x 1200 pixel CCD sensing element and interchangeable Nikon SLR photographic lenses for varying the size of the field of view (with focal lengths varying from 50 mm to 200 mm). Temporal spacing between images within a pair is selected such that the maximum velocity within the field of view corresponds to a nominal particle displacement of eight pixels.

The majority of the image pair sets used for PIV measurements in this dissertation consist of 500 image pairs each, and the sets used for high-accuracy velocity measurements in the airfoil wake (cf. Chapter 3) each consist of 10000 image pairs. Before velocity vectors are computed from an image pair set, an average intensity image is computed across all images in the set and subsequently subtracted from every image in the set. Doing so removes reflections and background artifacts from the image and enhances the accuracy of the velocity calculations. Within each average-subtracted image pair, estimates of velocity are computed by cross-correlation between interrogation domains spanning 64 x 64 pixels and spaced every 32 pixels horizontally and vertically ("50% overlap"). Based on these results, subsequent velocity measurements are computed using cross-correlation between smaller (32 x 32 pixel) 50%-overlapping interrogation domains which are shifted spatially between the two images in the pair (in order to capture the same particles in both images). This adaptive cross-correlation technique is described in further detail by Scarano and Riethmuller (2000). The vectors within each set are subsequently averaged to obtain a mean flow field. Vectors that deviate excessively from the mean are excluded from the set and the mean flow field is re-computed. For typical sets having 500 image pairs, the resulting mean velocity has error on the order of 1%. For the sets having 10000 image pairs, the mean velocity error is reduced to 0.2%. Vorticity is computed from the mean velocity measurements by numerical differentiation using fourth-order finite differences (in both $x$ and $y$). It must be noted that the resulting vorticity fields (for both time- and phase-averaged measurements) denote the average vorticity at any given location and do not correspond to the instantaneous vorticity at any particular moment. These velocity and vorticity measurements are used to compute higher-order quantities such as vorticity flux, circulation and momentum flux in the flow, as well as to characterize flow separation behavior and to measure boundary layer characteristics (e.g. displacement thickness, momentum thickness, wall friction coefficient etc.).

For the aerodynamic flows without large-scale separation (i.e. airfoil in cruise configuration), PIV velocity measurements along the airfoil centerline on the pressure and suction surfaces are used to assess the boundary layer streamwise development, shape factor and wall friction coefficient, which is subsequently integrated to estimate the wall friction drag. Measurements in the near wake ($1.00 < x/c < 1.18$) are used to measure the streamwise momentum flux in order to obtain a direct estimate of the total change in airfoil drag (time-averaged) and the temporal variation of circulation and vorticity flux (phase-averaged). The flow fields in the vicinity of an actuator (both time- and phase-averaged) are also measured to characterize the interaction of the actuator with the surrounding flow. It is worth noting that the actuation frequency (~2 kHz) is significantly higher than the repetition rate of the PIV system (up to 15 Hz).

For the aerodynamic flows with large-scale separation (i.e. high-lift airfoil), the separated flow domain above the suction surface of the flap is characterized using PIV along the airfoil centerline, along with the upstream boundary layer and the near wake. In the configuration using synthetic jets, the flow field near the juncture between the flap and the main body is also assessed using PIV. Time-averaged measurements in two opposing sets of 40 diagonal planes, each of which is rotated $\pm 30^{\circ}$ about the cross-stream axis, with 500 image pairs per plane are used to compute the 3-D velocity field within an overlap volume.

# CHAPTER 3

# DRAG REDUCTION USING REGULATION OF TRAPPED VORTICITY

Concentrations of trapped vorticity on the surface of an airfoil are created and manipulated using active flow control actuation in a manner that alters the local pressure distribution. The changes in local pressure result in significant aerodynamic effects including reduced pressure drag and changes in lift and pitching moment. It is shown in this chapter how creation and manipulation of a trapped vorticity concentration near the leading edge of the airfoil pressure surface can alter the boundary layer characteristics such that pressure drag is reduced. Placing a trapped vorticity concentration near the trailing edge alters the Kutta condition, affecting the flow around both the suction and pressure surfaces of the airfoil in a manner leading to changes in the pitching moment (Chapter 4). In addition, it is shown how the required actuation authority can be reduced significantly using pulse-modulated actuation at a frequency coupled to the instability of the near wake (Chapter 5) and how alternating pulse-modulated operation of trailing-edge actuators on both the suction and pressure surfaces leads to bi-directional changes in pitching moment without the use of moving control surfaces (Chapter 6).

## *3.1. Aerodynamic Effects of Trapped Vorticity near the Leading Edge*

These aerodynamic effects have been investigated using an airfoil based on a commercial aircraft configuration described in Bower et al. (2004) (Figure 3.1) with a hybrid actuator installed on the pressure surface near the leading edge. The time-averaged pressure distribution around the airfoil at center span in the absence and presence of actuation are

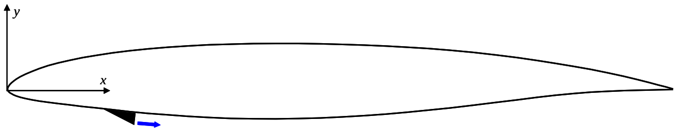

***Figure 3.1**. Airfoil with leading edge actuator.*

shown in Figure 3.2 for $\alpha = 4^{\circ}$ and $Re_c = 6.7 \cdot 10^5$. Due to the sweep of the airfoil, the flow does not stagnate at the leading edge and therefore the maximum pressure coefficient near the leading edge is nominally 0.8. The presence of the inactive actuator results in substantial suction downstream of the actuator and therefore a decrement in $C_p$ on the order of 0.35 within the domain $0.12 < x/c < 0.33$. The maximum magnitude of the pressure decrement increases somewhat with $Re_c$ from ~0.35 to ~0.55. As discussed subsequently, this low pressure region develops due to the formation of a closed trapped vorticity concentration downstream of the inactive actuator. While this reduction in pressure contributes to a decrease in lift, it is offset by a concomitant, smaller increase in $C_p$ over a larger segment of the pressure surface of the airfoil upstream and downstream of the actuator so that the net impact on the lift and pressure drag is minimal.

Synthetic jet actuation (momentum coefficient $C_\mu = 2.05 \cdot 10^{-3}$ per unit span) leads to substantial changes in the interaction domain with the cross flow over the pressure surface and evidently to a reduction in the cross stream scale and strength of the trapped vorticity concentration. The streamwise extent of the local domain of low pressure is reduced (the downstream edge of this domain moves to $x/c \approx 0.26$), and the magnitude of the maximum pressure decrement is significantly increased. While the streamwise length of this domain appears to be independent of $Re_c$, the suction peak decreases with increasing $Re_c$ ($C_p = -1.4$, $-1.3$, and $-1.1$ at $Re_c = 6.7 \cdot 10^5$, $1.0 \cdot 10^6$, and $1.3 \cdot 10^6$, respectively). However, in these measurements the actuation amplitude is invariant

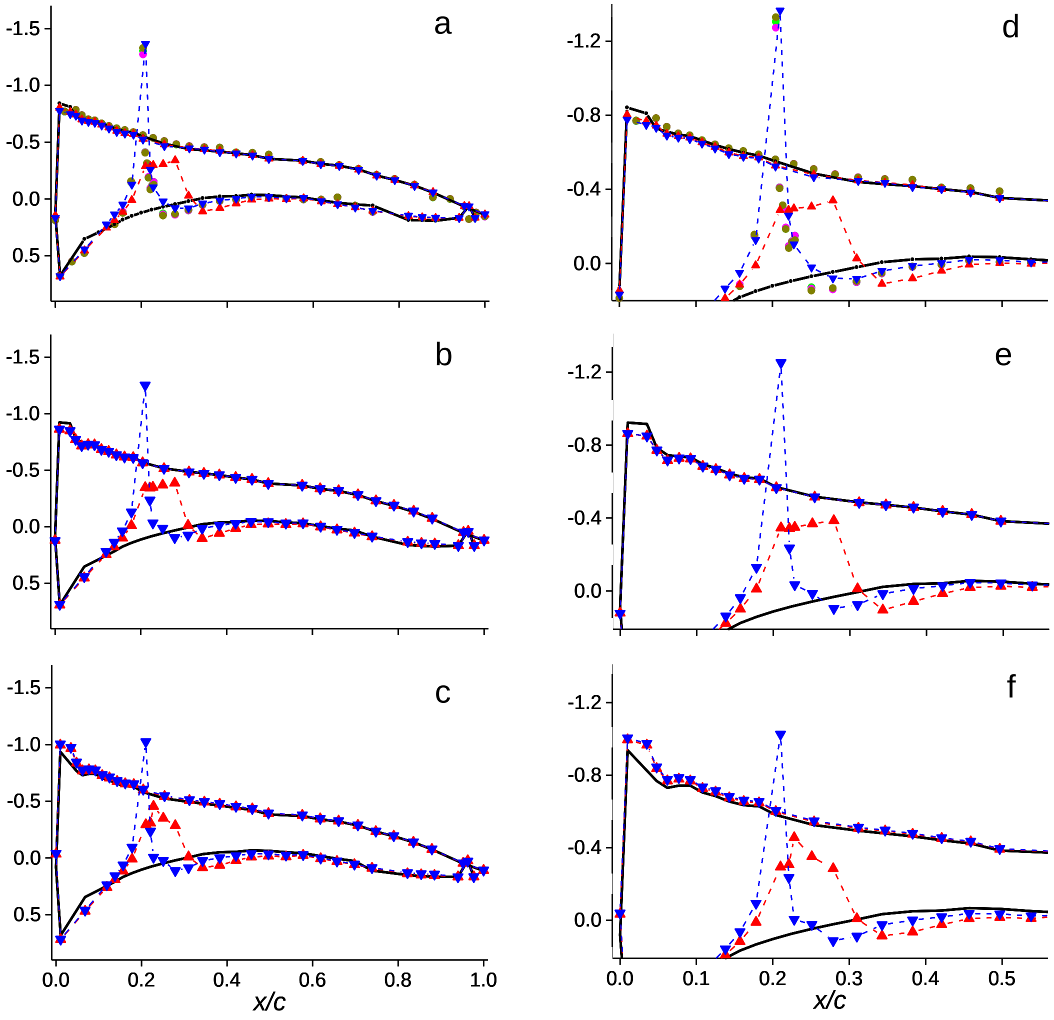

***Figure 3.2**. Pressure distribution around the airfoil for $\alpha = 4^o$ for $Re_c = 6.7 \cdot 10^5$ (a,d), $1.0 \cdot 10^6$ (b,e), and $1.3 \cdot 10^6$ (c,f). Baseline (−), actuator inactive (▲), and active (▼). Figures 3a and 3d include pressure distributions when the actuation is applied symmetrically about the centerline over 0.87s (●), 0.56s (●), and 0.16s (●).*

because the actuators are operated at their maximum power level and therefore the effective momentum coefficient of the jet decreases with increasing $Re_c$; for the data in Figures 3.2a-c, $C_\mu = 2.05 \cdot 10^{-3}$, $0.91 \cdot 10^{-3}$ and $0.51 \cdot 10^{-3}$, respectively. The alteration of the trapped vorticity concentration (cf. Figure 3.3) results in an asymmetric pressure distribution upstream and downstream of the hybrid actuator and contributes to a significant reduction in pressure drag (cf. Figure 3.4). It is noteworthy that these effects occur as a result of the interaction between the jet and the cross flow, and that pressure changes induced by the operation of the jet at the same momentum flux under quiescent conditions are nearly immeasurable.

Figures 3.2a and 3.2d include pressure measurements obtained using addressable actuator segments in order to determine the effect of the spanwise extent of the active segment of the actuator on the measured pressure distribution. Actuation is applied symmetrically about the centerline across 0.87*s*, 0.56*s*, and 0.16*s* and a momentum coefficient per unit span of $C_\mu = 2.05 \cdot 10^{-3}$ showing no significant variation in the center-span pressure distribution when the actuation extends beyond ±0.08*s* about the centerline. For this reason, subsequent measurements are made using actuation within 0.16*s* of the airfoil span.

The effect of actuation on the vorticity layer next to the pressure surface (Figure 3.3) is shown using vector plots of the time-averaged flow field immediately downstream of the actuator for $C_\mu = 0$, $0.22 \cdot 10^{-3}$, $0.91 \cdot 10^{-3}$ and $2.05 \cdot 10^{-3}$, respectively. The flow fields are taken from PIV measurements on the pressure surface in the streamwise domain $0.20 < x/c < 0.28$ at a resolution of 25 μm/pixel and averaged over 10000 realizations due to the diminished flow seeding downstream of the actuator. In the absence of actuation (Figure 3.3a) the upstream boundary layer separates at the actuator orifice, producing a detached vorticity layer and a large separation bubble over the Coanda surface and farther downstream. The presence of this recirculating domain is accompanied by local reduction in the static pressure that is terminated near 0.3*c*. Under actuation ($C_\mu = 0.22 \cdot 10^{-3}$; Figure 3.3b) the synthetic jet interacting with the surrounding flow forms a domain of trapped vorticity which intensifies with increasing $C_\mu$ (e.g. Figure 3.3c; $C_\mu = 0.91 \cdot 10^{-3}$). The vorticity concentration causes a low pressure region to form

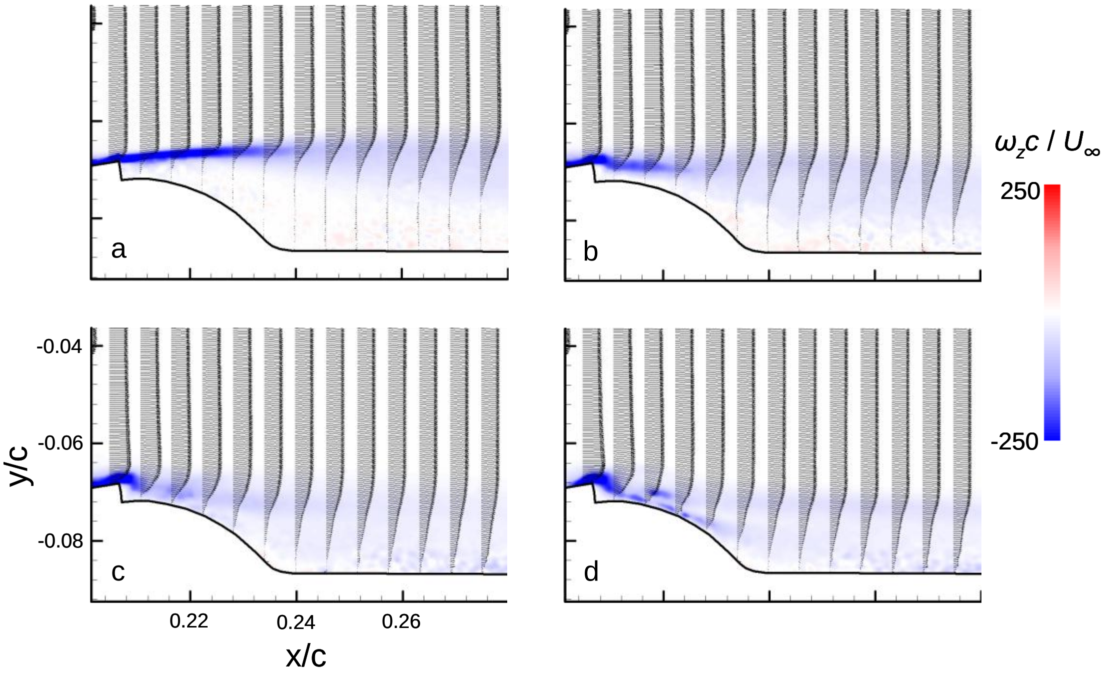

***Figure 3.3**. Flow fields in vicinity of actuator (x/c = 0.21). $C_\mu$ = (a) 0, (b) $0.22\cdot10^{-3}$, (c) $0.91\cdot10^{-3}$ and (d) $2.05\cdot10^{-3}$.*

and the upstream boundary layer accelerates while the flow downstream of the actuator is redirected toward the airfoil surface. As a result, the separation bubble is eliminated and there is substantial pressure recovery over the Coanda surface. With sufficient actuation ($C_\mu = 2.05\cdot10^{-3}$; Figure 3.3d) the separation bubble is almost entirely suppressed and a boundary layer begins to form downstream of the actuator. By altering the strength of the trapped vorticity near the actuator, the characteristics of the separated flow over the Coanda surface and the upstream and downstream boundary layers can be fluidically manipulated, producing corresponding variations in the aerodynamic characteristics of the airfoil.

The effects of actuation on the aerodynamic characteristics of the airfoil at angles of attack within the range $-2^{\circ} < \alpha < 8^{\circ}$ are assessed from the pressure measurements. As shown in Figure 3.4a, the reduction in pressure on the pressure surface of the airfoil as a result of the presence of the inactive hybrid actuator (cf. Figure 3.2) leads to a slight

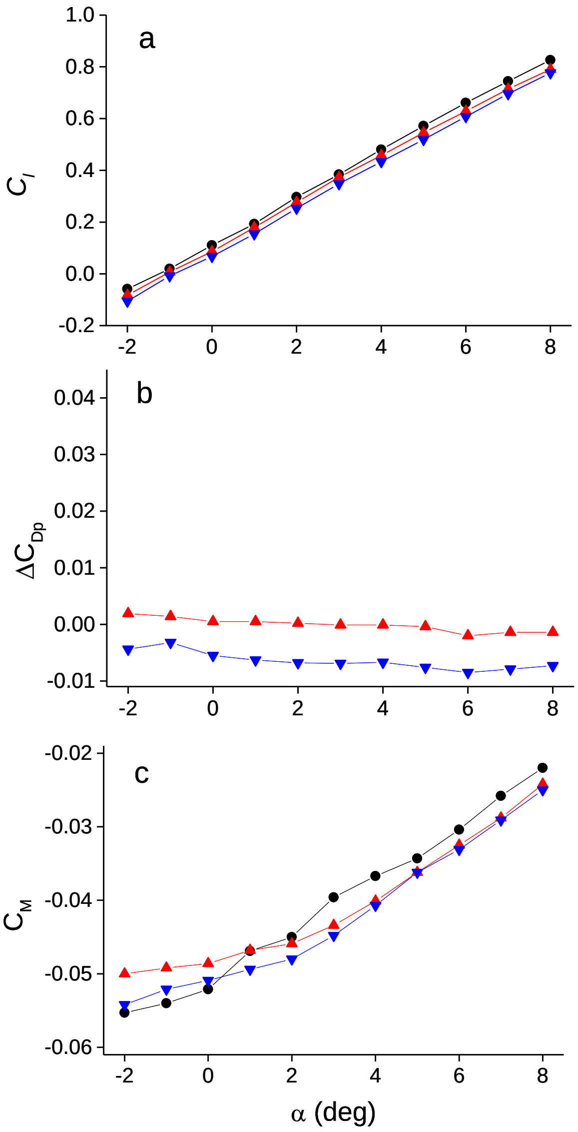

***Figure 3.4**. Variation of (a) $C_l$ , (b) $\Delta C_{dp}$ and (c) $C_m$ with angle of attack for $Re_c = 6.7 \cdot 10^5$: Baseline (●), actuator inactive (▲) and active (▼).*

reduction in lift relative to the baseline airfoil which is invariant with angle of attack within the measured range. This variation is nominally $\Delta C_l \approx -0.02$, corresponding to a reduction of approximately 4% at $\alpha = 4^o$. Jet actuation results in additional decrement of 0.02 in $C_l$, i.e., $\Delta C_l \approx -0.04$ relative to the baseline airfoil or a reduction of approximately 9% at $\alpha = 4^o$. The changes in pressure drag due to actuation are assessed according to the differences in pressure drag relative to the baseline airfoil because the changes in the pressure distribution occur predominantly near the actuator (cf. Figure 3.2a) and due to the limited spatial resolution of the pressure distribution near the leading edge. These measurements are computed from the differences in pressure distributions and are shown in Figure 3.4b. The presence of the inactive hybrid actuator results in virtually no change in pressure drag for $1^{o} < \alpha < 5^{o}$, a slight increase for $\alpha < 1^{o}$ and a comparable slight decrease for $\alpha > 5^{o}$. When actuation is applied ($C_{\mu} = 2 \cdot 10^{-3}$), the pressure drag decreases substantially and uniformly relative to the baseline across the entire range of $\alpha$ (e.g. $\Delta C_{dp} \approx -0.075$ relative to the unactuated airfoil at $\alpha = 4^{o}$). The measurement of the change in pressure drag is used in conjunction with estimates of the change in friction drag from boundary layer measurements to compute the reduction in *total* drag relative to the baseline airfoil.

The effect of actuation on the pitching moment coefficient about $c/4$ has also been computed from the pressure distributions (Figure 3.4c), and no significant effect is indicated. Due to the proximity of the actuator to $c/4$, the resulting changes in pitching moment (with the jet active and inactive) are small. This occurs because the pressure distributions for the baseline, unactuated, and actuated airfoils (cf. Figure 3.2b) differ substantially only in the vicinity of the actuator ($x/c = 0.21$), resulting in no significant change in $C_m$ due to the proximity of the domain of altered pressure to the quarter chord point. For $\alpha > 3°$, the inactive actuator results in $\Delta C_m \approx -0.003$ and actuation results in no further changes. For $\alpha < -1°$, $C_m$ with the inactive actuator is higher ($\Delta C_m \approx 0.005$) than for the baseline airfoil, and actuation reduces the increment to 0.002, bringing $C_m$ closer to the baseline values.

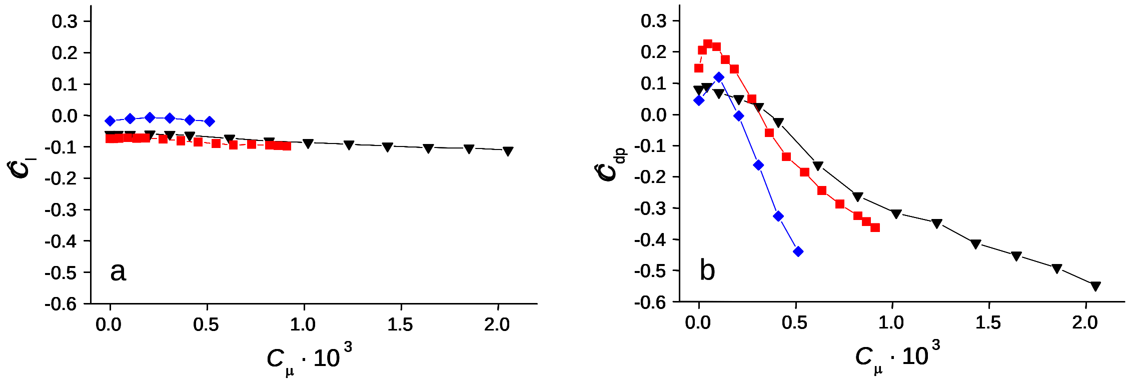

***Figure 3.5**. Variation with $C_\mu$ of (a) $\hat{C}_l$ and (b) $\hat{C}_{dp}$ for $\alpha = 4^o$ and $Re_c = 6.7 \cdot 10^5$ (▼),$1.0 \cdot 10^6$ (■), and $1.3 \cdot 10^6$ (♦).*

By altering the strength of the trapped vorticity near the actuator, the characteristics of the separated flow over the Coanda surface and the upstream and downstream boundary layers can be fluidically manipulated, producing corresponding variations in the aerodynamic characteristics of the airfoil. The sensitivity of aerodynamic performance modification to the actuation amplitude as measured by $C_\mu$ is shown in Figures 3.5a and b ($\alpha = 4^o$ and $Re_c = 6.7 \cdot 10^5$, $1.0 \cdot 10^6$, and $1.3 \cdot 10^6$) in terms of the variation of the fractional lift and drag increments (relative to the baseline airfoil) $\hat{C}_l = \Delta C_l / C_{l0}$ and $\hat{C}_{dp} = \Delta C_{dp} / C_{dp0}$ ($C_\mu$ is limited by the maximum speed of the actuator jet). Figure 3.5a shows that while the presence of the inactive hybrid actuator results in some reduction in lift, the activation of the jet brings about only a minimal additional change. Overall, the decrease in lift induced by the presence of the hybrid actuator is less than 10% for $Re_c = 6.7 \cdot 10^5$ and $1.0 \cdot 10^6$, and less than 2% for $Re_c = 1.3 \cdot 10^6$. The corresponding fractional variations in $C_{dp}$ (Figure 3.5b) are far more significant. The maximum available $C_\mu$ at each of the three Reynolds numbers (in increasing order) results in maximum reductions in pressure drag of 55%, 40%, and 45%, respectively, relative to the baseline configuration. It is interesting that at $C_\mu \sim 0.1 \cdot 10^{-3}$ the jet actuation results in an *increase* in pressure drag relative to the baseline and inactive actuator configurations ostensibly owing to an increase in the size of the trapped vortex (cf. Figure 3.2b) at low actuation levels. As $C_\mu$ increases the strength of the trapped vortex increases but its characteristic cross stream scale decreases, also illustrated in Figure 3.2b. Of particular note is the performance at $Re_c = 1.3 \cdot 10^6$ for which the reduction in pressure drag is 45% despite the fact that the maximum jet momentum coefficient is $C_\mu = 0.5 \cdot 10^{-3}$. The variation of actuator performance with $Re_c$ for a given $C_\mu$ is explained by the fact that the scale of the boundary layer and consequently its interaction with the hybrid actuator vary with $Re_c$. In particular, increasing $Re_c$ reduces the cross-stream height of the boundary layer and therefore its size relative to the time-periodic vortical structures that are produced by the jet for which the operating parameters remain invariant. The present measurements show that as $Re_c$ increases, the effectiveness of the actuation (e.g., as measured by the change in $C_{dp}$) also increases despite the reduced $C_\mu$. This indicates that the coupling between the actuation and the local boundary layer is improved as the boundary layer thickness decreases.

### *3.2. Boundary Layer Characterization and Wall Friction Measurement*

The effects of the actuation on the friction drag (and therefore the changes in *total* drag) are estimated from measurements of velocity profiles around the airfoil ($\alpha = 4^\circ$ and $Re_c = 6.7 \cdot 10^5$) using high-resolution PIV within the boundary layer in cross stream planes normal to the spanwise axis of the airfoil at ten streamwise locations on the pressure surface and eight streamwise locations on the suction surface as shown schematically in Figure 3.6 and listed numerically in Appendix A. Within each square field of view of the

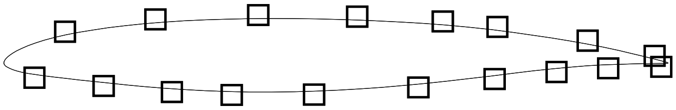

***Figure 3.6***. *Wall friction measurement locations on the airfoil. Each frame approximately correspon to the size of the field of view.*

camera (measuring between 13 mm; 0.026*c* and 20 mm; 0.040*c* on the side to accommodate the changes in the boundary layer thickness) the velocity measurements are averaged in the streamwise direction to obtain a single cross-stream velocity profile. Each data set consists of 400 image pairs. The time-averaged data are used to calculate the displacement thickness, momentum thickness, shape factor, and wall friction coefficient $C_f$. Since the most significant changes in the flow are located near the actuator (cf. Figure 3.2) the measurement domains are concentrated on the pressure surface, and one measurement domain ($x/c = 0.11$) is used to measure the velocity across the actuator itself.

Figures 3.7a and b show samples of cross stream velocity distributions on the pressure surface boundary layer at $x/c = 0.15$ and 0.35, respectively, for $\alpha = 4^o$ and $Re_c = 6.7 \cdot 10^5$. The velocity and cross stream coordinate are scaled by the boundary layer edge velocity ($U_{e\,b}$) and displacement thickness ($\delta^*_b$) of the boundary layer of the baseline airfoil. The velocity between the last valid data point and the wall is estimated using linear interpolation. The local flow speed at the edge of the boundary layer upstream of the actuator (Figure 3.7a) increases significantly in the presence of the actuator, and it is lowest for the baseline airfoil (where the boundary layer is laminar). The presence of the inactive hybrid actuator results in a significant acceleration of the local edge velocity to $1.08\,U_{e\,b}$ that is associated with the local reduction in pressure (cf. Figure 3.2). Jet actuation results in an additional increase in the edge velocity to $1.18\,U_{e\,b}$ that is associated with the suction peak downstream of the jet (cf. Figure 3.2). Therefore the formation of the trapped vorticity domain downstream of the actuator (cf. Figure 3.3) leads to a local acceleration of the external flow and a reduction in the local static pressure that, owing to the slope of the surface, contributes to a significant reduction in pressure drag (with minimal fractional reduction in lift). As is evident from Figure 3.2, when the actuator is inactive, the extent of the recirculating flow domain is such that the low pressure downstream of the actuator nullifies the effect of the reduced pressure upstream.

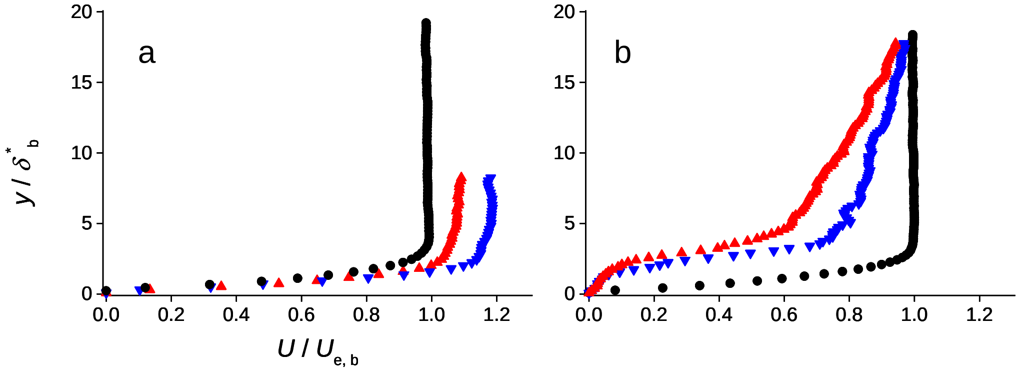

***Figure 3.7**. Cross-stream distributions of the streamwise velocity on the pressure surface at x/c = (a) 0.15 and (b) 0.35. Baseline (●), and with inactive (▲) and active (▼) actuators.*

The velocity distributions in Figure 3.7b are measured 0.13*c* downstream of the actuator. At this location, the boundary layer edge velocity in the presence of the hybrid actuator (inactive and active) is lower than the corresponding velocity over the baseline airfoil, which is commensurate with the increase in the local static pressure downstream of the actuator compared to the baseline (cf. Figure 3.2). The reduction in velocity induced by the inactive actuator is considerably larger than when the actuator is active, indicating an increase in flow momentum near the wall under actuation that corresponds

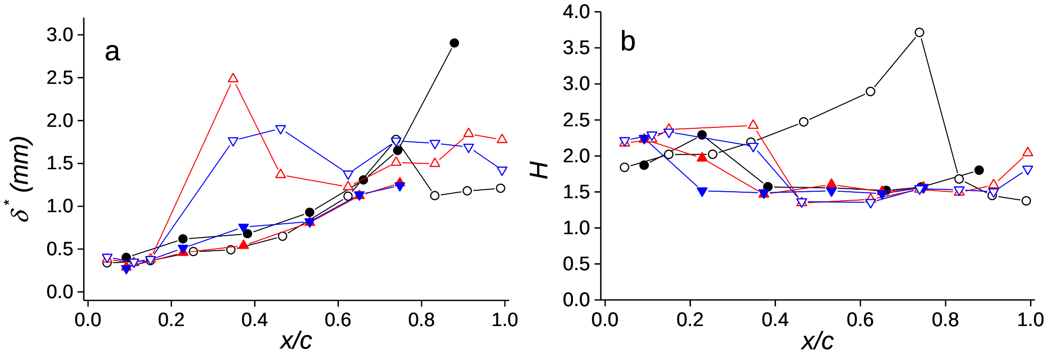

***Figure 3.8****. Variation of (a) $\delta^*$ and (b) boundary layer shape factor with streamwise location for $Re_c = 6.7 \cdot 10^5$ and $\alpha = 4^o$. Baseline (●), inactive (▲), and active (▼) actuator. Open and closed symbols indicate pressure and suction surfaces, respectively.*

to the pressure recovery downstream of the actuator (cf. Figure 3.2) resulting in reduced pressure drag.

The variation of the boundary layer displacement thickness $\delta^*$ along the surface of the airfoil is shown in Figure 3.8a for the baseline airfoil, as well as the airfoil with the inactive and active hybrid actuator. On the suction surface (closed symbols), the displacement thickness increases monotonically for the three configurations, and is typically slightly (0.1 mm) larger than for the baseline airfoil. Because the boundary layer becomes partially separated near the trailing edge on the suction surface, meaningful values of displacement and momentum thickness cannot be calculated for certain streamwise locations and are not indicated in the plot. The presence of the (inactive) hybrid actuator on the pressure surface of the airfoil leads to a significant increase in $\delta^*$ for $x/c > 0.15$ (at $x/c = 0.15$, $\delta^* \approx 0.37$ mm). The increase in $\delta^*$ at the next measurement station (0.13*c* downstream of the jet orifice) is the result of the formation of the recirculation domain that is associated with the trapped vortex. The effects of this domain are present as far downstream as $x/c = 0.6$. In the presence of actuation, the cross-stream extent of the trapped vorticity domain decreases and with it the magnitude of the displacement thickness as higher speed fluid is drawn closer to the wall (cf. Figure 3.3). Farther downstream, $\delta^*$ is relatively uniform (between 1.5-2.0 mm for $x/c > 0.5$). The corresponding displacement thickness of the boundary layer of the baseline airfoil increases monotonically as far downstream as 0.74c before decreasing to approximately 1.2 mm following transition to turbulence (as momentum from the free stream is redirected toward the wall), which can be determined more clearly by the change in the boundary layer shape factor.

The state of the boundary layer can be assessed from the streamwise variation of the shape factor $H$ (Figure 3.8b). Upstream of $x/c = 0.15$ on both the suction and pressure surfaces, the shape factor varies as $1.8 < H < 2.4$, which is typical of a laminar boundary layer (although $H$ is also affected by surface curvature and pressure gradient). There is significant variation in the shape factor on the suction surface near $x/c = 0.2$ where the boundary layer appears to undergo transition to turbulence in the presence of the hybrid actuator. For $x/c > 0.35$, $H$ has a nominal value of 1.5 on the suction surface for all three configurations and for both states (i.e., inactive and active) of the hybrid actuator, indicating that the boundary layer downstream of the actuator is turbulent. The shape factor of the pressure surface boundary layer of the baseline airfoil monotonically increases to a level in excess of 3.5 before decreasing to approximately 1.5 near $x/c = 0.8$, indicating transition to turbulence. Therefore, it is expected that the friction drag of the baseline airfoil is smaller than in the presence of the hybrid actuator.

The wall friction coefficient $C_f$ is computed from the measured velocity distributions. At locations where the boundary layer is turbulent, $C_f$ is determined based on Clauser's method (1954) as shown in Figure 3.9a (using cross stream distribution of the streamwise velocity at $x/c = 0.38$ on the suction surface). The measured velocity profiles are scaled to fit the universal law of the wall for a turbulent boundary layer using the wall velocity scale $u_* = [\nu\,(\partial u / \partial y)_w]^{1/2}$ and the scaled length $y_+ = yu_*/\nu$. The wall friction coefficient is obtained from $C_f = 2(u_*/U_\infty)^2$. An alternate wall friction coefficient $C_{f*}$ is also computed using the boundary layer edge velocity $U_e$. At locations where the boundary layer is laminar, the wall friction coefficient is obtained by fitting the velocity distributions to a Falkner-Skan profile.

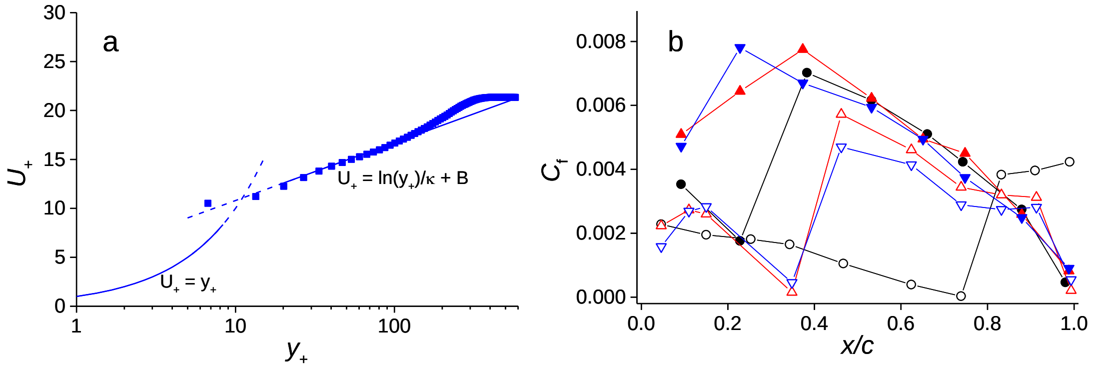

***Figure 3.9**. (a) Cross-stream velocity distribution for a turbulent boundary layer scaled to fit the universal law of the wall. (b) Variation of wall friction coefficient with streamwise location. Baseline (●), inactive (▲), and active (▼) actuator. Open and closed symbols indicate pressure and suction surfaces, respectively.*

The streamwise distribution of the wall friction coefficient $C_f$ (normalized by the global free stream velocity) is shown in Figure 3.9b. On the suction surface (closed symbols) at $x/c = 0.09$ the boundary layer is laminar with $C_f = 0.004$. At the next downstream station ($x/c = 0.23$), $C_f$ on the baseline airfoil decreases because the laminar boundary layer continues to develop. At $x/c = 0.38$ wall friction increases to $C_f = 0.007$ upon transition to turbulence. As indicated in connection with the evolution of $H$ (Figure 3.8b) transition on the suction surface in the presence of the hybrid actuator occurs farther upstream, resulting in larger values of $C_f$ at $x/c = 0.23$. For $x/c > 0.35$, $C_f$ monotonically decreases as a turbulent boundary layer develops, for all three configurations. On the pressure surface (open symbols), the boundary layer is laminar near the leading edge for all three configurations, with $C_f \approx 0.002$ and remains laminar on the baseline airfoil as far downstream as $0.74c$ with $C_f$ decreasing monotonically in the streamwise direction. Farther downstream, following transition, $C_f$ increases to approximately 0.004. In the presence of the hybrid actuator, $C_f$ decreases significantly downstream of the actuator near the downstream edge of the recirculating flow domain ($x/c = 0.35c$). When the jet is activated the streamwise extent of the recirculating domain decreases and therefore the wall friction coefficient downstream of $x/c > 0.4$ is somewhat lower than with the inactive actuator. It is also noteworthy that because of the upstream shift of the suction surface transition point (cf. Figure 3.8b) caused by actuation higher $C_f$ values are found farther upstream than in the absence of actuation.

To validate the measurements of $C_f$ it is instructive to analyze the relationship between $C_f^*$ (calculated using the local boundary layer edge velocity) and $Re_{\theta*}$, the Reynolds number based on the momentum thickness of the boundary layer, as shown in Figure 3.10. Also shown are the wall friction coefficients for Blasius and Falkner-Skan ($\beta = 0.6$) boundary layers along with a correlation for the wall friction of a flat plate turbulent boundary layer $C_f^* = 0.306 \ln(4.075 Re_{\theta*})^{-2}$ (Abbott and von Doenhoff 1959). The values of $C_f^*$ for the turbulent boundary layers on the surface of the airfoil agree well with the correlation, except in the locations where the flow is not fully attached (i.e., downstream of the actuator and near the trailing edge). The measurements of $C_f^*$ for laminar boundary layers on the airfoil follow the same trend as for the Blasius boundary

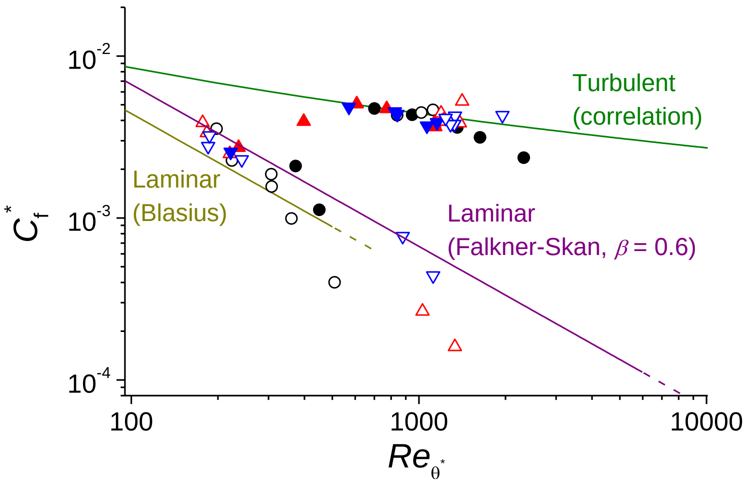

***Figure 3.10**. Variation of $C_f^*$ with Reynolds number based on the boundary layer momentum thickness. Baseline (●), inactive (▲), and active (▼) actuator. Open and closed symbols indicate pressure and suction surfaces, respectively.*

layer, i.e., $C_f^* \propto (Re_{\theta^*})^{-1}$, but with larger values due to the presence of favorable pressure gradients (cf. Figure 3.2). As a result, the values of $C_f^*$ for the laminar boundary layers are in better agreement with the values for a Falkner-Skan boundary layer (with a positive $\beta$, e.g. $\beta = 0.6$), as shown in Figure 3.10. It should be noted that because of its greater stability, $C_f^*$ for the Falkner-Skan ($\beta = 0.6$) boundary layer is plotted for higher $Re_{\theta^*}$ than for the Blasius boundary layer.

The wall friction drag $C_{df}$ is estimated from integration of the wall friction coefficient around the airfoil ($Re_c = 6.7 \cdot 10^5$). For the baseline configuration, in which the boundary layer is laminar along much of the pressure surface, an estimate of $C_{df} = 0.0058$ is obtained. Since the flow along significant portions of the baseline airfoil is laminar, the estimated $C_{df}$ is likely to increase at higher $Re_c$ as the boundary layer transitions to turbulence farther upstream. In the presence of the hybrid actuator, the boundary layer downstream of the actuator is turbulent, and correspondingly the estimates for $C_{df}$ are higher (0.0081 and 0.0076 with the actuator inactive and active, respectively). Combining the estimates of friction drag and pressure drag yields an estimate for the total airfoil drag coefficient for the three configurations tested. For the baseline airfoil an estimate of $C_{\mathrm{d}} = 0.0170$ is obtained. In the presence of the inactive hybrid actuator, $C_{\mathrm{d}} = 0.0192$ (13% larger than baseline; $\Delta C_{\mathrm{d}} = 0.0022$). However, in the presence of jet actuation, the *total* drag coefficient is estimated as $\mathrm{C_d} = 0.0121$ which is 29% lower than the baseline, or $\Delta \mathrm{C_d} = -0.0049$. It is noted that on the present airfoil, the boundary layer upstream of the actuator remains laminar over the entire range of Reynolds numbers tested (up to $1.3 \cdot 10^6$). The effectiveness of the actuation in the presence of a turbulent boundary layer upstream of the actuator is demonstrated using a trailing edge actuator as described subsequently in chapter 4. As shown in Figure 3.4, the actuation results in a decrease in lift of 9% relative to the baseline and so the reduction in total drag leads to a 27% *increase* in *l*/*d* from 28.3 to 35.8.

### *3.3. Drag Reduction Measurement by Near-Wake Characterization*

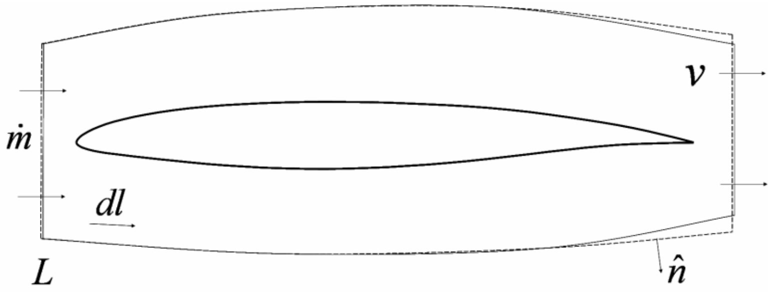

***Figure 3.11***. *Control volumes around airfoil for analysis of mass flux and momentum flux per unit span. Equal mass flux: unactuated (solid), actuated (dashed). Upper and lower boundaries coincide with streamlines.*

The estimates of the total reduction in $C_{\mathrm{d}}$ from pressure drag and wall friction are validated using a *direct* measurement of the total drag reduction from control volume analysis (cf. Figure 3.11) in both the absence and presence of actuation. The mass and streamwise momentum fluxes ($\dot{m} = \oint_L \rho(\vec{v} \cdot \hat{n})dl$ and $\dot{p}_x = \oint_L \rho u(\vec{v} \cdot \hat{n})dl$, respectively) through the control volumes are calculated from high-resolution PIV measurements of cross-stream velocity distributions in the near wake ($1.00 < x/c < 1.17$). The upper and lower bounds of the control volumes are selected to coincide with streamlines well outside of the wake that extend sufficiently far upstream where the flow is uniform. Because the actuation alters the flow field around the airfoil, the streamlines that define the upper and lower boundaries of the control volume are slightly different in the absence and presence of actuation as are the cross-stream extents of the downstream (outlet) boundaries of the control volumes. The upstream (inlet) boundaries of the control volumes are selected to have identical cross-stream heights and therefore equal influxes of mass and streamwise momentum.

The airfoil drag $C_\mathrm{d}$ can be determined, in principle, by computing the time rate of change of streamwise momentum across a single control volume. The terms contributing to the time rate of change in streamwise momentum include the streamwise momentum fluxes $\dot{p}_{x,in}$ and $\dot{p}_{x,out}$ at the upstream and downstream boundaries, respectively (since there is no momentum flux across the upper and lower boundaries, which coincide with streamlines) and the net streamwise component of the normal and shear forces on the control volume due to the pressure and shear stress distribution on the boundary. However, what is of interest is the *difference* in $C_\mathrm{d}$ that is brought about by the actuation $\Delta C_d = C_\mathrm{d,u} - C_\mathrm{d,a}$, which can be computed from the difference in the individual contributing terms. Since the uniform flow at the upstream boundaries of the control volumes is the same in the absence and presence of actuation, the differences in momentum flux and pressure vanish on the upstream boundary. Based on measurements of the velocity gradients across the upper and lower boundaries, the contributions of shear stress to drag are estimated to be on the order of $\Delta C_d \sim O(10^{-6})$, and hence are negligible. Because the lift is nearly identical both in the absence and presence of actuation (cf. Figure 3.4a), the circulation changes little and hence the streamlines and pressure distributions away from the airfoil surface are similar. For this reason, and because the streamlines are relatively flat, the contributions of pressure to $\Delta C_d$ on the upper and lower boundaries are negligible. The remaining terms are:

$$\Delta d = d_u - d_a = ([\dot{p}_{x,\,out}]_a - [\dot{p}_{x,\,out}]_u) + ([f_p]_a - [f_p]_u)$$

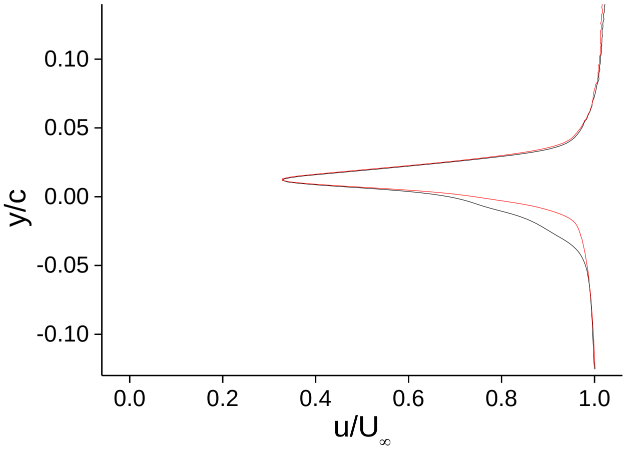

***Figure 3.12.*** *Velocity profiles at x/c = 1.029: (−) Unactuated, (−) Actuated.*

Shown in Figure 3.12 are time-averaged velocity profiles in the near wake of the airfoil from which the change in momentum flux is computed. Measurements are averaged over 10000 PIV realizations to obtain velocity measurements accurate to within 0.2%. Streamwise velocity profiles at $x/c = 1.029$ in the absence and presence of actuation show how actuation causes the wake to become narrower due to an increase in velocity on the pressure surface, where the actuator is located, and also show how the velocity profiles match at the cross-stream edges of the measurement domain. As a result, the entire portion of the wake where a difference in momentum is present is located within both cross-stream velocity profiles. The difference in momentum flux is computed by integrating the momentum fluxes between cross-stream bounds spanning $\Delta(y/c) = 0.2668$ and 0.2639 for the unactuated and actuated profiles, respectively, so that the mass fluxes are equal. The turbulence quantity $\overline{u'u'}$ is incorporated into the momentum flux calculation (but has no effect on mass flux).

The pressure on the downstream boundary of the control volume is estimated by integrating the pressure gradient along the boundary (computed from the Navier-Stokes equations) starting with the pressure at the top of the boundary. The pressure at the top of the boundary is computed using Bernoulli's equation, which applies along the streamline forming the upper boundary of the control volume.

The differences in downstream momentum flux and in downstream pressure between the absence and presence of actuation are computed to be $\Delta C_\mathrm{d} = 0.0073$ and $-0.0005$, respectively, resulting in a reduction in the *total* drag of the airfoil of $\Delta C_\mathrm{d} = 0.0068$ that is comparable to the estimate of $\Delta C_\mathrm{d} = 0.0071$ from the pressure drag and wall friction results.

Because the aerodynamic effects of actuation on the pressure surface near the leading edge are limited primarily to drag reduction, it is desirable to assess the effects of actuation from other locations on the airfoil. As discussed in Chapter 4, configurations with hybrid actuators near the trailing edge enable the flow around the trailing edge to be altered in a manner that leads to changes lift and pitching moment.

# CHAPTER 4

# SUPERPOSITION OF TRAPPED VORTICITY ACTUATION

The effects of creating and manipulating trapped vorticity with active flow control described in Chapter 3 *are primarily confined to the vicinity of the actuator* (cf., Figure 3.3), and the resulting aerodynamic effects primarily consist of drag reduction. For this reason, configurations are tested where additional hybrid actuators are placed around the airfoil in order to create and manipulate vorticity concentrations that result in *additive* aerodynamic effects. In particular, by placing actuators near the trailing edge the flow around the trailing edge can be altered in a manner that changes the pitching moment $C_m$. Two configurations with superposed trapped vorticity have been tested, one containing trapped vortices near the leading edge and trailing edge of the pressure surface (discussed in connection with Figures 4.1-4.3) and another containing trapped vortices on both sides of the trailing edge (Figures 4.4-4.9).

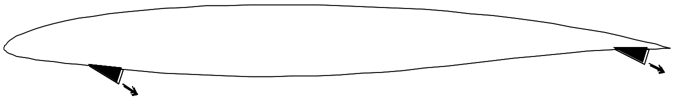

***Figure 4.1**. Airfoil configuration with two surface actuators.*

The configuration with two pressure-surface-mounted hybrid actuators was formed by adding an actuator to the configuration in Figure 3.1 near the trailing edge of the airfoil ($x/c$ = 0.94) as illustrated in Figure 4.1. Because this position is downstream of both the baseline transition point on the pressure surface (cf. Figure 3.8b) and the upstream actuator, the boundary layer upstream of the trailing edge actuator is turbulent (in contrast to the laminar boundary layer upstream of the actuator near the leading edge,

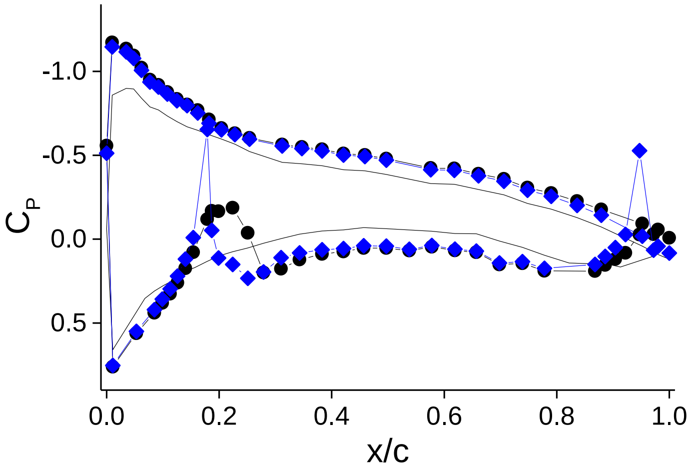

***Figure 4.2**. Pressure distribution ($\alpha$ = 4° and $Re_c = 1.0{\cdot}10^6$): (–) baseline, (●) actuators inactive, (♦) both actuators operating.*

cf. Figure 3.8b). In this manner it is shown how the effects of actuation are similar regardless of whether the upstream boundary layer is laminar or turbulent.

The effects of actuation on the pressure distribution around the airfoil with two actuators are shown in Figure 4.2 for $\alpha$ = 4° ($Re_c = 1.0{\cdot}10^6$). Having two inactive hybrid actuators on the pressure surface may be thought of as having similar effects on circulation, and therefore on lift, to the changes associated with the presence of a small trailing edge flap and a leading edge slat, or may be considered a change in the effective camber. This is illustrated by the fact that the presence of the actuators results in an increase in pressure of $\Delta C_\mathrm{p} \approx 0.15$ on the pressure surface between the actuators and a comparable decrease in pressure across nearly the entire suction surface. The changes in $C_\mathrm{p}$ near the leading edge actuator are largely unaffected by the presence of the trailing edge actuator. The trailing edge actuator induces a reduction in pressure upstream of the jet orifice (as with the leading edge actuator) in addition to a decrease in the pressure at the trailing edge (cf. DeSalvo and Glezer 2004). Continuous operation of either actuator results in significant alteration of the pressure distribution near the active jet, with

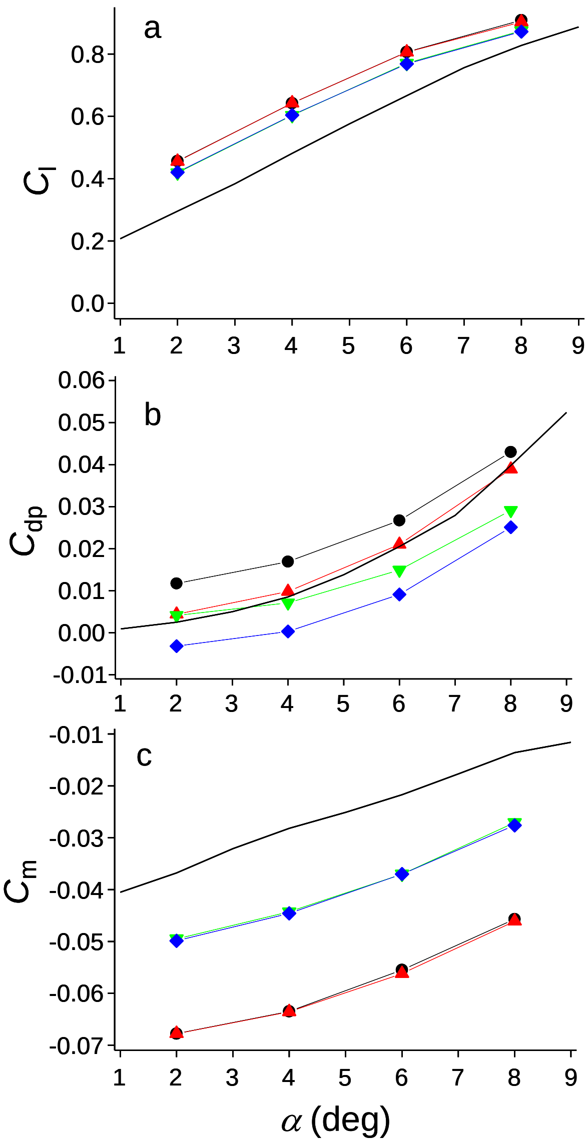

***Figure 4.3***. *Variation of (a)* $C_l$, *(b)* $C_{dp}$ *and (c)* $C_m$ *with angle of attack. (—) Baseline, (●) Both actuators inactive; Active actuators: (▲) Upstream actuator, (▼) Downstream actuator, (♦) Both actuators.*

relatively little effect on the pressure distribution elsewhere on the airfoil. Operation of the leading edge actuator results in similar changes that occur in the absence of the trailing edge actuator (cf. Figure 3.2). The trailing edge actuator induces a suction peak with a local pressure minimum $C_p \approx -0.5$. The pressure downstream of the actuator and at the trailing edge increases by $\Delta C_p \approx 0.15$, leading to a pressure increase on the suction surface near the trailing edge that extends as far upstream as $x/c = 0.6$ when the actuator is operating. These results show that the changes in pressure that occur due to the operation of either actuator are predominantly local, and it has also been shown that the effects of the actuators are relatively independent.

The effects of the actuation on the lift, pressure drag and moment coefficients over a range of angles of attack are shown in Figure 4.3 for the baseline airfoil and in the presence of both inactive actuators and when either actuator or both are operational. The inactive actuators lead to an increase in lift (Figure 4.3a) compared to the smooth airfoil where the lift increment is nearly constant at $\Delta C_l \approx 0.13$ for $\alpha < 6^o$. When the downstream actuator is active, the lift increment decreases to $\Delta C_l \approx 0.09$ (relative to the smooth airfoil) regardless of whether the upstream actuator is operational. Perhaps the most important feature of the data in Figure 4.3a is that when both actuators are operational, there is still a net increase in lift of 15% at $\alpha = 6°$ relative to the baseline. When the actuators are inactive, the pressure drag increases by 30% (at $\alpha = 6°$) relative to the baseline. However, when the upstream actuator (alone) is operating the pressure drag (Figure 4.3b) decreases by $\Delta C_{dp} = 0.005$ and is quite close to the drag of the baseline airfoil. When the downstream actuator alone is active, the drag for $\alpha > 4^o$ is less than the drag of the baseline (smooth) airfoil and the magnitude of the drag reduction increases with $\alpha$. That both the upstream and downstream actuators (having laminar and turbulent upstream boundary layers, respectively) individually reduce the pressure drag, indicates that actuation is effective regardless of the state of the upstream boundary layer. The drag reduction is largest when *both* actuators are operational and it varies from $\underline{\Delta} C_{dp} = 0.005$ at $\alpha = 2^o$ to $\Delta C_{dp} = 0.014$ at $\alpha = 8^o$. Therefore, the increase in lift and the corresponding decrease in drag lead to an increase in $l/d_p$ by a factor of 2.6 at $\alpha = 6°$. For the trailing edge actuator, the pitching moment about $c/4$ (Figure 4.3c) increases monotonically with $\alpha$. When the downstream actuator is inactive, $C_m$ becomes more negative by $\Delta C_m \approx -0.03$ due to the increased pressure and suction on the bottom and top surfaces near the trailing edge. Operation of the downstream actuator reduces the decrement to $\Delta C_m \approx -0.015$ relative to the baseline airfoil.

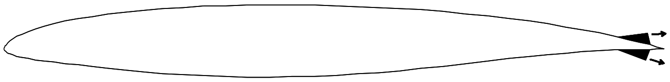

***Figure 4.4**. Airfoil model with two hybrid actuators near the trailing edge.*

Bi-directional changes of the pitching moment of an airfoil without the presence of moving control surfaces can be achieved when the actuators are placed on the pressure and suction surfaces of the airfoil near the trailing edge. As shown in Figure 4.4, both the pressure surface (*PS*) and suction surface (*SS*) actuators are located near the trailing edge and effect pitch-up and pitch-down moments. The *PS* actuator is located at $x/c = 0.95$ while the effectiveness of the *SS* actuator is investigated at four streamwise positions $(x/c)_s = 0.55$, 0.75, 0.90 and 0.95. The variations in pitching moment (computed from pressure distributions) at $\alpha = 4°$ are shown in Figure 4.5a when the *PS* and *SS* actuators are simultaneously inactive, and individually and simultaneously active. The coupling between the *PS* and *SS* actuators is evident by the general increase in $C_m$ as the *SS* actuator is moved closer to the trailing edge. Compared to the smooth airfoil (which has a downward pitching moment shown with a dashed line), the pitching moment induced by the *PS* actuator becomes almost positive ($C_m = 0.003$) with the *SS* actuator at $(x/c)_s = 0.90$ where the moment increments between the *PS* and *SS* actuators relative to the smooth airfoil are largest (within the investigated range) namely, $\Delta C_m = 1.10 C_{m0}$ and

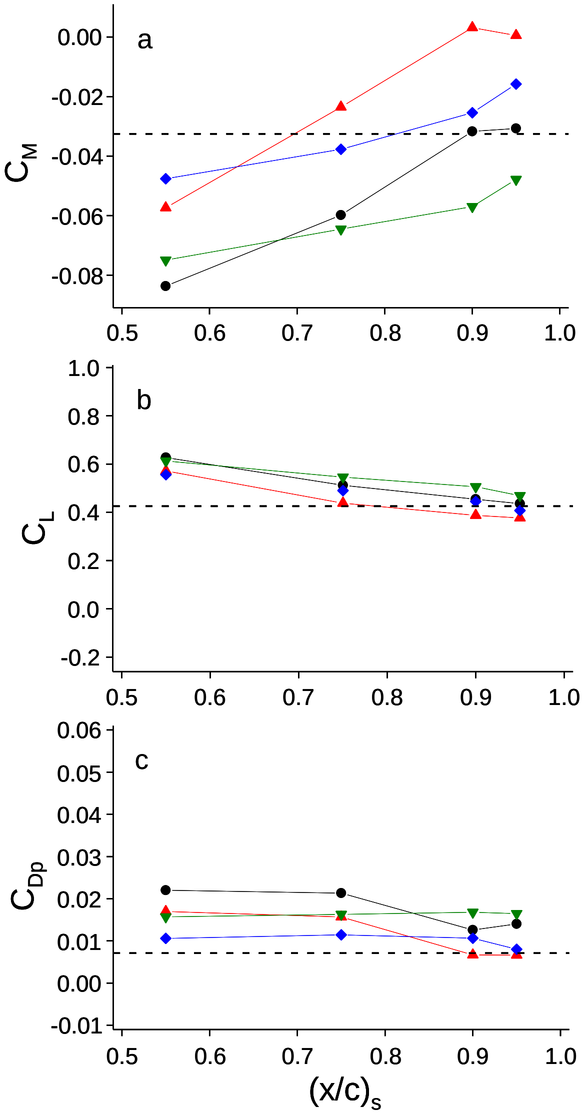

***Figure 4.5**. Variation of (a) $C_m$, (b) $C_l$, and (c) $C_{dp}$ with $(x/c)_s$. (●) Unactuated, (▲) Pressure surface actuator operating only, (▼) Suction surface actuator operating only, (♦) Both actuators operating, (—) Baseline.*

$-0.75C_{m0}$, respectively. Note that simultaneous *PS* and *SS* actuation results in a net pitching moment that is almost the same as for the smooth airfoil. The range of the actuation $\Delta C_m$ decreases slightly when the *SS* actuator is placed at 0.95*c*, ostensibly as a result of the decrease in the size of the trapped vorticity concentration.

The corresponding changes in lift and pressure drag are shown in Figures 4.5b and 4.5c, respectively. It is noteworthy that the presence of the *SS* actuator at $x/c = 0.55$

results in an increment of $\Delta C_l = 0.20$ relative to the baseline, and simultaneously in a substantial increase in pressure drag $\Delta C_{dp} = 0.015$ in the absence of actuation. These effects diminish as the *SS* actuator is moved downstream. It is noteworthy that when only the *SS* actuator is active, the overall pressure drag is almost invariant regardless of the actuator's streamwise position while operation of the *PS* actuator results in pressure drag that is almost the same as the baseline for $(x/c)_s = 0.9$ and 0.95. Although $C_m$ can be varied across a wider range of values with the actuator at 0.90*c* than at 0.95*c*, the drag penalty due to operation of the suction surface actuator is less with the actuator at 0.95*c*; this is particularly true at higher angles of attack, as shown subsequently.

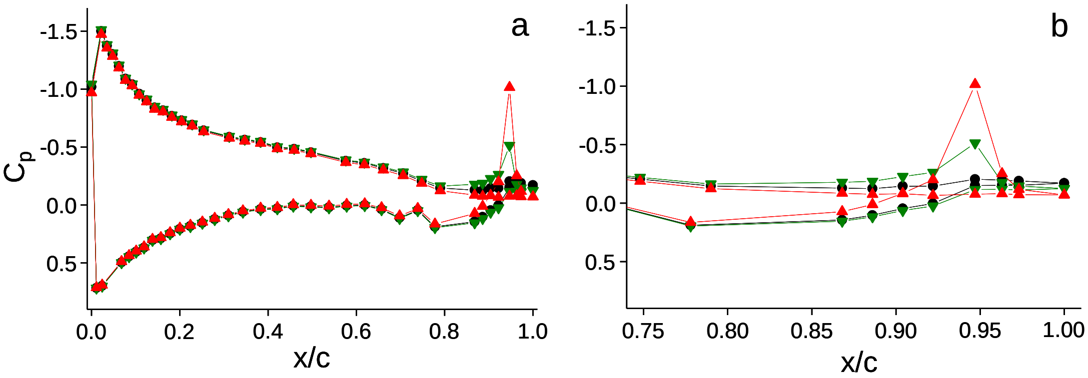

***Figure 4.6***. *Pressure distribution around airfoil at* $\alpha = 6°$ *and* $(x/c)_s = 0.95$. *(a) Global view, (b) trailing edge detail. Symbols as in Figure 4.5.*

Pressure distributions around the airfoil at $\alpha = 6°$ and $(x/c)_s = 0.95$ (Figure 4.6) show that the operation of the pressure surface actuator leads to a pressure increase at the trailing edge of $\Delta C_p \approx 0.1$ that extends to the opposite surface and therefore leads to a pitch-up moment increment. Similar changes in the pressure distribution occur when the suction surface actuator is operated, producing an opposite, nose-down pitching moment. It is evident that the trapped vorticity concentrations induced by the actuation result in a region of low pressure near the trailing edge that accelerates the flow along both the pressure and suction surfaces of the airfoil. Operation of either actuator causes induces a domain of very low pressure in the immediate vicinity of the actuator, accompanied by an increase in pressure downstream of the actuator and at the trailing edge. As a result, the Kutta condition is manipulated so that the flow on the opposite surface from the operating actuator (around the trailing edge) decelerates, leading to increased pressures and a corresponding pitching moment (cf. Figure 4.5). A further contribution to the pitching moment comes from the reduced pressure immediately upstream of the actuator that is created when the actuator operates.

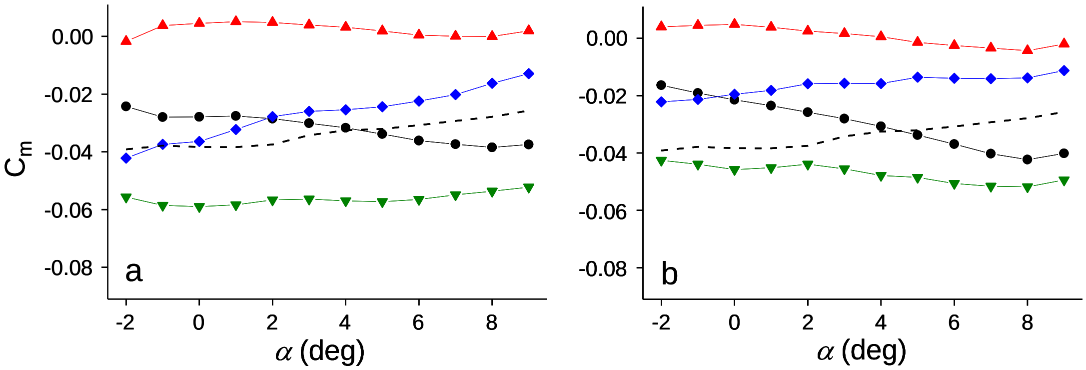

***Figure 4.7**. Variation of $C_m$ with $\alpha$ for $(x/c)_s$ = (a) 0.90c, (b) 0.95c. Symbols as in Figure 4.5.*

Given the sensitivity of $C_\mathrm{m}$ to actuator location (cf Figure 4.5) and in particular the decrease in drag near the trailing edge, the variation of $C_\mathrm{m}$ with angle of attack ($-2^\mathrm{o} < \alpha < 9^\mathrm{o}$) was measured at $(x/c)_\mathrm{s} = 0.90$ and 0.95 (Figures 4.7a and b, respectively) for the baseline airfoil and in the presence of the inactive and active actuators. The overall trends are similar at both locations. To begin with, in the absence of actuation $C_\mathrm{m}$ decreases with $\alpha$ while $C_{\mathrm{m}0}$ (for the baseline airfoil) increases with $\alpha$ indicating that the inactive actuators renders the airfoil slightly more stable as evidenced by the change in $\mathrm{d}C_\mathrm{m}/\mathrm{d}\alpha$ compared to the smooth airfoil. When either one of the actuators (*PS* or *SS*) is active, $C_m$ varies only slightly with $\alpha$. However, while the moment difference between these actuation conditions is also relatively invariant with $\alpha$ ($\Delta C_m = 0.047$ and 0.058 for $(x/c)_s = 0.95$ and 0.90, respectively), the moment increments induced by *PS* and *SS* actuation relative to the unactuated airfoil monotonically decrease and increase, respectively as $\alpha$ increases. For instance, at $(x/c)_s = 0.95$ and $\alpha = 8°$, $\Delta C_m$ (with respect to the unactuated condition) for *PS* and *SS* actuation has respective values of +0.038 and −0.009. The ranges of $C_m$ values that are achievable using actuation alone allow the moment coefficient to be varied between approximately the value of the smooth (unactuated) airfoil and a value corresponding to a (small) nose-up pitching moment. Simultaneous operation of both actuators produces a $\Delta C_m$ (with respect to the unactuated condition) of an amount nearly equal to the combination of the $\Delta C_m$ values of the individual actuators, indicating that the effects of the *PS* and *SS* actuators on $C_m$ are independent of each other.

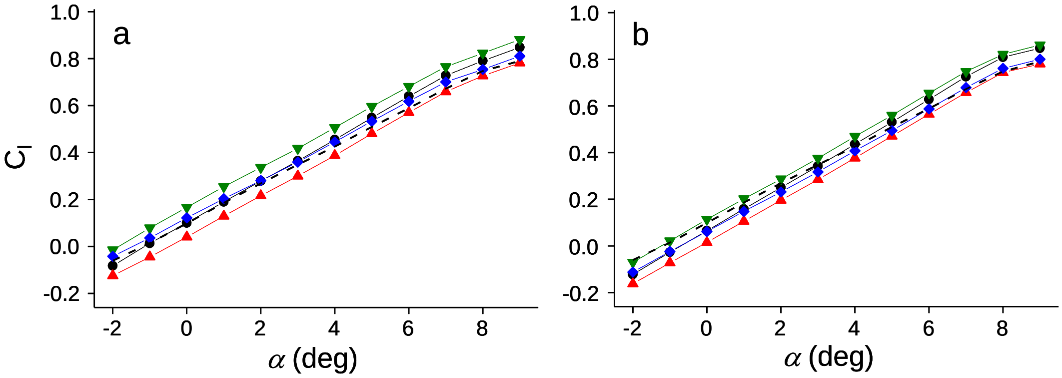

***Figure 4.8**. Variation of $C_l$ with $\alpha$ for $(x/c)_s$ = (a) 0.90c, (b) 0.95c. Symbols as in Figure 4.5*.

The corresponding effects of the actuation on the lift and pressure drag coefficients each measured at $(x/c)_s = 0.90$ and 0.95 are shown in Figures 4.8a and b and and 4.9a and b, respectively. Compared to the unactuated airfoil, operation of either actuator leads to a relative lift increments of $\Delta C_l \approx 0.1$ and 0.12 for $(x/c)_s = 0.9$ and 0.95, respectively, over the range of angles of attack tested. It is noteworthy that compared to the smooth airfoil, at low $\alpha$ the lift is reduced primarily by the *PS* actuator while at high $\alpha$ the lift increases mostly by the *SS* actuator such that $dC_l / d\alpha$ increases when either actuator is operational.

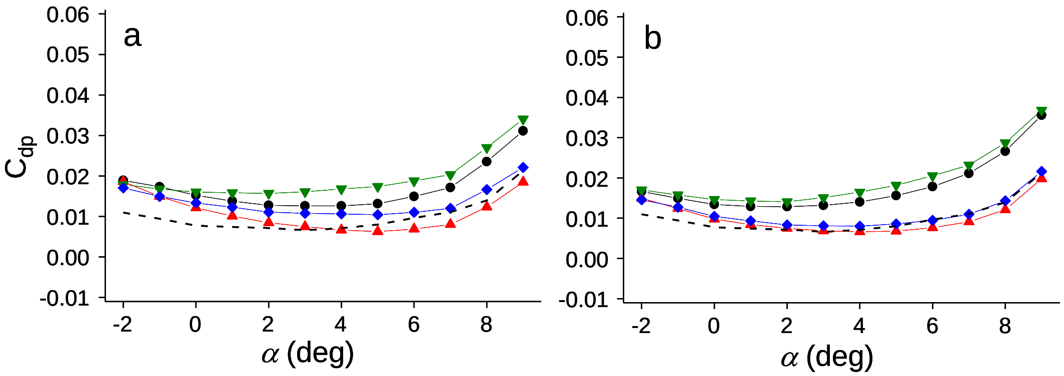

***Figure 4.9**. Variation of $C_{dp}$ with $\alpha$ for $(x/c)_s$ = (a) 0.90c, (b) 0.95c. Symbols as in Figure 4.5.*

The changes in pressure drag induced by the actuation are shown in Figure 4.9. The presence of the inactive actuators leads to an increase in the cross stream width of the near wake resulting in a substantial increase in $C_{dp}$ (50-100% relative to the smooth airfoil). However, as shown in the work of DeSalvo and Glezer (2004), operation of the *PS* actuator can lead to a significant reduction in pressure drag which increases in magnitude with $\alpha$ relative to the smooth airfoil. For example, at $\alpha = 6°$, the pressure drag decreases by 21% when the *SS* actuator is inactive and increases by 17% when the *SS* actuator is active (the latter increase is accompanied by an increase in $C_l$ and a nose down pitching moment). While the distributions of $C_{dp}$ at $(x/c)_s = 0.90$ and 0.95 during operation of the *PS* and *SS* actuators are similar, *SS* actuator operation with $(x/c)_s = 0.90$ induces a pressure drag increase of up to 33% compared to only 17% at $(x/c)_s = 0.95$;

however, the greater drag penalty is offset by a larger range of $C_m$ values that can be achieved with $(x/c)_s = 0.90$.

The aerodynamic effects discussed in chapters 3 and 4 occur as a result of quasi-steady (time-harmonic) actuation waveform. By applying pulse modulation to the actuation waveform at frequencies that are coupled to the instability of the near wake, the actuation authority required to achieve a given change in the aerodynamic characteristics can be reduced as discussed in Chapter 5.

# CHAPTER 5

# PULSE-MODULATED ACTUATION

In order to reduce the active flow control actuation momentum required to realize the aerodynamic improvements modifications demonstrated in Chapters 3-4, it is desirable to couple the actuation to the instability of the near wake (e.g., Amitay and Glezer 2002) by operating the actuator with a pulse-modulated actuation waveform. Because the nonlinear response of the flow effectively demodulates the actuation, oscillation at the pulse modulation frequency is introduced into the flow that couples to the near-wake instability and enhances the effectiveness of the actuation.

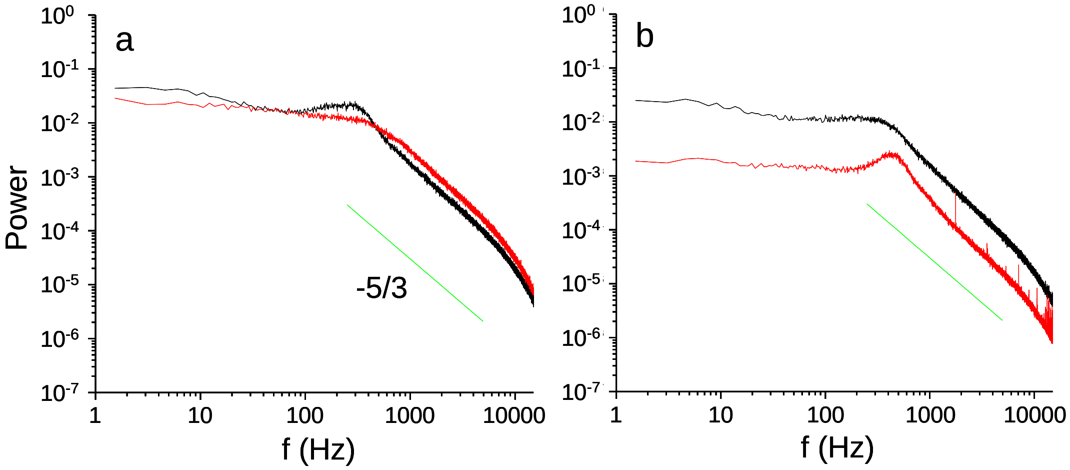

***Figure 5.1***. *Power spectrum of wake 0.25c downstream of trailing edge. (a) Upper wake, (b) Lower wake. Actuator not operating is shown in black, continuous downstream actuation in red.*

The range of receptive wake frequencies (in the absence of stall) is assessed from spectra of the streamwise velocity measured using hot wire anemometry near the upper and lower edges of the wake (Figures 5.1a and b, respectively) at a distance of 0.25*c* downstream of the trailing edge. The unforced spectrum near the top edge shows a discernible frequency band of increased fluctuations between 150-500 Hz, corresponding to Strouhal numbers (based on the airfoil chord) of 4.1-10 and reduced frequencies based on the characteristic scale of the actuator within the range 0.1-0.2. When the downstream actuator is active, the frequency band vanishes and the spectrum becomes featureless. However, the response of the pressure surface side of the wake (Figure 5.1b) is different, and the actuation results in an overall reduction in the magnitude of the spectral components and the appearance of a frequency band between 250-600 Hz which is somewhat higher than in the absence of actuation (note also the spectral peaks at the actuation frequency and its higher harmonics within the dissipation range). As shown subsequently, the wake becomes narrower and, the velocity deficit decreases thereby suggesting that its unstable frequency band is somewhat higher. In what follows, pulsed-modulated actuation is at modulation frequencies $f_{\mathrm{mod}}$ that are within the receptive band of the wake. The pulse repetition rate is variable, and the pulse duration and phase are adjusted so that the beginning and end of every pulse coincide with zero crossings of the actuator resonance waveform.

The variation of the moment, pressure drag and lift coefficients with pulse duration and several repetition (modulation) frequencies of the downstream actuator at $\alpha = 4^{\circ}$ ($Re_c = 1.0\cdot10^6$) when the upstream actuator is inactive is shown in Figure 5.2a. The moment coefficient is largest when the downstream actuator is inactive, and decreases monotonically with increasing pulse duration (continuous actuation is achieved when the duty cycle is 1). At the lowest modulation frequency $St = 0.8$ (corresponding to $f_{\mathrm{mod}} = 50$ Hz), the moment coefficient increases almost linearly with pulse duration from $C_{\mathrm{m}} = -0.067$ until it reaches a maximum of $C_{\mathrm{m}} = -0.049$ at a duty cycle of 0.9 that is only

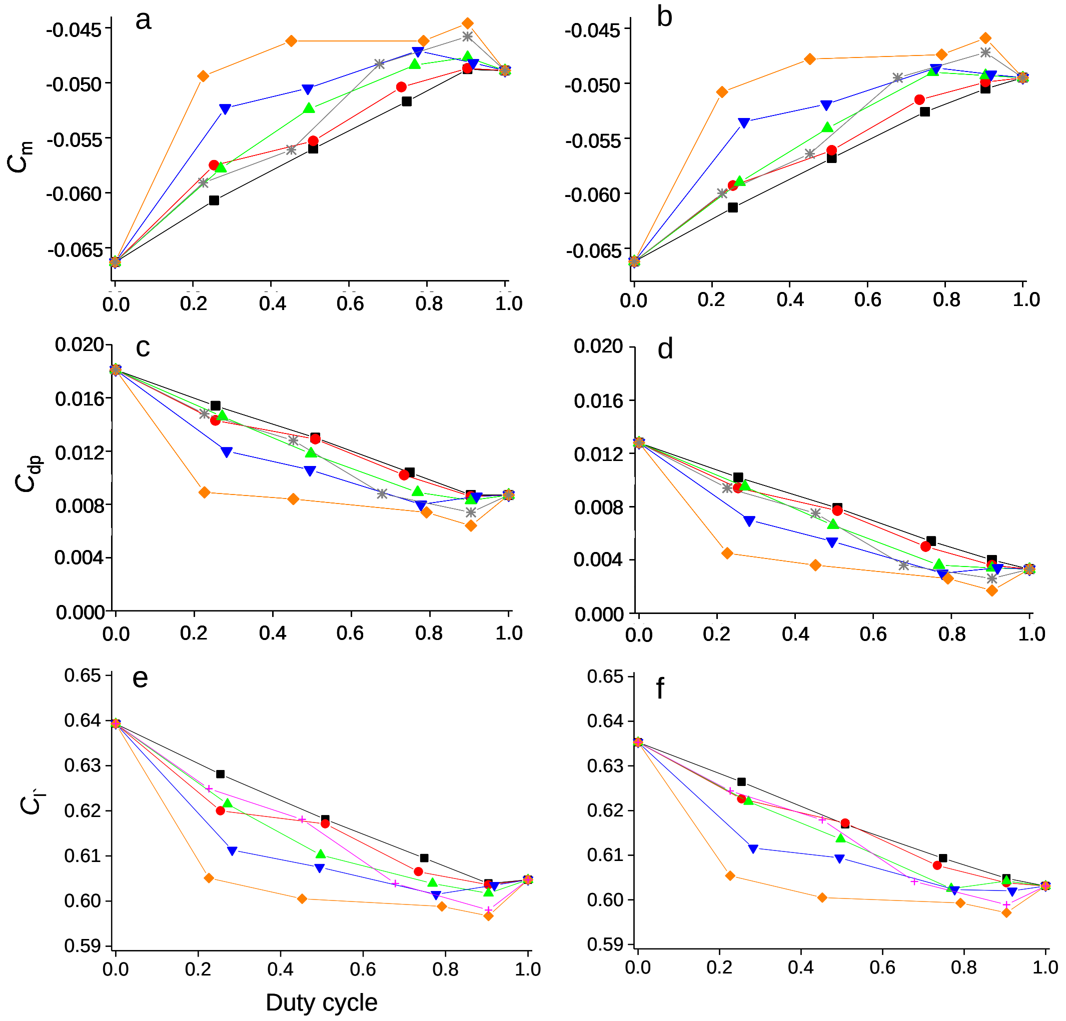

***Figure 5.2**. Variation of (a,b) $C_m$, (c,d) $C_{\underline{dp}}$ and (e,f) $C_l$ with actuator duty cycle. Upstream actuator (a,c,e) inactive, (b,d,f) active. Downstream actuator pulse modulated at St = 0.8 (■), 1.7 (●), 2.7 (▲), 4.2 (▼), 6.7 (♦) , 13.3 (*).*

slightly lower than the level of $C_{\mathrm{m}}$ under continuous actuation. At higher modulation frequencies, the initial rate of increase of $C_{\mathrm{m}}$ becomes larger and then the rate increase diminishes. The highest initial level of $C_{\mathrm{m}}$ is attained with a modulation frequency of $St$ = 6.7 (near the peak of the unstable frequency range of the near wake) and a duty cycle of 0.25. It is important to note that at $St$ = 6.7, the value of $C_{\mathrm{m}}$ is highest at a duty cycle of 0.9 ($C_{\mathrm{m}}$ = -0.045) and that $C_{\mathrm{m}}$ has approximately the same value at a duty cycle of 0.25 as under continuous actuation. These variations in moment remain almost unchanged when the upstream actuator is operational (continuously) as shown in Figure 5.2b. These data show that the effect of the upstream actuator on the sensitivity of the moment to pulse modulation by the downstream actuator is minimal.

The corresponding variation of pressure drag coefficient $C_{\mathrm{dp}}$ with modulation frequency and duty cycle is shown in Figures 5.2c and d in the absence and presence of upstream actuation, respectively. The trends are similar to the data in Figures 5.2a and b. At low modulation frequencies, $C_{\mathrm{dp}}$ decreases monotonically with increased duty cycle; as the modulation frequency is increased, $C_{\mathrm{dp}}$ decreases with modulation frequency. The lowest drag is attained at a reduced modulation frequency of $St = 6.7$, with a decrease of $\Delta C_{\mathrm{dp}} = 0.009$ at a duty cycle of 0.25. It is important to note that the pressure drag at this actuation condition is almost the same as that of the airfoil with continuous (non-pulsed) actuation, which is also approximately equal to the pressure drag of the smooth (baseline) airfoil. When the upstream actuator is activated the pressure drag decreases by $\Delta C_{\mathrm{dp}} \approx 0.006$ (Figure 5.2d) regardless of the operating condition of the downstream actuator. At $St = 6.7$ and a duty cycle of 0.25, the pressure drag is reduced to $C_{\mathrm{dp}} = 0.003$, in comparison to the baseline airfoil pressure drag of $C_{\mathrm{dp}} = 0.009$. Increasing the duty cycle to 0.9 reduces the pressure drag even further to $C_{\mathrm{dp}} = 0.0017$. Compared to continuous actuation of both actuators, with $C_{\mathrm{dp}} = 0.0033$, pulsed modulation of the downstream actuator at a duty cycle of 0.25 (i.e., 25% of the actuation power with the downstream actuator) and $St = 6.7$ with the upstream actuator operating (continuously) results in $C_{\mathrm{dp}} = 0.0045$.

The variation in lift coefficient (Figures 5.2e-f with the upstream actuator inactive and active, respectively) follows similar trends to the pitching moment and pressure drag. At the lowest modulation frequency $St = 0.8$ (corresponding to $f_{\mathrm{mod}} = 50$ Hz), the lift coefficient decreases almost linearly with pulse duration from $C_l = 0.639$ until reaching a minimum of $C_l = 0.604$ at a duty cycle of 0.9 that is only slightly lower than the level of $C_l$ under continuous actuation. At higher modulation frequencies, the initial rate of decrease of $C_l$ becomes larger and then the rate decrease diminishes. The lowest initial level of $C_l$ is attained when the modulation frequency is $St = 6.7$ which is near the peak of the unstable frequency range of the near wake and the duty cycle is 0.25. It is important to note that at $St = 6.7$, the value of $C_l$ is lowest at a duty cycle of 0.9, with a corresponding $\Delta C_l = -0.04$ relative to the unforced condition, and that $C_l$ has approximately the same value at a duty cycle of 0.25 as under continuous actuation. These variations in lift remain almost unchanged when the upstream actuator is operational (continuously) as shown in Figure 5.2f. These data show that the effect of the upstream actuator on the sensitivity of the lift to pulse modulation by the downstream actuator is minimal (the variation in lift when the upstream actuator is activated is no more than $\Delta C_l = \pm 0.005$).

The effect of modulated actuation of the downstream actuator on the pressure distribution around the airfoil (with the upstream actuator inactive) is shown in Figure 5.3. For $St = 6.7$ and duty cycle 0.25, the pressure distribution is nearly identical to that of the airfoil with continuous (unmodulated) actuation, particularly near the trailing edge as shown in detail in Figure 5.3b. As a result, the aerodynamic forces and moments are similar in these cases. Compared to the case of continuous actuation, operating the actuator at $St = 6.7$ and duty cycle 0.9 causes the pressure minimum near the actuator orifice to strengthen by $\Delta C_p = -0.2$, leading to additional flow acceleration upstream of the orifice. Downstream of the actuator and near the trailing edge there is a small

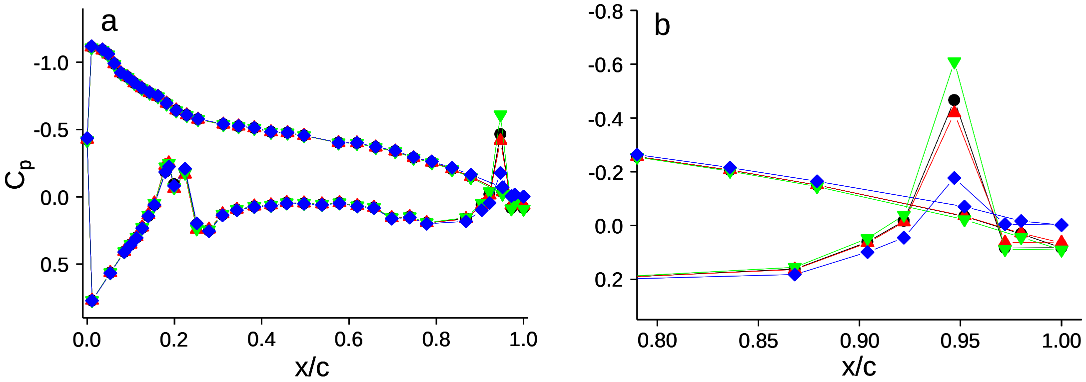

***Figure 5.3***. *Pressure distribution for* $\alpha = 4°$ *and* $Re_c = 1.0{\cdot}10^6$. *(a) Global view, (b) detail view. Downstream actuation (●) Continuous, (▲) St = 1.7 and 25% duty cycle, (▼) St = 6.7 and 25% duty cycle, (♦) St = 6.7 and 75% duty cycle.*

pressure rise of $\Delta C_p = 0.02$, in addition to a small pressure increase on the suction surface between the trailing edge and 0.85*c*. These changes constitute an enhancement of the effects of continuous actuation, leading to an additional reduction in $C_{dp}$, decrease in $C_l$, and increase in $C_m$. By comparison, actuation at *St* = 1.7 and duty cycle 0.25 generates a weaker low pressure domain near the orifice, resulting in smaller changes in the aerodynamic characteristics as shown in Figure 5.2.

An analysis of the temporal variation of the aerodynamic characteristics of the airfoil under pulse-modulated and continuous actuation waveforms is conducted using phase-averaged PIV measurements in the near wake. The phase-averaged velocity field measures 90 x 90 mm and is centered immediately below the trailing edge of the airfoil ~0.05*c* downstream of the trailing edge. These data are used to compute concentrations of the spanwise vorticity $\omega_z$ and thereafter the integral of the vorticity flux across the wake to obtain the global time rate of change of circulation:

$$\frac{d\Gamma}{dt} = \oint_L \omega_z (\bar{v} \cdot \hat{n}) dl$$

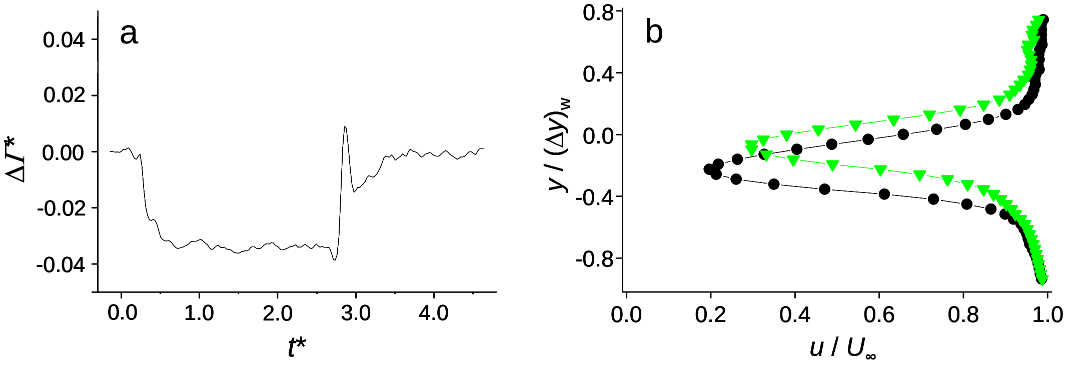

***Figure 5.4**. (a) Variation of circulation. Continuous actuation of downstream actuator begins at $t^* = 0$ and ends at $t^* = 2.4$. (b) Cross-stream velocity profiles of wake. (●) Both actuators inactive, (▼) Downstream actuator active only.*

It is noted that although the integration path $L$ typically surrounds the entire airfoil, the spanwise vorticity normally vanishes everywhere except within the wake. The circulation itself can be obtained from a second integration step.

Figure 5.4a shows the variation of circulation with time when continuous actuation is activated and deactivated at $\alpha = 4°$ and $Re_c = 1.0 \cdot 10^6$ (time is scaled by the convective time scale of the airfoil, $t^* = t/\tau$, where $\tau = c/U_\infty$, and the circulation is scaled by $U_\infty \cdot c/2$). Continuous actuation is initiated at $t^* = 0$ and terminated at $t^* = 2.4$; this is done to provide adequate time for the flow to settle following the change in actuation state. After the initiation of actuation, there is a small increase in the circulation of the airfoil at $t^* = 0.1$ followed by fluctuations, and the primary change in between the unactuated and actuated states begins at $t^* = 0.25$, in which the (scaled) circulation changes by $\Delta\Gamma^* = -0.034$. This change in circulation occurs over a time interval of approximately $\tau$, and is followed by minor fluctuations that decay over the next convective time scale. It is noteworthy that the change in scaled circulation is approximately equal to the change in $C_L$ between the two states (cf. Figure 5.2), using $\Gamma^* = C_L$ for a nominally *steady* flow. However, it is clearly not possible to relate the changes in circulation to the *unsteady* lift during the transient period using the steady formulation. Approximately $0.25\tau$ after the termination of actuation ($t^* = 2.4$), there is another small change in the circulation, followed by a very rapid rise over $0.1\tau$ to a level that is 0.01 greater than the scaled circulation for the airfoil without actuation. The circulation returns to its value for the unactuated airfoil within $\tau$ of the termination of actuation. As shown in chapter 4, the actuation also results in substantial reduction in drag. These changes are also apparent in the wake where the maximum velocity deficit is reduced by 13% ($0.1U_\infty$) and the wake width decreases by ~10% as a result of the actuation (Figure 5.4b). At the same time, the upward shift in the wake is commensurate with the small reduction in lift.

In general, activations and deactivations of the trailing edge actuator separated by relatively long settling times generate circulation transients of duration $1\text{-}2\tau$ after which $\Gamma^*$ settles to a steady state value. Within the transients, the most rapid circulation changes occur during an interval of duration $0.1\text{-}0.25\tau$, which is also in the range of the period associated with the wake receptivity as discussed in connection with Figure 5.1. These results suggest that it might be possible to drive the transitory changes in actuation (using pulse modulation of the trailing edge actuator on the same timescale as the observed circulation) and thereby couple them to the instability of the near wake so that the desired changes in circulation can be attained at lower actuation power.

The variation of circulation following the initiation (at $t^* = 0$) of pulsed modulated actuation of the trailing edge actuator ($\alpha = 4^\circ$ and $Re_c = 1.0 \cdot 10^6$) for $St_{\mathrm{mod}} = 1.7$ at duty cycles of 0.25 and 0.75 are shown in Figures 5.5a, and b, respectively. In Figure 5.5a (duty cycle 0.25), the actuator is active for $0.15\tau$ and the circulation decreases rapidly

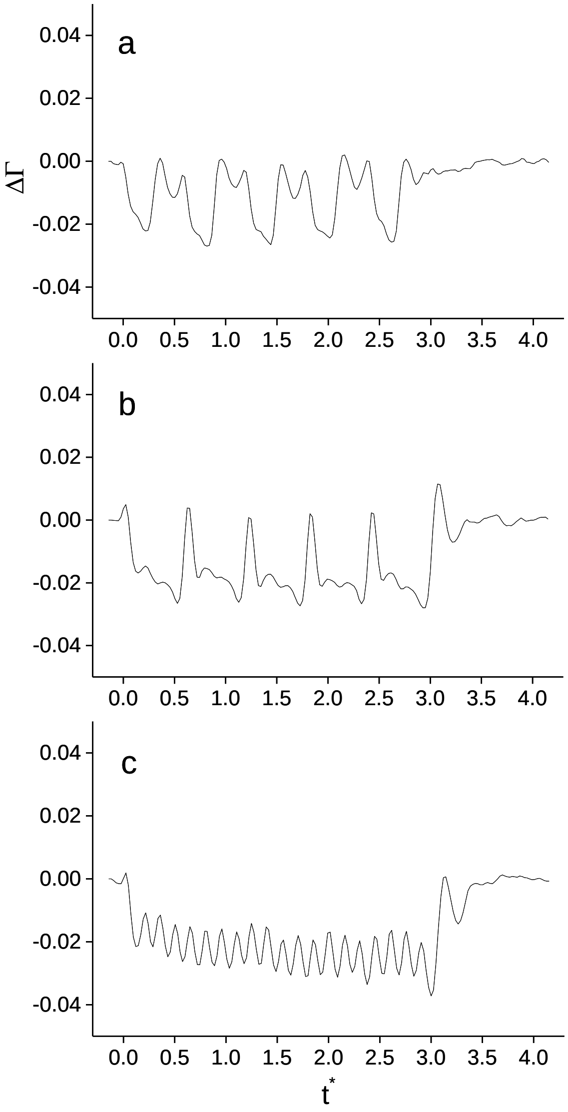

***Figure 5.5**: Time variation of circulation. Downstream actuation at (a) St = 1.7 and 0.25 duty cycle, (b) St = 1.7 and 0.75 duty cycle, (c) St = 6.7 and 0.25 duty cycle beginning at t* = 0 and ending at t* = 3.0.*

following each modulation pulse. When the actuator is inactive ($0.45\tau$), the circulation fluctuates in a manner that is similar to the variation following actuator termination shown in Figure 5.4a. Following the initial pulse the circulation changes by $\Delta\Gamma^* = -0.022$ before rising and in subsequent pulses the circulation varies by as much as $\Delta\Gamma^* \approx 0.03$ indicating that there is a longer, global time scale over which the circulation adjusts over the entire airfoil. Following the termination of the modulation pulse train at

$t^*$ = 2.55, there is a transient change in circulation over the next 0.9$\tau$ that is comparable to the changes following the termination of unmodulated actuation as shown in Figure 5.4a. When the duty cycle is increased to 0.75 (Figure 5.5b), the actuator is active for 0.45$\tau$ and inactive during the next 0.15$\tau$. It is noteworthy that the nominal change in circulation during each modulation pulse increases slightly with time over the first 2-3 pulses and the circulation increases rapidly and briefly (for ~0.2$\tau$) between pulses.

The response of the circulation is markedly different when the modulation frequency is within the receptive band of the near wake. Figure 5.5c shows the effects for $St_{\mathrm{mod}} = 6.7$ at duty cycle 0.25 (period of 0.15$\tau$). This is the modulation frequency for which pulse modulation at duty cycle 0.25 results in nearly the maximum aerodynamic performance at reduced power level. At this duty cycle the circulation oscillates at the modulation frequency but the oscillation amplitude is *lower* than the full excursion that shown in Figures 5.4a-b ($St_{\mathrm{mod}} = 1.7$) and the nominal mean for $t^* > 1.5$ is $\Delta\Gamma^* \approx -0.025$. As shown in Figure 5.2, the actuation causes the time-averaged lift coefficient to change by $\Delta C_L = -0.035$. These data suggest that by exploiting the interaction of the transients with the flow near the trailing edge it should be possible to tune the modulation frequency such that the amplitude of the oscillating circulation becomes even lower and virtually time-invariant.

The effect of the modulation frequency on the structure of the wake is determined from the time-dependent magnitude and the corresponding cross stream elevation of the maximum velocity deficit (at 0.05$c$ downstream of the trailing edge) as shown in Figures 5.6a-f. When the actuation waveform is unmodulated (Figures 5.6a and b), the onset of the actuation at $t^* = 0$ results in a large transitory overshoot deficit decrease from $0.78U_\infty$

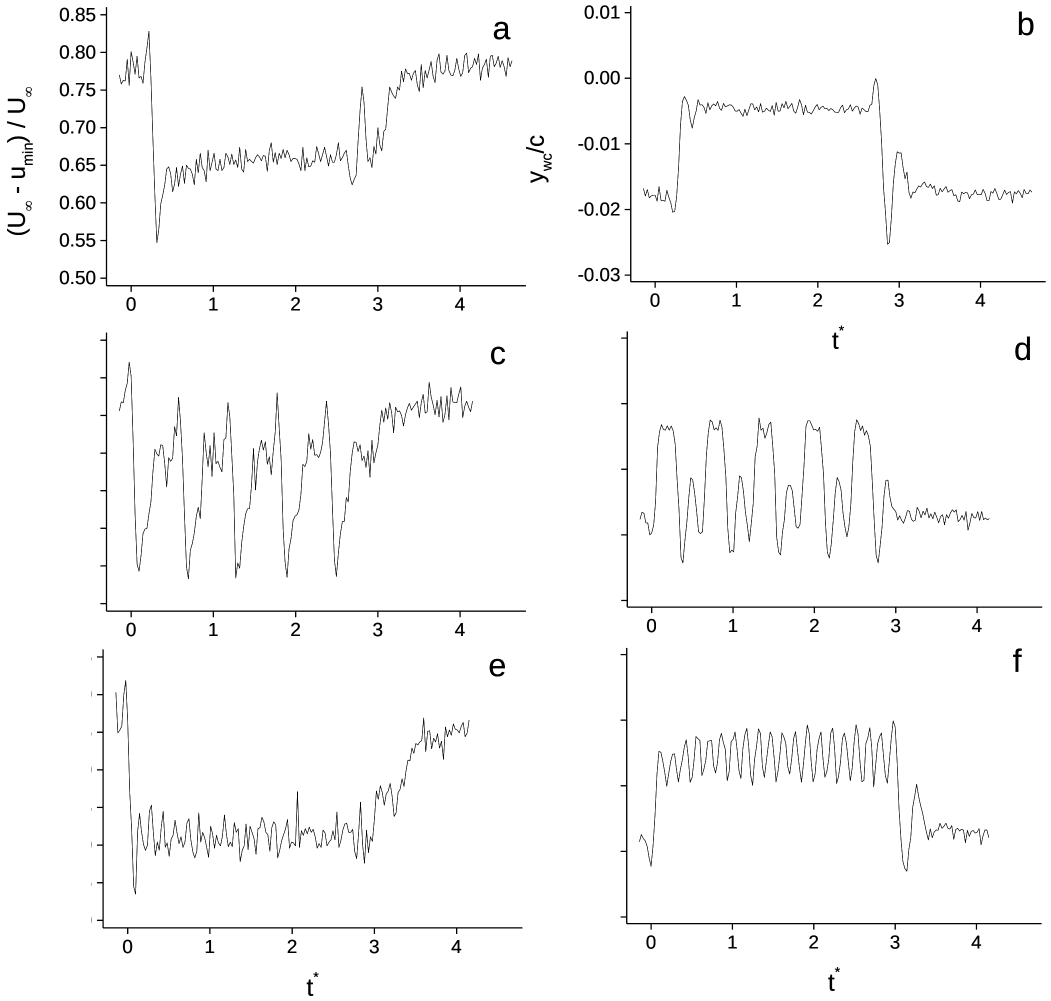

*__Figure 5.6__. Time variation of maximum velocity deficit (a, c, e) magnitude and (b, d, f) location. (a, b) Continuous actuation between t* = 0 and t* = 2.4; (c, d) St = 1.7 and 25% duty cycle; (e, f) St = 6.7 and 25% duty cycle.*

to $0.55U_\infty$ which settles within $1.5\tau$. Upon termination of the actuation at $t^* = 2.4$, there is another transitory change followed by a settling period that occur on timescales similar to those found during the activation transient. The corresponding time-dependent cross stream elevation of the maximum deficit scaled by the width of the wake $(\delta y)_w$ in the absence of actuation (Figure 5.6b) shows that following the onset of actuation the wake to moves up (i.e., closer to the trailing edge), by $\Delta(y/(\delta y)_w) = 0.15$. When the actuator is deactivated, the wake returns to its original elevation. The time-series of the maximum deficit and its elevation when the actuation waveform is pulse modulated is striking. In Figures 5.6c-d and e-f, the duty cycle is 0.25 and the modulation frequencies are $St = 1.7$ and 6.7, respectively. These data clearly demonstrate that as the modulation frequency approaches the locally unstable wake frequency, the magnitude of the oscillations diminishes significantly and the maximum velocity deficit seems to be “locked” to the state that is normally achieved by continuous actuation (e.g., Figure 5.6a). Furthermore, the magnitude of the nominally invariant maximum velocity deficit during the actuation is actually *lower* ($0.62U_\infty$) than when the actuation is continuous ($0.66U_\infty$) and the settling time appears to be shorter.

Pulse-modulated actuation coupled to the instability of the near wake is applied to a configuration with actuators mounted to both sides of the trailing edge (cf. Chapter 4) as discussed in Chapter 6. Alternate operation of the actuators enables the pitching moment to be continuously varied across a range of values (by varying the duty cycle to each actuator) while reducing the actuator power required by coupling to the wake instability.

# CHAPTER 6

# BI-DIRECTIONAL PITCH ACTUATION AT THE TRAILING EDGE

An effective form of bi-directional pitching moment control can be achieved by the *superposition of two hybrid actuators near the trailing edge* and using pulse-modulated actuation to couple the actuation to the instability of the near wake (cf. Chapter 5) in order to maximize the control authority of the actuators. Because the pitching moment change from a single trailing-edge-mounted actuator is unidirectional (cf. Chapter 4), two actuators on opposite sides of the trailing edge are used to vary the pitching moment in both directions. Operating the actuators using alternating pulse modulation with variable duty cycle allows the actuation to be coupled to the near-wake instability while permitting the pitching moment to be continuously varied without requiring the actuators to be operated at reduced (steady state) power levels.

As discussed in Chapter 3, the aerodynamic characteristics of the airfoil can be continuously varied simply by adjusting the actuator momentum coefficient $C_\mu$ through the amplitude of the actuation waveform. However, this variation is nonlinear and is clearly dependent on the characteristics of the actuator (e.g. at very low actuation amplitudes the jet formation may be unstable). For these reasons it is useful to operate the actuator using pulse width modulation and vary its duty cycle for a given $C_\mu$. By exploiting transitory effects, pulse modulated actuation can yield aerodynamic performance that is equal to or greater than what is achieved with continuous (unmodulated) actuation with lower actuation power. The effects of actuation increase

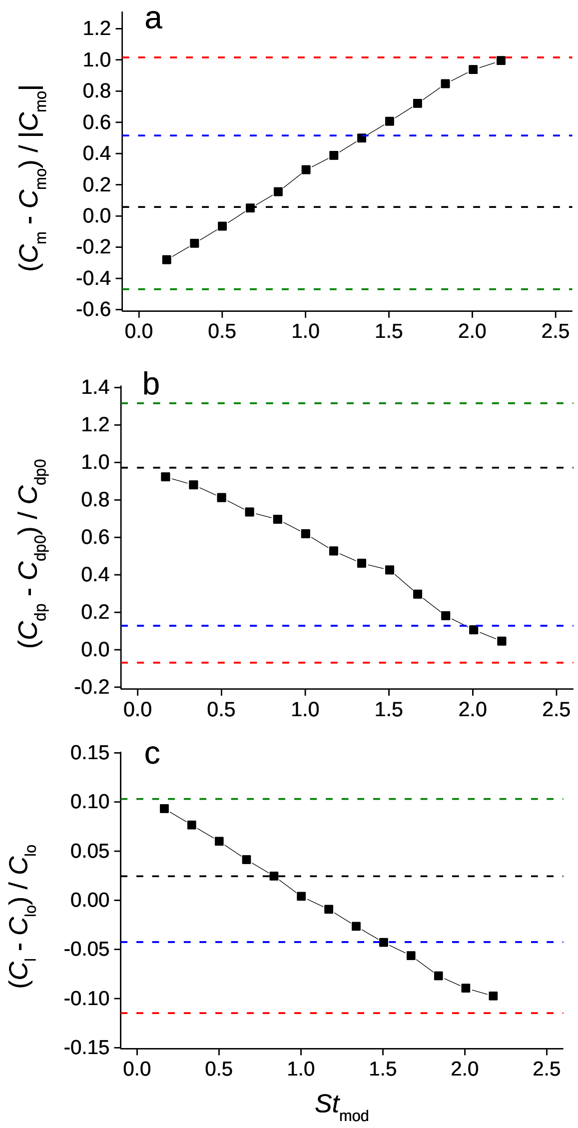

***Figure 6.1****. Variation of (a) ($\Delta C_m / |C_{mo}|$), (b) ($\Delta C_{dp} / |C_{dpo}|$) and (c) ($\Delta C_l / |C_{lo}|$), operating pressure surface actuator in pulses of duration 0.42τ and suction surface actuator the remainder of the time (■). Unmodulated actuation: (—) Unactuated, (—), Pressure surface actuation only, (—) Suction surface actuation only, (—) Both actuators operating.*

with increasing duty cycle, and seem to peak when the modulation frequency is commensurate with the unstable frequencies of the near wake.

These considerations suggest that alternating pulse modulated operation of the two actuators can yield desired, controllable variation in the aerodynamic performance. In the present implementation, complementary pulse-modulated actuation waveforms are applied to the *SS* and *PS* actuators in order to vary $C_\mathrm{m}$ between the levels of pitching moment that are generated by continuous operation of either individual actuator. As shown in connection with Figure 4.7a, the achievable pitching moments are almost invariant across a broad range of angles of attack when the baseline flow is fully attached. Therefore, the *PS* and *SS* actuators are operated at actuation levels that correspond to the minimum and maximum levels of $C_\mathrm{m}$ and are pulse modulated *complementary* to each other at variable duty cycle such that only one actuator is active at any one time to produce a continuous variation in the magnitude of $C_\mathrm{m}$. Based on transitory response of $\Gamma^*$ in Figure 5.4a, the modulation (or repetition) frequency of the (pulse) modulating waveform is selected so that the *PS* actuator is operated for $0.42\tau_\mathrm{conv}$ of each modulation period while the *SS* actuator is operating the remainder of the time.

The aerodynamic effects of complementary pulse modulated actuation at $\alpha = 4^\mathrm{o}$ are shown in Figure 6.1, where the $St_\mathrm{mod}$ indicates the dimensionless repetition (modulating) frequency which can be varied between 0, corresponding to continuous operation of the *SS* actuator, and 2.38 which corresponds to continuous operation of the *PS* actuator. The variation of $\Delta\hat{C}_\mathrm{m} = (C_\mathrm{m} - C_\mathrm{mo}) / |C_\mathrm{mo}|$ with $St_\mathrm{mod}$ is shown in Figure 6.1a. The most striking feature of this distribution is the almost-linear variation of $\Delta\hat{C}_\mathrm{m}$ with the modulation frequency. For $St_\mathrm{mod} = 0.17$, $\Delta\hat{C}_\mathrm{m} = -0.28$ which is 40% lower than the level achieved under continuous *SS* actuation ($\Delta\hat{C}_\mathrm{m} = -0.47$). As the repetition frequency is increased, $\Delta\hat{C}_\mathrm{M}$ increases monotonically up to $\Delta\hat{C}_\mathrm{m} = 0.99$ at $St_\mathrm{mod} = 2.17$, which is near the level for continuous *PS* actuation ($\Delta\hat{C}_\mathrm{m} = 1.02$). Therefore, pulse modulated actuation can be used to continuously vary $C_\mathrm{m}$ across a range spanning $1.28|C_\mathrm{mo}|$. It is noteworthy that the application of pulse width modulation also alters the

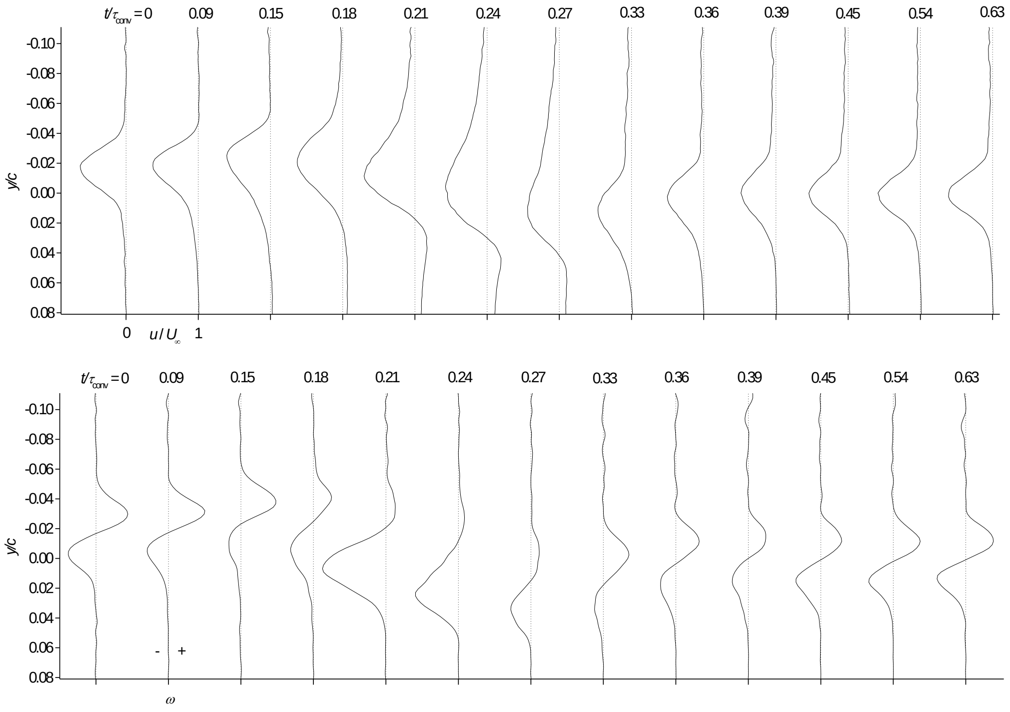

***Figure 6.2**. Wake profiles following transition from pressure surface to suction surface actuation at $t/\tau_{conv} = 0$: (upper) streamwise velocity, (lower) spanwise vorticity.*

corresponding changes in pressure drag (Figure 6.1b). As shown in Figure 4.9, operation of the *PS* actuator leads to a substantial reduction in drag compared to the unactuated airfoil to levels that are comparable to the pressure drag of the smooth airfoil, and compensates for the small drag increase associated with the inactive *SS* actuator. When pulse width modulation is used, the normalized drag increment $\Delta\hat{C}_{dp} = \Delta C_{dp} / C_{dpo}$ at $St_{mod} = 2.17$ is almost the same as for continuous *PS* actuation ($\Delta\hat{C}_{dp} = -0.07$). However, at lower $St_{mod} = 0.17$, when $\Delta\hat{C}_m$ is nearly equal to the level achieved by continuous *SS* actuation, the normalized pressure drag is $\Delta\hat{C}_{dp} = 0.92$ which is 30% *lower* than the value for continuous *SS* actuation of 1.32. This suggests that brief pulses of the *PS* actuator (combined with interruptions of the *SS* actuator) can be used to mitigate the pressure drag increase that occurs due to continuous *SS* actuation. As a result, for $0.17 < St_{\mathrm{mod}} < 2.17$ $C_{\mathrm{m}}$ can be varied over nearly the same range of levels as with continuous actuation but with lower drag penalty. As shown in Figure 6.1c, the normalized lift varies monotonically between $-0.097 < \Delta C_{\mathrm{l}} / C_{\mathrm{lo}} < 0.093$, compared to the respective continuous *SS* and *PS* values of 0.10 and −0.11.

The evolution of the flow field near the trailing edge under alternating pulse-modulated actuation is assessed from phase-averaged particle image velocimetry (PIV) with a field of view measuring 140 x 140 mm that is centered about a location 0.05*c* downstream of, and at the same vertical position as, the trailing edge. These data are used to compute the spanwise vorticity concentrations $\omega_z$ and thereafter the integral of the vorticity flux across the wake to obtain the global time rate of change of circulation $d\Gamma/dt = \oint_L \omega_z (\bar{v} \cdot \hat{n})\, dl$ in a similar process to the method described in chapter 5.

The temporal evolution of the near wake following a switch between the two actuators (i.e., step deactivation of the *PS* actuator and simultaneous step activation of the *SS* actuator) is inferred from a series of phase-averaged cross-stream distributions of streamwise velocity and spanwise vorticity measured 0.09*c* downstream of the trailing edge at $\alpha = 4^{\circ}$ (Figures 6.2a and b, respectively). Before the *PS* actuation is terminated (at $t/\tau_{\mathrm{conv}} = 0$, where $\tau_{\mathrm{conv}} = c/U_{\infty}$ is the characteristic convective time scale) and while the *SS* actuator is inactive, the wake has a nominal width of 0.09*c* and maximum velocity deficit of $0.63U_{\infty}$. The simultaneous respective activation and deactivation of the *SS* and *PS* actuators leads to a brief, upward tilt of the wake ($\Delta y = +0.005c$ between $t/\tau_{\mathrm{conv}} = 0$ and 0.15), followed by broadening of the lower segment of the wake. It is noteworthy that while initially ($t/\tau_{\mathrm{conv}} = 0$) the cross stream distribution of spanwise vorticity (Figure 6.2b) is almost symmetric about the wake centerline (even though the bottom, *PS* actuator is active), the wake tilt and broadening are accompanied by a reduction in the magnitude of the CCW (negative) vorticity layer associated with the pressure side of the airfoil that is followed by a substantial increase in concentration of CCW vorticity at $t/\tau_{\mathrm{conv}} = 0.21$ as vorticity trapped by the *PS* actuator is released and shed into the wake. At the same time, following the activation of the *SS* actuator, it appears that flux of CW (positive) vorticity from the suction surface is momentarily reduced indicating accumulation downstream of the actuator and is indicative of an increase in lift (cf. Figure 4.8). During these changes in vorticity concentrations, the wake tilts toward the pressure surface by as much as $\Delta y = -0.035c$ (relative to the cross stream position at $t/\tau_{\mathrm{conv}} = 0$) at $t/\tau_{\mathrm{conv}} = 0.27$. Subsequently, the wake begins to recover from the transients associated with the change in actuation, tilts upward, regains its symmetry, and the vorticity fluxes from the top and bottom surfaces of the airfoil become approximately equal. In its final stable form, as shown at $t/\tau_{\mathrm{conv}} = 0.63$, the wake is displaced toward the pressure surface by $\Delta y = -0.020c$ relative to its cross stream position at $t/\tau_{\mathrm{conv}} = 0$ and has the same nominal width.

Transitory changes in the normalized circulation around the airfoil $\Gamma^* = \Gamma / (U_\infty \cdot c/2)$ (calculated from the vorticity flux) when the actuation is switched between the *PS* and *SS* actuators are shown in Figure 6.3. When the actuation is switched from the *PS* to *SS* actuators (Figure 6.3a), the rise in circulation is preceded by a small decrease at $t/\tau_{\mathrm{conv}} = 0.12$ which occurs as a result of a momentary accumulation of CCW vorticity near the *PS* actuator while shedding of CW vorticity from the suction side

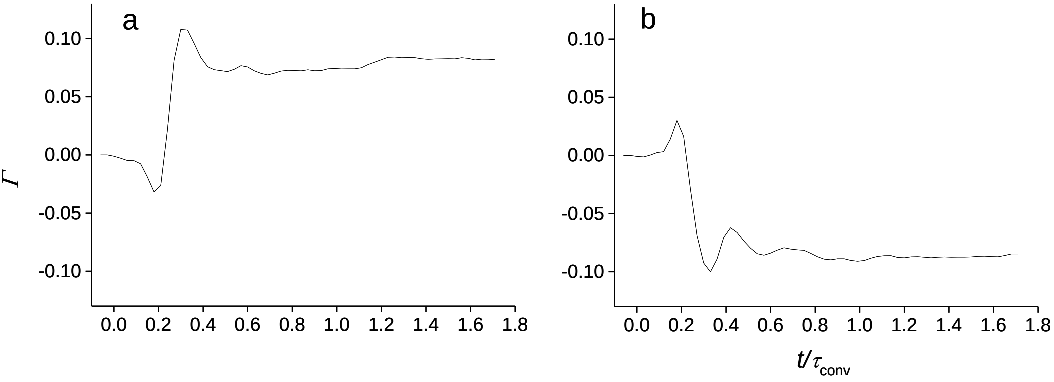

***Figure 6.3***. *Time-dependent circulation. Actuation changing from (a) pressure surface to suction surface, (b) suction surface to pressure surface.*

continues (cf. Figure 6.2b). Subsequently, a significant concentration of accumulated CCW vorticity is shed and there is a decrease in the CW vorticity (cf. Figure 6.2b), which results in an increase in circulation beginning at $t/\tau_{\mathrm{conv}} = 0.21$ over a period of $0.15\,\tau_{\mathrm{conv}}$ and an overshoot of 32% relative to the final stationary level. When the actuation is switched from the *SS* to the *PS* actuators (Figure 6.3b), the drop in circulation and corresponding decrease in lift is preceded by an initial increase in circulation suggesting an initial increase in trapped CW vorticity (a similar rise was observed by Amitay and Glezer (2006) during the termination of actuation for an airfoil at post-stall angle of attack). The initial increase is followed by a large transitory reduction in circulation as a result of accumulation of CCW vorticity by the *PS* actuator before the circulation settles to a lower stationary level. The circulation undershoot and overshoot and some oscillations that follow the primary transition in circulation may be coupled to a near wake instability having a characteristic period of $0.15\,\tau_{\mathrm{conv}}$ (cf. DeSalvo and Glezer 2006). The overall change in the level of the scaled circulation ($\Delta\Gamma^* = 0.082$, i.e. $0.19C_{L0}$) between the two stable actuation conditions corresponds approximately to the change in

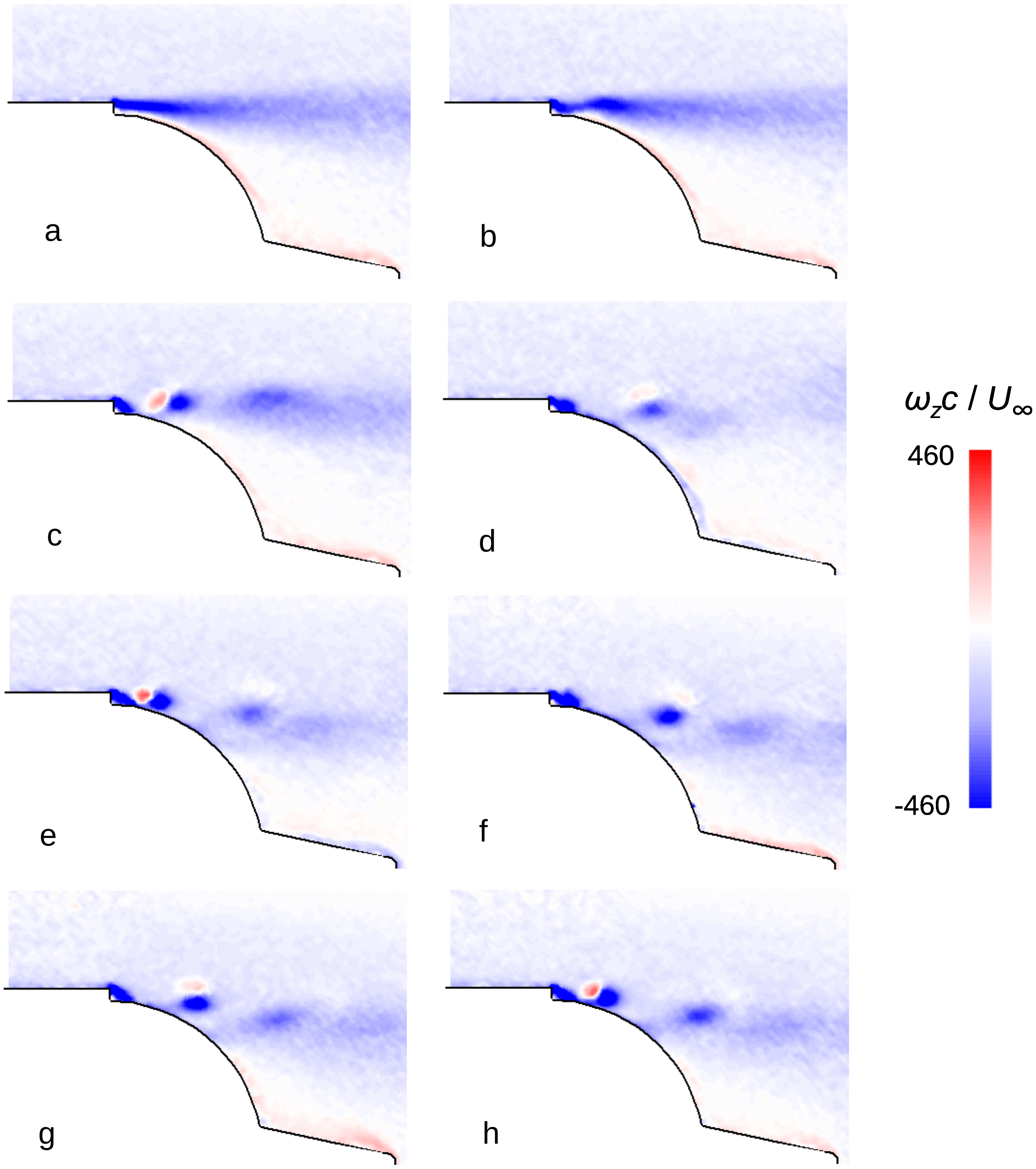

*Figure 6.4*. *Vorticity fields following initiation of actuation at* $t/\tau_{conv} = 0$*:* $t/\tau_{conv}$ *= (a-h) 0, 0.03, 0.06, 0.12, 0.18, 0.30, 0.42, 0.54.*

$C_L$ (cf. Figure 4.8), assuming that $\Gamma^* = C_L$ for nominally *steady* flow (though $\Gamma^*$ does not correspond with the variation of *unsteady* lift during the transient period).

The effects of the initiation of actuation on the flow field in the immediate vicinity of the suction actuator are shown in the maps of vorticity concentrations (Figure 6.4) that are measured phase-locked to the actuation waveform (the imaged field measures 32 x 32 mm, and the magnification is 33 μm/pixel). It should be noted that the cross stream height of the turbulent boundary layer upstream of the actuator orifice (located at $x/c = 0.95$) extends well above the top end of the image and therefore the CW (blue) vorticity layer above the surface upstream of the actuator extends through the top edge of the frame. Prior to the onset of actuation (at $t/\tau_{\mathrm{conv}} = 0$**)**, there is a layer of CW vorticity that is detached from the wall downstream of the actuator orifice (Figure 6.4a) and is accompanied by a recirculating flow (trapped vorticity) domain that produces a thin layer of CCW (red) vortictity along the wall. At $t/\tau_{\mathrm{conv}} = 0.03$ (Figure 6.4b), the activation of the actuator disrupts the separated layer and leads to the shedding of a concentration of CW vorticity into the wake which consequently results in a momentary reduction in lift (cf. Figure 6.3a). A counterrotating vortex pair forms near the actuator orifice, as seen at $t/\tau_{\mathrm{conv}} = 0.06$ (Figure 6.4c) and begins to propagate downstream while farther downstream ($\Delta x \approx 0.025c$ downstream of the actuator) the remnants of the separated vorticity layer (that was present at $t/\tau_{\mathrm{conv}} = 0$) are shed into the wake. A portion of the CW vorticity produced by the actuator remains attached to the wall ($t/\tau_{\mathrm{conv}} = 0.12$; Figure 6.4d), reducing the size of the vorticity domain downstream of the actuator and leading to an overall rise in (time-averaged) vorticity concentrations near the actuator. The CCW vortex induced by the actuator has diminished in strength and advected above the considerably stronger CW vortex, which is relatively close to the wall. Continued operation of the actuator causes additional vortex pairs to form at the actuator and persist briefly before they are advected downstream. As a result of the actuation, the flow near the trailing edge is turned toward the airfoil surface while CW vorticity concentrations are shed into the wake (Figures 6.4e-h).

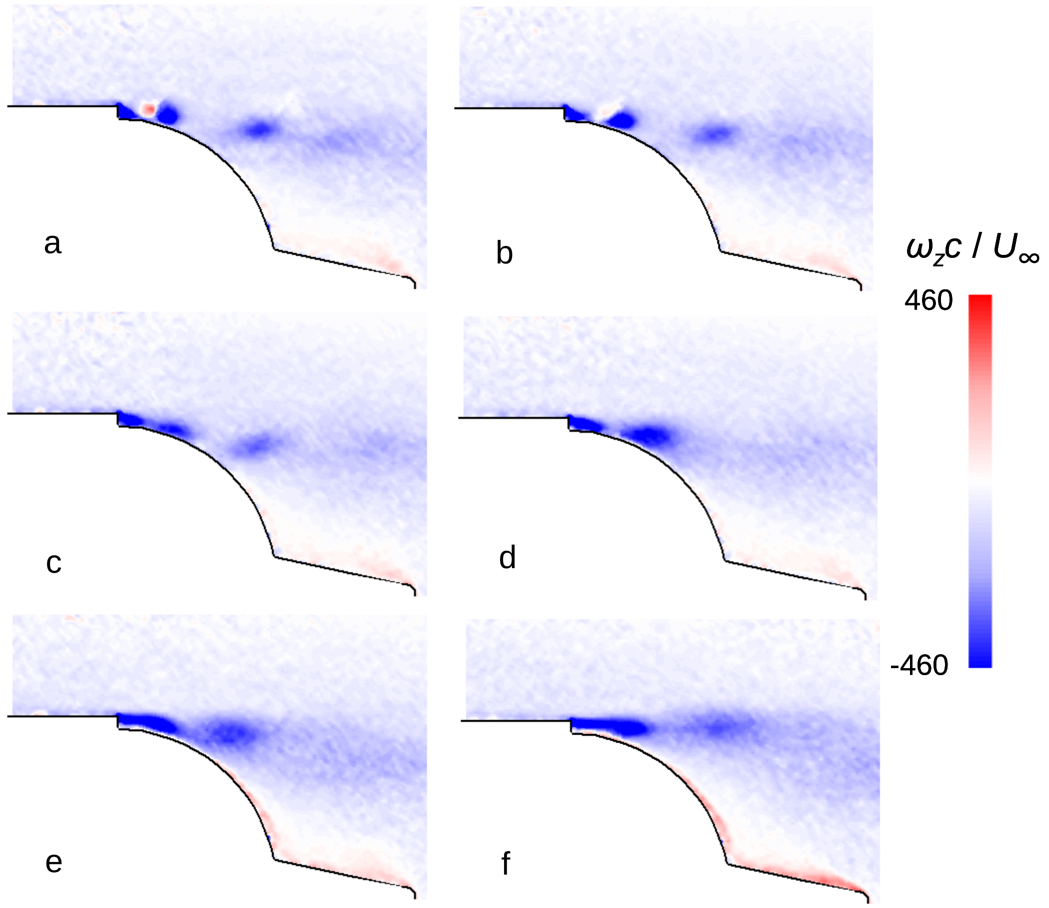

***Figure 6.5**. Vorticity fields following termination of actuation at $t/\tau_{conv} = 0$: $t/\tau_{conv}$ = (a-f) 0, 0.03, 0.06, 0.09, 0.15, 0.21.*

Similarly, Figure 6.5 shows the evolution of the vorticity field following the *termination* of actuation on the suction surface (Figure 6.5a). The separated vorticity layer downstream of the actuator begins to reform at $t/\tau_{\text{conv}} = 0.03$ (Figure 6.5b) and becomes more apparent by $t/\tau_{\text{conv}} = 0.06$ (Figure 6.5c); however, it has not yet stabilized, as indicated by the interruption downstream of the actuator orifice. During this time the separation point (located near the point where the sense of the wall vorticity changes) remains in the same approximate location. By $t/\tau_{\text{conv}} = 0.09$ (Figure 6.5d) the concentration of CW vorticity downstream of the interruption has started to detach from the wall, while the separation point along the wall moves upstream. The vorticity concentration propagates downstream, becomes detached from the wall by $t/\tau_{\mathrm{conv}} = 0.15$ (Figure 6.5e), and continues to be advected into the wake at $t/\tau_{\mathrm{conv}} = 0.21$ (Figure 6.5f) while the vorticity layer stabilizes near the actuator. After a period of $t/\tau_{\mathrm{conv}} \sim 1$(cf. Figure 6.3), the flow settles into the configuration shown in Figure 6.4a.

The use of active flow control for enhancement of the aerodynamic characteristics of airfoils with large-scale separation domains is discussed Chapters 7-9. In Chapter 7, the performance of an airfoil with a deployed high-lift flap is enhanced by using flow control actuation based on fluidically oscillating jets to mitigate separation and increase lift.

# CHAPTER 7

# SEPARATION CONTROL ON A HIGH-LIFT AIRFOIL WITH A SIMPLE FLAP

Active flow control can be incorporated into an airfoil to mitigate larger-scale domains of separated flow and thereby lead to significant improvements in aerodynamic performance. The flow over an airfoil with a deployed trailing-edge flap is characterized by the presence of a separated flow domain over the flap suction surface that typically develops near the juncture between the airfoil elements and reduces circulation, leading to reduced lift. As demonstrated by DeSalvo and Glezer (2010, 2011, 2014) placement of an array of integrated fluidic oscillators a short distance upstream (O[0.01$c$]) of the juncture can effectively diminish the extent of separation and lead to significant enhancement in lift. The physical mechanisms and aerodynamic effects associated with the use of active flow control on high-lift systems are discussed in Chapters 7-9. In this chapter, an array of fluidically oscillating jets is used to mitigate separation over the suction surface of a simple flap on a high-lift airfoil. A similar configuration containing zero-net-mass-flux actuators (synthetic jets; cf. Chapter 2) is investigated in Chapter 8 and compared to the fluidic oscillator configuration. The physical mechanism through which actuator jets reduce the extent of flow separation on the flap suction surface is also investigated. Chapter 9 describes the use of active flow control to mitigate separation on a Fowler flap by enhancing the effectiveness of the bleed flow through the cove between the high-lift elements in maintaining flow attachment.

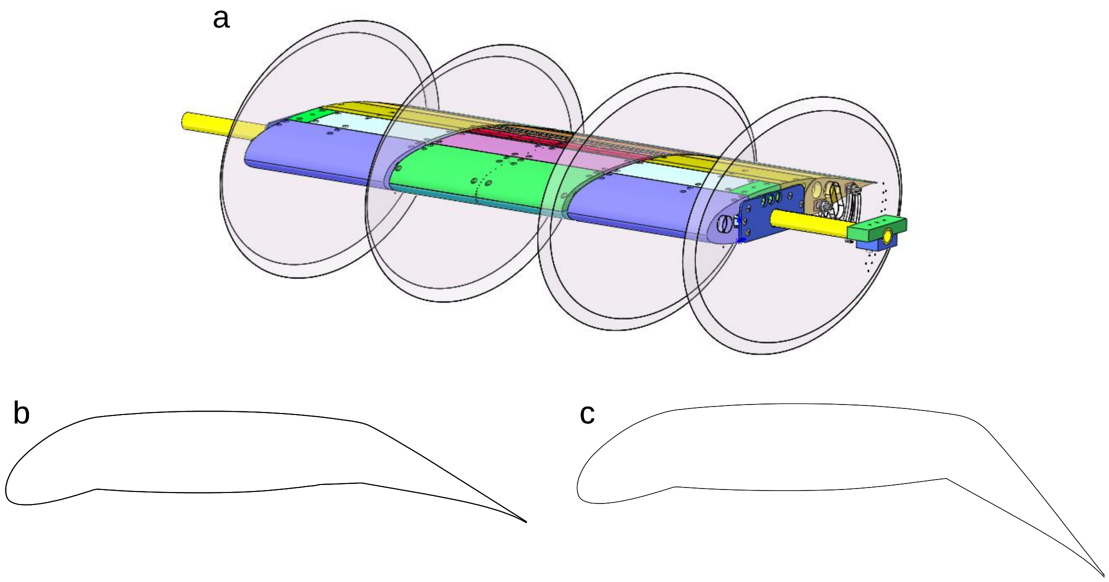

***Figure 7.1.*** *(a) ADVINT-based airfoil model with adjustable trailing edge flap and drooped leading edge. Centerline cross-sections: (b) δ = 20º and (c) δ = 40º.*

## *7.1. High-Lift Aerodynamic Enhancement using Active Flow Control*

The performance of a high-lift system using a simple flap (Figure 7.1) can be improved significantly by increasing the extent of flow attachment along the suction surface of the flap in the absence of a cove flow. This is particularly true at high flap deflection angles where the flow separates at or near the flap shoulder under most conditions. By installing and operating a spanwise array of fluidic oscillators located near the flap shoulder, the extent of flow separation along the flap has been shown to decrease, leading to substantial increases in lift. The oscillating jets are inclined in the streamwise direction through a range of shallow angles relative to the airfoil surface and oscillate in the spanwise direction. The manipulation of spanwise and (in particular) streamwise vorticity concentrations in the boundary layer serves to maintain flow attachment in a domain where the flow would otherwise become separated. This diminishes the blockage caused by the separation over the flap and therefore the flow speeds across the suction

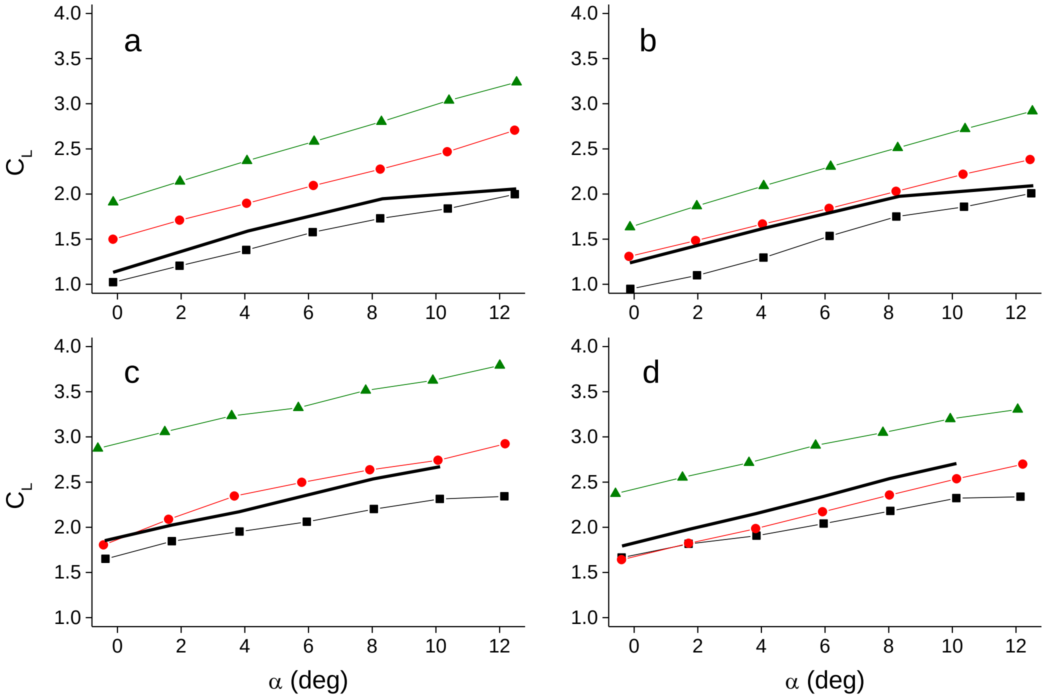

***Figure 7.2.*** *Variation of* $C_l$ *with* $\alpha$*, spanwise fluidic oscillators oriented 26° above the local surface tangent:* $\delta = 20°$, $Re_c = 6.7{\cdot}10^5$ *(a) and* $1.0{\cdot}10^6$ *(b);* $\delta = 40°$, $Re_c = 6.7{\cdot}10^5$ *(c) and* $1.0{\cdot}10^6$ *(d).* $C_\mu = 0$ *(■); 0.3% (*$Re_c = 6.7{\cdot}10^5$*) and 0.13% (*$Re_c = 1.0{\cdot}10^6$*) (●); 1.6% (*$Re_c = 6.7{\cdot}10^5$*) and 0.7% (*$Re_c = 1.0{\cdot}10^6$*) (▲); Baseline (—).*

surface of both the flap and the main element are higher, resulting in increased suction and higher lift. As noted in Chapter 2, aerodynamic quantities shown in this section are 2-D values computed from integration of centerline pressure distributions.

The increase in lift is shown in Figure 7.2, which illustrates the variation of $C_l$ across $0° < \alpha < 12°$ for $Re_c = 6.7{\cdot}10^5$ and $1.0{\cdot}10^6$, and for various values of the momentum coefficient $C_\mu$ (cf. §2.2). Figures 7.2a-b and 7.2c-d present $C_l$ for $\delta = 20°$ and 40°, respectively, for oscillating jets that are inclined in the streamwise direction at 26° above the local surface tangent. Owing to the presence of the downstream-facing actuator orifice, separation occurs slightly farther upstream than on the baseline airfoil that has a gapless outer mold line. In the present implementation, this effect on separation corresponds to a small loss of lift relative to the baseline airfoil of $\Delta C_l = -0.21$ and $-0.22$ for $\delta = 20°$ and 40°, respectively, at $\alpha = 4°$ and $Re_c = 6.7{\cdot}10^5$. Subsequent discussions of

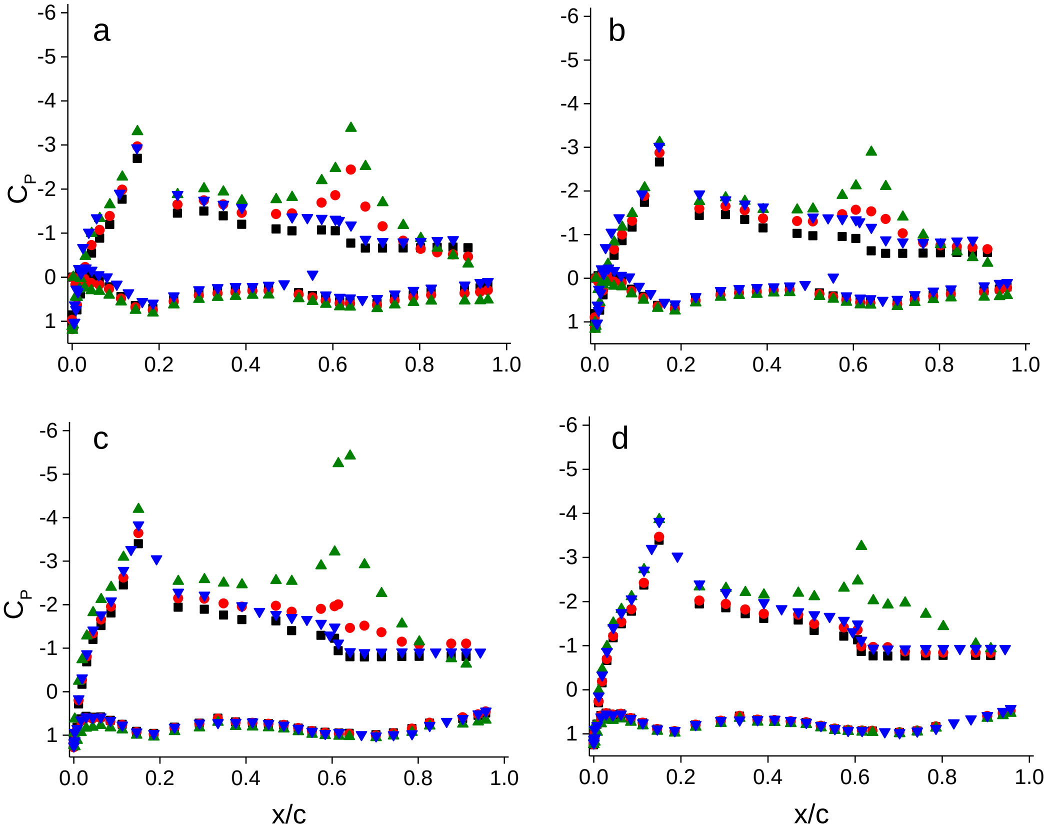

***Figure 7.3**. Variation of $C_p$ with x/c: $\delta$ = 20°, $Re_c$ = $6.7 \cdot 10^5$ (a) and $1.0 \cdot 10^6$ (b); $\delta$ = 40°, $Re_c$ = $6.7 \cdot 10^5$ (c) and $1.0 \cdot 10^6$ (d). (▼) baseline airfoil, other symbols as in Figure 7.2.*

lift increments in this chapter are indicated for these values of $\alpha$ and $Re_c$ and are referenced to the baseline airfoil unless otherwise noted. Refinement of the actuator installation is expected to reduce the lift penalty relative to the smooth baseline. Such efforts in other, similar installations have led to lift decrements as small as $\Delta C_l \sim -0.1$. The data in Figure 7.2 show that actuation leads to a substantial lift increase for $\delta$ = 20°; actuation at $C_\mu = 0.3\%$ has some effectiveness at attaching the flow, resulting in $\Delta C_l = 0.31$, while at $C_\mu = 1.6\%$ the actuation yields a completely attached flow along the flap (as discussed in §7.2) with a much greater lift increment of $\Delta C_l = 0.78$.

The largest lift increment achieved with the fluidic oscillator jets occurs at the flap deflection $\delta$ = 40°, where a large separated flow domain is present over the suction surface in the absence of actuation. In that case, the lift increases by $\Delta C_l = 1.05$ with actuation at $C_\mu = 1.6\%$ yielding $C_l = 3.23$ at $\alpha = 4^o$. This corresponds to nearly complete flow attachment along a steeply inclined, downstream-facing flap suction surface (as discussed in §7.2). It is also noteworthy that for a deflection of $\delta = 20^o$ at $Re_c=1.0 \cdot 10^6$, $C_\mu = 0.13\%$ is sufficient to recover the lift losses due to the presence of the actuator (Figure 7.2b, for $Re_c = 1.0 \cdot 10^6$) while higher actuation level ($C_\mu = 0.3\%$) is required at $\delta = 40^o$ (Figure 7.2c). The same trend was observed for $Re_c = 6.7 \cdot 10^5$.

As discussed in connection with Figure 7.2, the lift increase is associated with increased suction along the suction surface of the airfoil. This is shown in the pressure distributions on the model at $\alpha = 4^o$ for $\delta = 20^o$ and $\delta = 40^o$ (Figure 7.3). All pressure distributions exhibit a suction peak at $x/c = 0.15$, which does not migrate significantly with $\alpha$ or $C_\mu$ since the surrounding flow is influenced primarily by the drooped leading edge. On the baseline airfoil, separation occurs at $x/c = 0.70$ for $\delta = 20^o$, i.e. immediately downstream of the flap shoulder, and migrates upstream to $x/c = 0.65$ for $\delta = 40^o$ because of the steeply inclined flap suction surface that causes a strong adverse pressure gradient. The separated flow results in blockage on the suction surface, reducing the circulation around the airfoil and consequently the lift. In the presence of the fluidic oscillator without forcing ($C_\mu = 0$) this effect is exaggerated somewhat because separation occurs at the orifice, which is located ~$0.05c$ upstream of the baseline separation point. For $\delta = 20^o$, a very low level of forcing ($C_\mu = 0.13\%$) is sufficient to overcome the additional suction losses due to the presence of the actuator. Actuation causes a low pressure domain to form in the vicinity of the orifice, apparent near $x/c = 0.65$ in the pressure distributions. In turn, the separation point moves downstream and there is increased suction across the suction surface of the main element as far upstream as $x/c = 0.10$.

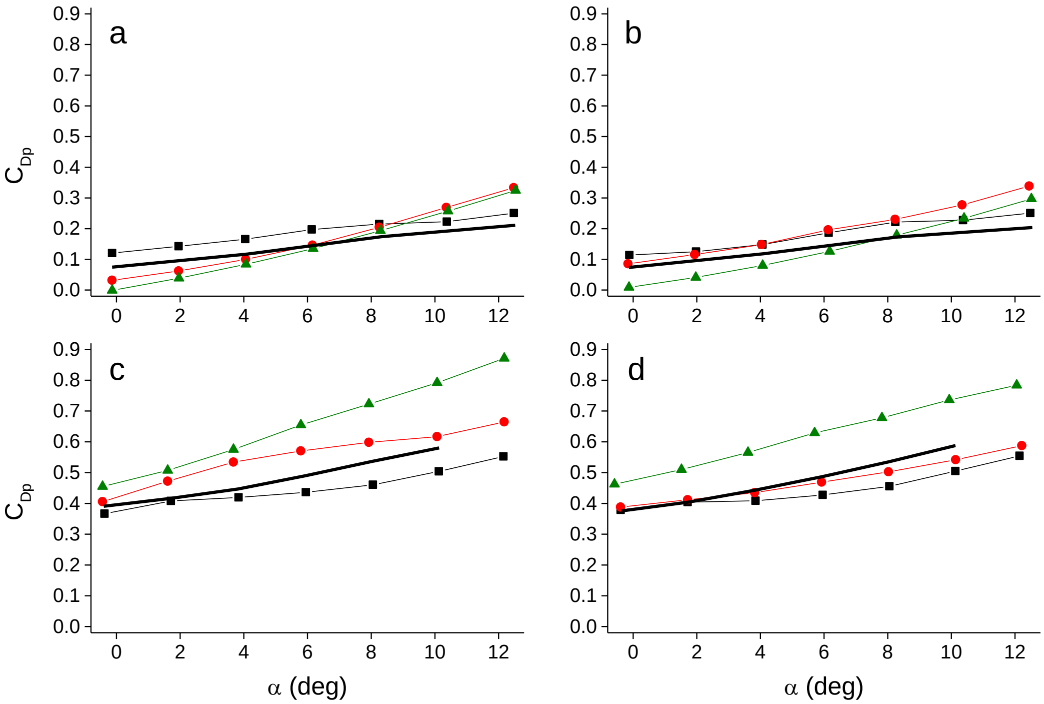

***Figure 7.4**. Variation of $C_{dp}$ with α:  δ = 20º, $Re_c$ = 6.7·$10^5$ (a) and 1.0·$10^6$ (b); δ = 40º, $Re_c$ = 6.7·$10^5$ (c) and 1.0·$10^6$ (d).  Symbols as in Figure 7.2.*

Actuation at progressively higher levels of $C_\mu$ leads to vorticity concentrations near the flap shoulder, causing a Coanda-like effect in which the flow turns downward and follows the flap suction surface.  This leads to additional suction over the main element and hence increased lift.  The flow over the flap is attached across nearly the entire length of the flap at $C_\mu = 0.3\%$ (see §7.2) and remains fully attached at higher $C_\mu$ as well.  Low-level forcing ($C_\mu = 0.13\%$) is less effective with the δ = 40º flap, producing little additional suction on the surface because the flow over the flap is strongly separated. However, at higher momentum coefficients, a significant degree of flow attachment begins to develop.  At $C_\mu = 0.7\%$ the separation point moves to approximately 0.70*c* with substantial additional suction over the main element.  The effect of forcing is greatest at $C_\mu = 1.6\%$, *where the flow becomes fully attached on the suction surface of the δ = 40º flap*.  At that $C_\mu$, the suction peak at the flap shoulder becomes stronger than the leading edge suction peak (with a minimum of $C_p = -5.4$) and there is substantial additional

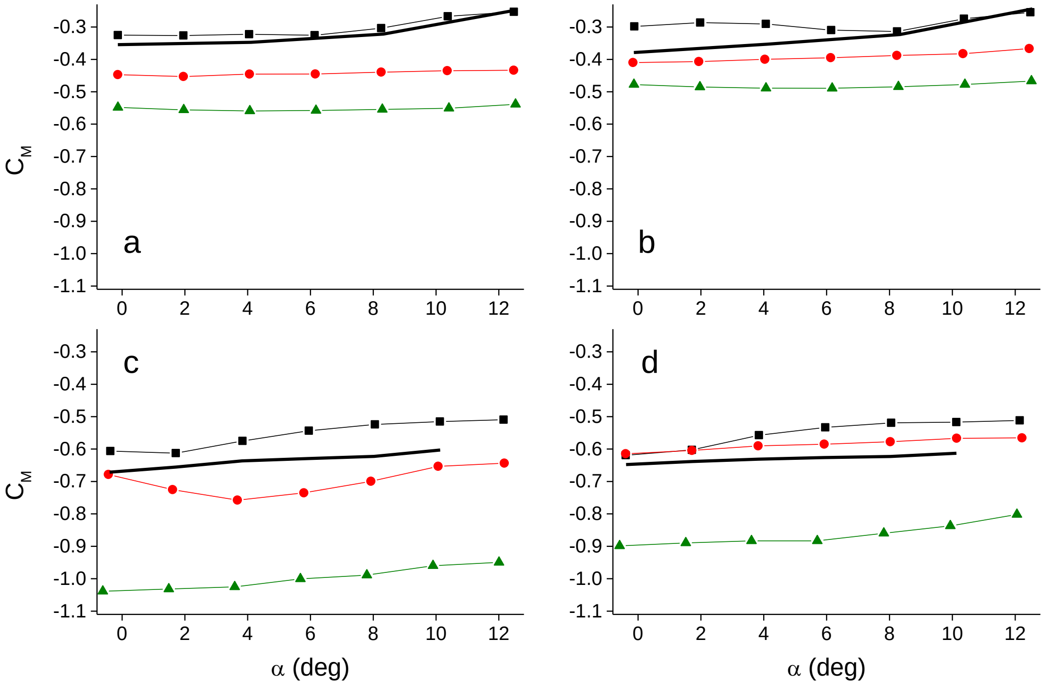

***Figure 7.5***. *Variation of $C_m$ with α: δ = 20º, $Re_c$ = 6.7·$10^5$ (a) and 1.0·$10^6$ (b); δ = 40º, $Re_c$ = 6.7·$10^5$ (c) and 1.0·$10^6$ (d). Symbols as in Figure 7.2.*

suction across the surfaces of the main element and the drooped leading edge. There is also a slight increase in pressure on the pressure surface of the drooped leading edge, suggesting a migration of the leading edge stagnation point toward the pressure surface.

The variation in pressure drag $C_{dp}$ corresponding to Figure 7.2 is shown in Figure 7.4. With the $\delta$ = 20º flap, the pressure drag increases slightly in the presence of the fluidic oscillator because the separation point moves upstream. Actuation improves flow attachment, decreases the extent of separation and reduces pressure drag at low angles of attack (the difference is greatest at $\alpha$ = 0º, where $C_{dp}$ decreases from 0.12 at $C_\mu = 0$ to nearly zero at $C_\mu = 1.6\%$). As $\alpha$ increases, additional lift-induced drag is generated resulting in increased $C_{dp}$. At $\delta$ = 40º, lift-induced drag dominates due to the higher $C_l$ levels at that flap deflection. Hence, variation in $C_{dp}$ coincides approximately with variation in $C_l$ (cf. Figure 7.2c-d), with $l/d_p \sim$ 5-6.

Figure 7.5, corresponding to the lift and drag data presented in Figure 7.2, shows the variation of $C_\mathrm{m}$ with $\alpha$. Pitching moment is strongly nose-down due to the deflected flap and exhibits comparable values between the unactuated and smooth conditions ($C_\mathrm{m} \approx -0.30$ and $-0.60$ for $\delta = 20^\circ$ and $40^\circ$, respectively) as well as minimal variation due to $\alpha$. Under actuation, the suction generated near the flap shoulder (located at $x/c = 0.65$) on the suction surface of the main element and the flap creates an additional nose-down pitching moment. The magnitude of pitching moment is as large as $C_\mathrm{m} \approx -1.0$ for $C_\mu = 1.6\%$ at $\delta = 40^\circ$.

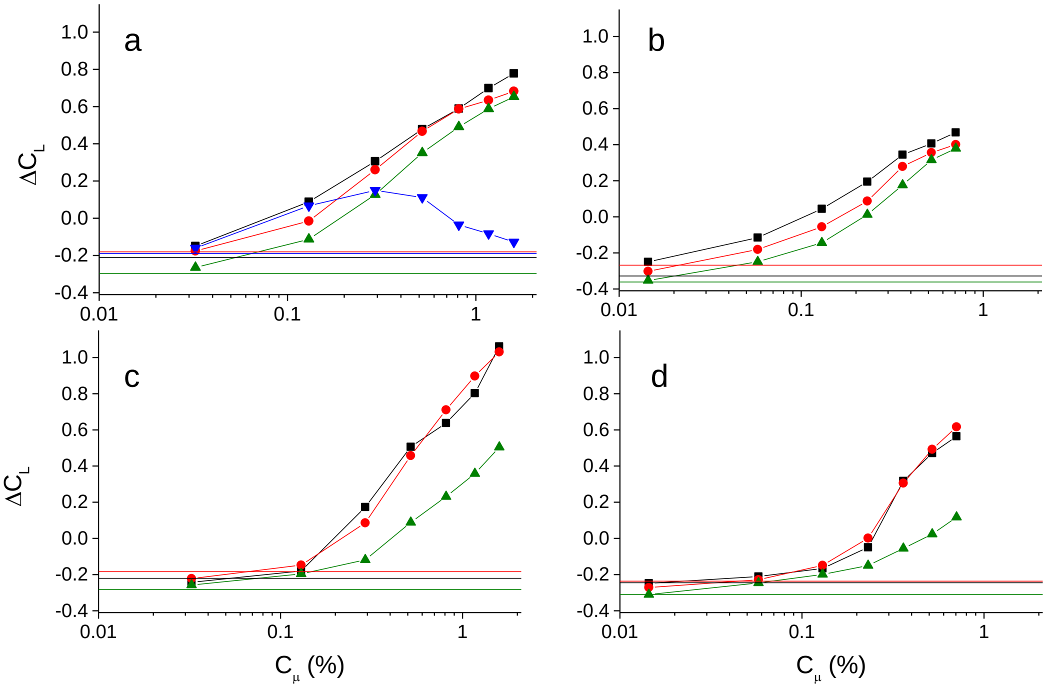

***Figure 7.6.*** *Variation of $\Delta C_l$ with $C_\mu$: $\delta = 20^\circ$, $Re_c = 6.7 \cdot 10^5$ (a) and $1.0 \cdot 10^6$ (b); $\delta = 40^\circ$, $Re_c = 6.7 \cdot 10^5$ (c) and $1.0 \cdot 10^6$ (d). Spanwise fluidic oscillators oriented above tangential 26° (■),37° (●),45° (▲). Horizontal lines denote results for $C_\mu = 0$. Configuration with 14 fluidic oscillators oriented normal to the airfoil surface (▼) in (a).*

In addition to the fluidic oscillator configuration used to obtain the measurements in Figures 7.2-5, with oscillating jets inclined 26° above the local surface tangent, alternate configurations are characterized with jet inclination angles of 37° and 45° above the local surface tangent (larger angles were found to be ineffective). The variation of $\Delta C_l$ with $C_\mu$ (relative to the baseline airfoil) at $\alpha = 4^o$ is shown in Figure 7.6 for the three different configurations. In Figure 7.6a, $\Delta C_l$ is shown for a configuration with 14 evenly spaced oscillating jets that are normal to and flush with the surface, indicating that for low levels of forcing ($C_\mu < 0.2\%$) the performance is comparable to the jets angled at 26º. This indicates that there are differences in the flow attachment mechanisms for surface-normal jets and that it may be practical to apply such a configuration, perhaps using multiple chordwise actuation points, in full-scale systems with limited maximum $C_\mu$. It is noteworthy that because of the limit on measurable flow rate in the actuation system of the present setup, $C_\mu$ is limited to 1.6% and 0.7% at $Re_c = 6.7{\cdot}10^5$ and $1.0{\cdot}10^6$, respectively. The maximum $C_\mu$ is lower at the higher Reynolds number due to the higher free stream speed $U_\infty$ at that condition. With a jet angle of 26º and the $\delta = 20^o$ flap, lift is reduced by $\Delta C_l = -0.21$ in the absence of actuation (relative to the smooth baseline) but increases with $C_\mu$ to a maximum of $\Delta C_l = 0.78$ at $C_\mu = 1.6\%$. The effect is strongest with the jets oriented at the lowest angle and diminishes with increasing jet angle. Likewise, at $\delta = 40^o$ there is a lift reduction of $\Delta C_l = -0.22$ without actuation, and $\Delta C_l$ increases with $C_\mu$ to a maximum of $\Delta C_l = 1.05$ at $C_\mu = 1.6\%$. In this configuration jet angles of 26º and 37º give comparable performance, while a significant loss of effectiveness occurs at an angle of 45º.

### *7.2. Effect of Active Flow Control on Flow Separation*

In order to characterize the effects of the actuator on the flow field around the airfoil, a series of PIV measurements have been obtained over the suction surface. The measurement plane is normal to the spanwise axis of the airfoil and is located 10 mm

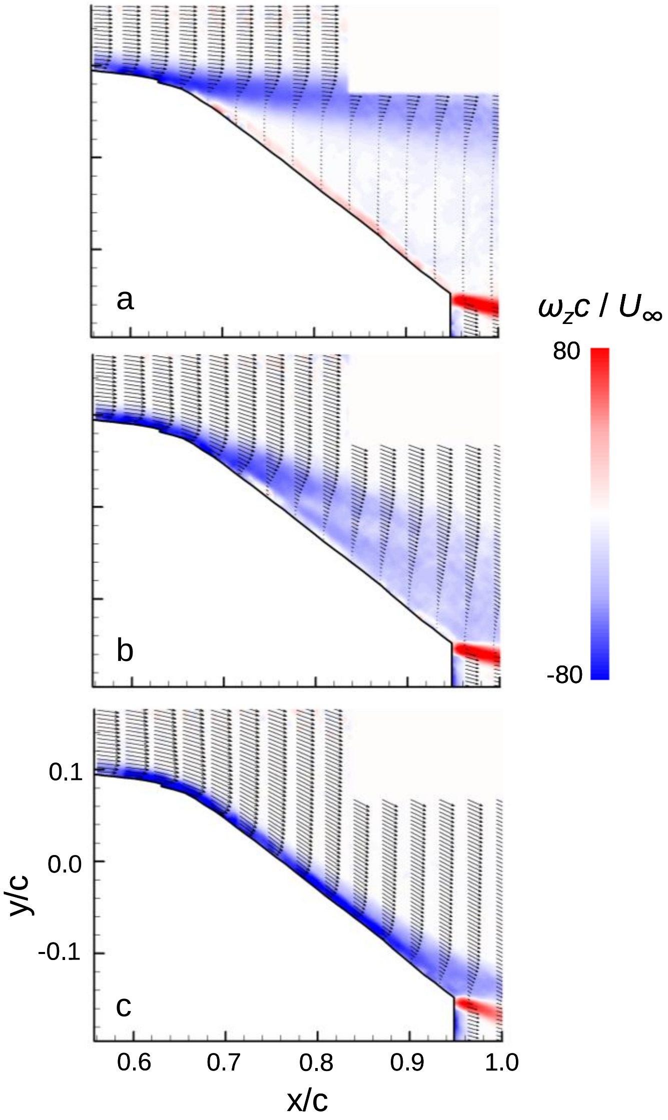

***Figure 7.7***. *Flowfield on $\delta = 20^o$ flap; spanwise oscillators 26º above the local surface tangent.* *$C_\mu$ = 0 (a), 0.3% (b), 1.6% (c).*

from the centerline, coincident with one of the 42 jet orifices across the span of the active section of the airfoil. Flow maps spanning the entire flap suction surface downstream of the shoulder which include the actuator orifice were formed by combining two overlapping views, each measuring 126 mm on a side, corresponding to 126 μm/pixel ($\delta$ = 20º and 40º in Figures 7.7 and 7.8, respectively). The far right edge of the masked region (below the surface) is the trailing edge of the model and corresponds to the edge of the PIV laser sheet (projected from above). A second set of higher resolution flow maps

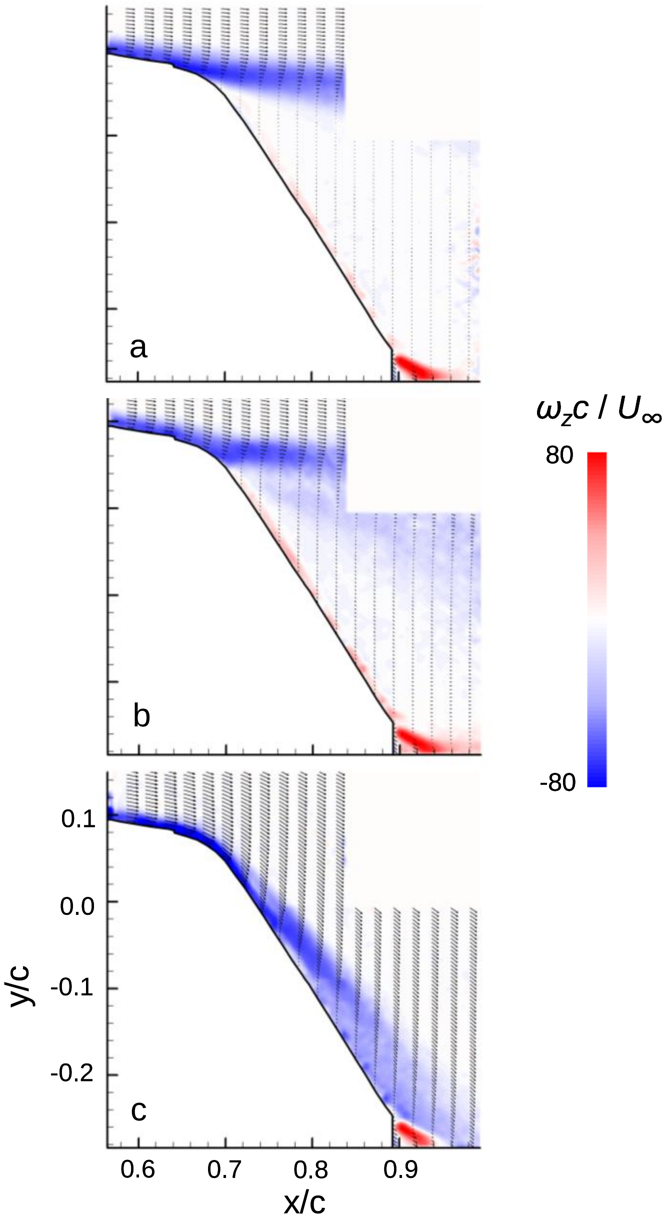

***Figure 7.8***. *Flowfield on $\delta$ = 40º flap; spanwise oscillators 26º above the local surface tangent. $C_\mu$ = 0 (a), 0.3% (b), 1.6% (c).*

were measured in the vicinity of the actuator orifice, each consisting of a single square view measuring 22 mm on a side (22 μm/pixel). These measurements were taken at $Re_c = 6.7 \cdot 10^5$ and $\alpha = 4°$ with fluidic oscillator jets oriented 26º above the tangential direction. Each velocity vector map is a time-average of 450 individual realizations.

For a $\delta$ = 20° flap, in the absence of actuation (Figure 7.7a) the flow separates at ~0.07*c* downstream of the actuator orifice, creating a recirculation zone over most of the flap suction surface as indicated by the opposite sense vorticity near the surface. Operation of the fluidic oscillator jets at $C_\mu$ = 0.3% and 1.6% (Figures 7.7b-c) results in the introduction of concentrations of streamwise vorticity and the resulting movement of high-momentum fluid toward the surface leads to flow attachment. The collapse of the separated flow domain at $C_\mu$ = 0.3% (Figure 7.7b) is spread over a relatively thick shear layer that is attached to the wall. With actuation at $C_\mu$ = 1.6% (Figure 7.7c) the attached vorticity layer is considerably thinner and has the appearance of an attached boundary layer where the vorticity is primarily concentrated near the wall along nearly the entire flap as far downstream as the trailing edge. It is noteworthy that the interaction domain between the suction surface boundary layer and the trailing edge extends as far as 0.08*c* upstream of the trailing edge, where the boundary layer begins to thicken significantly.

The corresponding velocity and vorticity maps for $\delta$ = 40° are shown in Figure 7.8. In the absence of actuation (Figure 7.8a), the flow separates near a location 0.05*c* downstream of the actuator, forming a (nearly) free shear layer that bounds the wake from above. Low-level actuation ($C_\mu$ = 0.3%; Figure 7.8b) concentrates the boundary layer near the surface, causing the separation point to move to ~0.06*c* downstream of the actuator. The separated shear layer appears to thicken and is tilted toward the surface indicating higher streamwise velocity adjacent to the surface which is also evident from the higher intensity opposite sense vorticity layer near the wall. At $C_\mu$ = 1.6% (Figure 7.8c) the flow remains attached along nearly the entire flap resulting in a significant increase in lift. Due to the strong adverse pressure gradient (cf. Figure 7.3c) the

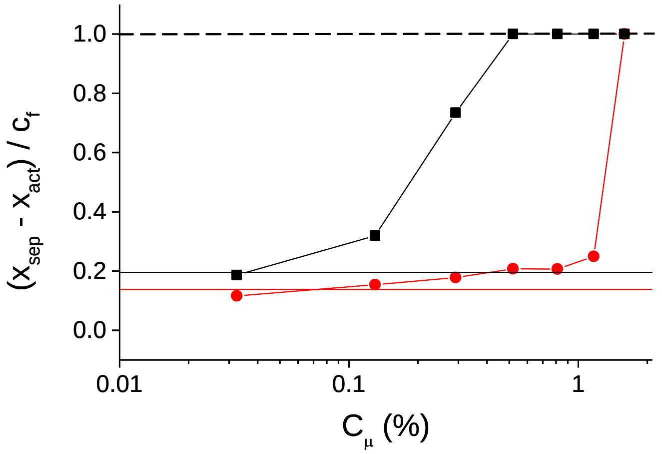

***Figure 7.9***. *Distance of separation point from actuator, scaled by flap chord $c_f = 0.35c$. (■) $\delta = 20^\circ$ (flow fully attached for $C_\mu > 0.3\%$), (●) $\delta = 40^\circ$ (flow fully attached for $C_\mu > 1.2\%$). Horizontal lines denote results for $C_\mu = 0$.*

boundary layer thickens considerably along the flap. It should be noted that significant gains in $C_L$ can be realized even in the absence of fully attached flow (cf. Figure 7.6).

The variation of separation location with $C_\mu$ for the $\delta = 20^\circ$ and 40° flaps is shown in Figure 7.9 in terms of distance downstream from the actuator scaled by the flap chord $c_f$. For the $\delta = 20^\circ$ flap, separation occurs at $0.2c_f$ downstream of the actuator in the absence of actuation. Due to the relatively small turning angle around the shoulder, actuation at $C_\mu = 0.13\%$ is sufficient to move the separation point to $0.32c_f$. At $C_\mu = 0.3\%$, the flow is attached along the entire suction surface of the flap (Figure 7.7b) and remains attached (with thinner boundary layer) at higher $C_\mu$ (Figure 7.7c). Separation on the $\delta = 40^\circ$ flap in the absence of actuation occurs farther upstream than on the $\delta = 20^\circ$ flap at a location $0.14c_f$ downstream of the actuator. Increasing $C_\mu$ moves the separation point downstream in small increments, since the steeply inclined surface immediately downstream of the shoulder creates a strong adverse pressure gradient (cf. Figure 7.3c-d). Only by operating at $C_\mu = 1.6\%$ does the flow become fully attached. It

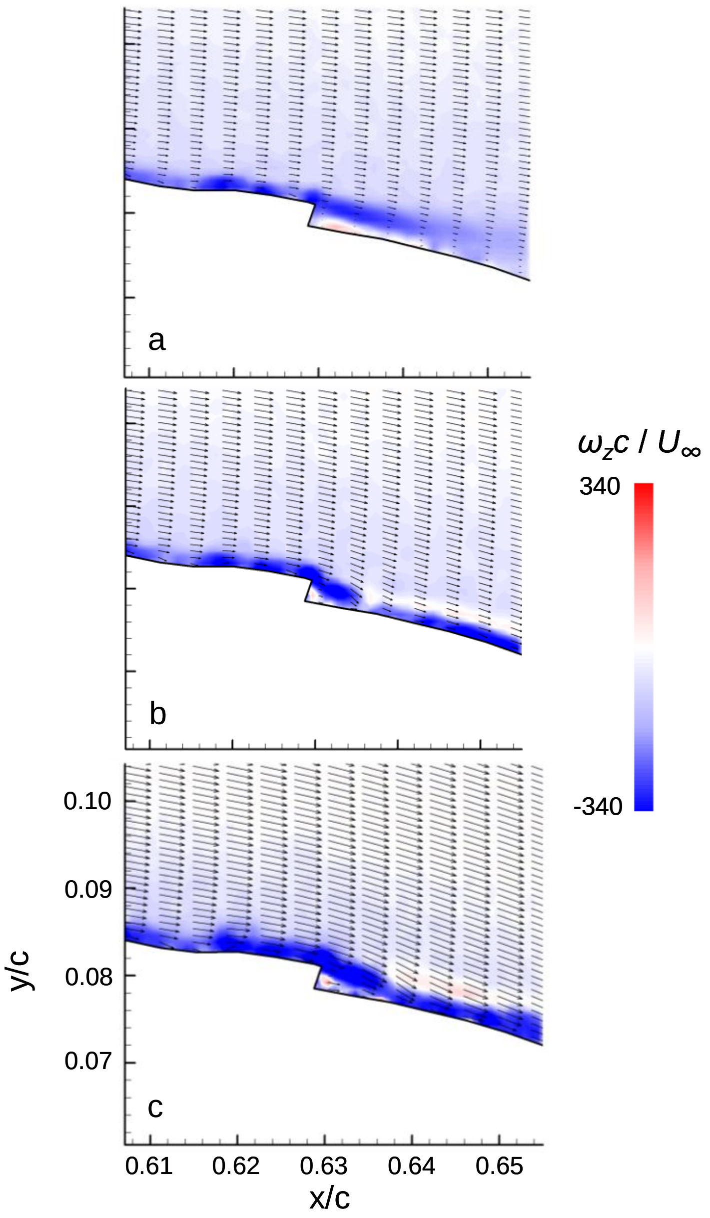

***Figure 7.10**. Magnified views of flowfield near juncture of mainbody and $\delta$ = 40º flap; spanwise oscillators 26º above the local surface tangent indicated by step in airfoil surface. $C_\mu$ = 0 (a), 0.3% (b), 1.6% (c).*

is remarkable that the change in the attachment distance increases rapidly with $C_\mu$ past 1.2%.

Magnified views of the flap shoulder and orifice for $\delta = 40^\circ$, spanning a chordwise distance of 0.05*c*, are shown in Figure 7.10a-c with $C_\mu$ = 0, 0.3% and 1.6%, respectively. In the absence of actuation (Figure 7.10a), there is a small recirculation domain near the surface downstream of the orifice. The streamwise extent of this recirculating domain diminishes significantly with actuation at $C_\mu = 0.3\%$ (Figure 7.10b). The local attachment of the flow to the surface is accompanied by a local increase in the streamwise velocity within the boundary layer. These effects of the actuation are further enhanced at $C_\mu = 1.6\%$ (Figure 7.10c) which indicates significantly higher momentum within the boundary layer. It is also noteworthy that the speed of the outer flow increases significantly with $C_\mu$ due to the strong low pressure domain that forms near the actuator. An important feature of the attached flow is the absence of a "time-averaged" classical wall jet downstream of the orifice. While this may be attributed in part to the spanwise oscillation of the actuation jet, it appears that this absence may be the result of cross stream mixing and the strong acceleration of the outer flow owing to the attachment.

Figure 7.11 shows scaled cross-stream distributions of streamwise velocity and spanwise vorticity $0.014c$ downstream of the actuator for $\delta = 40^\circ$ and $0 \leq C_\mu \leq 1.6\%$. These distributions are obtained from the high magnification PIV data (a subset of which is shown in Figure 7.10). The velocity measurements are scaled by the free stream speed $U_\infty$, cross-stream elevation is scaled by the 99%-velocity boundary layer thickness $\delta_{0.99}$ in the absence of actuation, and vorticity is scaled by $\omega_{\mathrm{ref}}$, the maximum vorticity magnitude for $C_\mu = 0$. As $C_\mu$ increases, the streamwise velocity (Figure 7.11a) increases substantially, with the largest increase near the wall. For $C_\mu \geq 0.13\%$ there is a local maximum near the wall that may be indicative of the penetration of high-speed fluid from the outer flow. This domain is associated with a local diminution in the spanwise vorticity near the surface at $y/\delta_{0.99} \sim 0.1$ (Figure 7.11b).

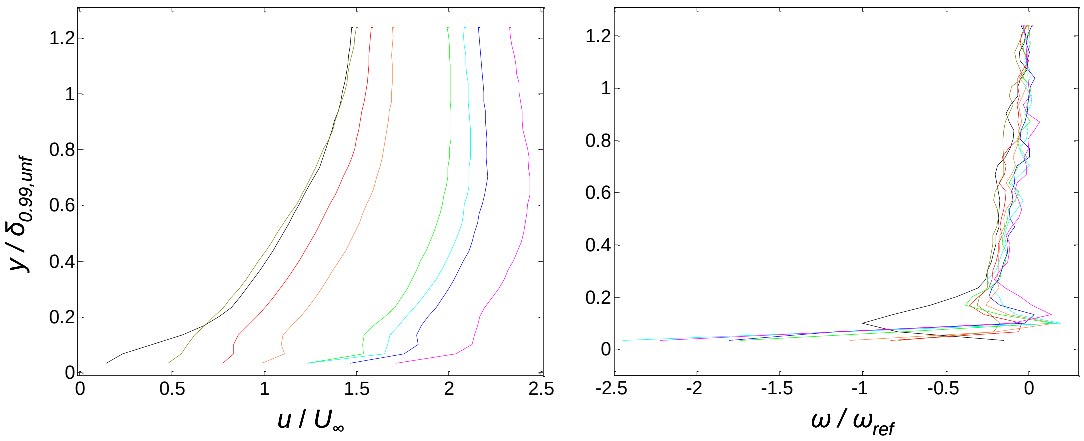

***Figure 7.11.*** *Velocity and vorticity profiles from Figure 13, in order of increasing $C_\mu$:* ***0****,* ***0.03%****,* ***0.13%****,* ***0.3%****,* ***(0.5%)****,* ***(0.8%)****,* ***1.2%****, 1.6%.*

Chapter 8 focuses on an investigation of the enhancement of high-lift performance using synthetic jet actuation. Because fluidic oscillators require a supply of high-pressure air to operate, it is desirable to eliminate this requirement by using zero-net-mass-flux actuation to introduce momentum into the surrounding flow. It is subsequently shown how synthetic jets can achieve comparable high-lift performance improvement provided the actuation authority is sufficient.

# CHAPTER 8

# SEPARATION CONTROL ON A SIMPLE FLAP USING SYNTHETIC JETS

As noted in Chapter 7, active flow control based on fluidic oscillators requires externally-supplied mass flux with adequate momentum, and therefore it is desirable to implement active flow control using zero-net-mass-flux actuation. This chapter shows how a spanwise array of synthetic jet actuators (that require no external fluid supply) can be used to reduce the extent of separation. A detailed study (based on three-dimensional PIV measurements) of the mechanism through which jet actuation leads to improved flow attachment (and hence greater lift) is also undertaken.

## *8.1. Aerodynamic Effects of Synthetic Jet-Based Active Flow Control*

The effects of actuation momentum coefficient $C_\mu$ on the attainable lift increment $\Delta C_l$ (the increase in lift computed from pressure distributions relative to the unactuated airfoil) are investigated over the range $0 < C_\mu < 2\%$ (at $\alpha = 4^\circ$). The spanwise actuation period $\lambda(n; k)$ is defined as $\lambda = n \cdot \lambda_j$ where $\lambda_j$ is the center to center distance between adjacent jet orifices (5.4 mm or $0.012c$ in the present implementation) and $k$ is the number of adjacent active jets within $n$. The actuation momentum coefficient $C_\mu$ is computed using the area of the jets that are operational across the span and the area of the airfoil. It should be noted that for a given total $C_\mu$, the momentum per jet varies with $\lambda$. Since the operating range of the present actuators has an upper bound that is dictated by the specific characteristics of the piezoelectric drivers, the global $C_\mu$ is also adjusted by varying $Re_c$ ($3.3 \cdot 10^5 < Re_c < 1.0 \cdot 10^6$) and the spatial duty cycle of the spanwise-periodic

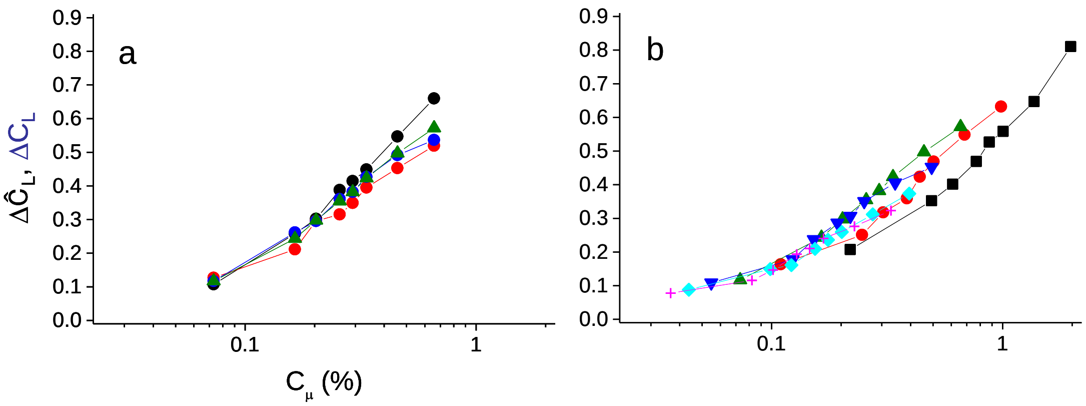

***Figure 8.1.*** *(a) Variation of* $\Delta\hat{C}_l$ *with* $C_\mu$ *at spanwise positions* $z_0$(●), $z_1$(●), $z_2$(●) *and period average* $\Delta C_l$ (▲). $\alpha = 4°$, $\lambda(3; 1) = 0.035c$. *(b) Variation with* $C_\mu$ *of* $\Delta C_l$ ($\alpha = 4°$). $\lambda(n; 1)$ = (■) *0.012c (n = 1),* (●) *0.023c (n = 2),* (▲) *0.035c (n = 3),* (▼) *0.047c (n = 4),* (♦) *0.058c (n = 5),* (+) *0.070c (n = 6).*

actuation *k/n*. The $\lambda$-averaged lift increment $\Delta C_l$ is computed from pressure measurements across *n* spanwise stations spaced $\lambda_j$ apart within $\lambda$ (cf. Figure 2.6).

Shown in Figure 8.1a is the spanwise variation in sectional lift $\Delta\hat{C}_l$ between measurement stations $z_0$, $z_1$ and $z_2$ within the spanwise wavelength $\lambda(3; 1) = 0.035c$ along with the resulting $\lambda$-averaged $\Delta C_l$. The highest $\Delta\hat{C}_l$ is measured at station $z_0$ (closest to the jet orifice), and the differences between $\Delta\hat{C}_l(z_i)$ increase with $C_\mu$. The (marginally) lower lift increments at $z_1$ and $z_2$ suggests that the actuation wavelength can be optimized to minimize the required actuation power for a desired $\Delta C_l$.

Figure 8.1b shows the variation of lift increment $\Delta C_l$ with a single active jet within a spanwise actuation period (i.e. $k = 1$) such that $\lambda(n = 1\text{-}6; 1) / c = 0.012$, 0.023, 0.035, 0.047, 0.058 and 0.070. A maximum lift increment of $\Delta C_l = 0.82$ is achieved at $C_\mu = 2\%$ when all jets are active [i.e., $\lambda(1; 1) = 0.012c$]. As $\lambda$ increases, the available $C_\mu$ decreases, and, consequently, the maximum attainable $\Delta C_l$ diminishes. However, it is noteworthy that for a given $C_\mu$, $\Delta C_l$ can be maximized by adjusting the actuation

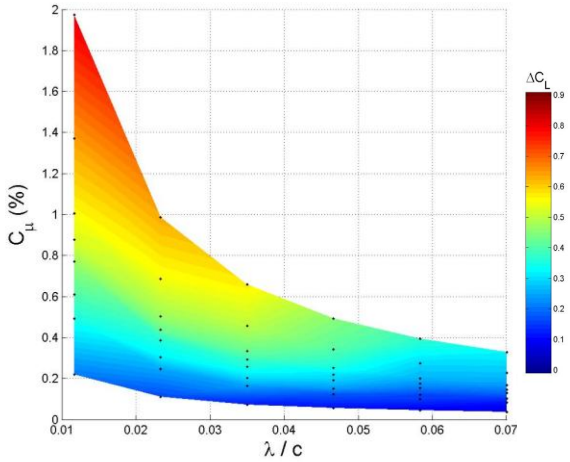

***Figure 8.2.*** *Variation of $\Delta C_l$ with $C_\mu$ and $\lambda / c$ ($k = 1$, $\alpha = 4°$). Points indicate measurements.*

wavelength $\lambda$. For example, at $C_\mu = 0.4\%$ the maximum lift increment is $\Delta C_l = 0.46$ for $\lambda(3; 1) = 0.035c$ indicating that better global performance at lower global $C_\mu$ may be attained using a small number of higher power individual jet actuators. For $C_\mu < 0.15\%$, lift increments on the order of $\Delta C_l \sim 0.1\text{-}0.2$ are realized, indicating that some performance improvement is possible even for severely limited $C_\mu$. In addition, at these low actuation levels, $\Delta C_l$ becomes invariant with $\lambda$ and hence the spanwise distribution of actuation becomes less significant (cf., Figure 8.1b).

By varying $C_\mu$ and $\lambda$ independently, the optimal wavelength (for which minimum $C_\mu$ is required to produce a given $\Delta C_l$) can be determined. Figure 8.2 is a color raster plot of $\Delta C_l[\lambda(n, 1)\ C_\mu]$. These data show that within the range of the present measurements, a given $\Delta C_l$ can be attained at a local minimum of $C_\mu$. To achieve lift increments of $\Delta C_l > 0.3$, the required $C_\mu$ is minimized for spanwise wavelengths of $\lambda \sim 0.035c$–$0.04c$, while at lower $\Delta C_l$ the required $C_\mu$ does not vary significantly with $\lambda$ (cf. Figure 4).

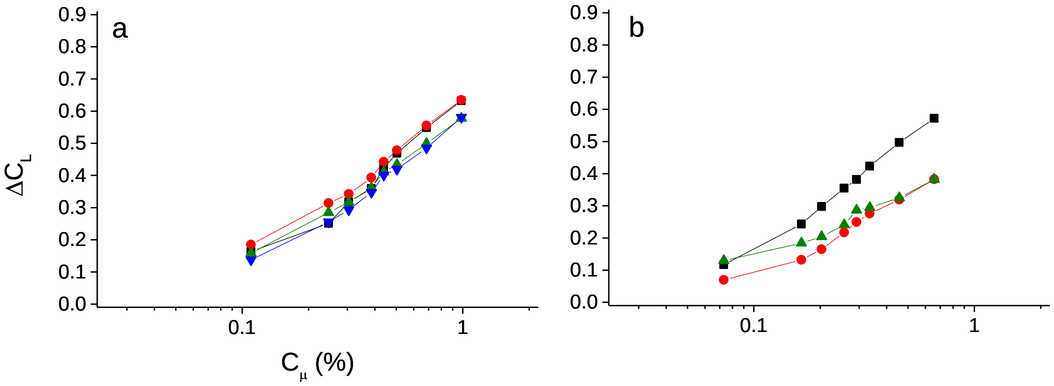

***Figure 8.3.*** *Variation of* $\Delta C_l$ *with* $C_\mu$ *(α = 4°) for (a) k / n = 0.5:* $\lambda$ *= (■) 0.023c, (●) 0.047c, (▲) 0.070c, (▼) 0.093c and (b) k / n = 0.33:* $\lambda$ *= (■) 0.035c, (●) 0.070c, (▲) 0.105c.*

The effects of varying $\lambda$ for a constant spatial duty cycle ($k / n$) are shown in Figure 8.3. For $k / n = 0.5$ (Figure 8.3a) the global $C_\mu$ is relatively invariant with actuation wavelength. The maximum lift increments for a given $C_\mu$ are nearly identical for $\lambda(2; 1) = 0.023c$ and $\lambda(4; 2) = 0.047c$ where the distances between active jet groups are comparable to the optimum. For $\lambda(6; 3) = 0.070c$ and $\lambda(8; 4) = 0.093c$, where the separation distances are suboptimal, the reduction in $\Delta C_l$ is relatively small. However, as the duty cycle is reduced to $k / n = 0.33$ (Figure 8.3b), the reduction in performance at suboptimal spacings is considerably more pronounced. In this configuration, the largest $\Delta C_l$ is obtained for $\lambda(3; 1) = 0.035c$ at which the jet separation distances are nearly optimal (cf. Figure 8.2). Increasing the spanwise period to $\lambda(6; 2) = 0.070$ and $\lambda(9; 3) = 0.105$, $\Delta C_l$ is significantly diminished (in contrast to $k/n = 0.5$), indicating that the interaction of the jets with the cross flow becomes less effective as the spacing between adjacent groups of active jets becomes large. This suggests that widely spaced groups of active jets are less effective at forming streamwise vorticity concentrations (and the induced pressure gradients) as discussed in §8.2.

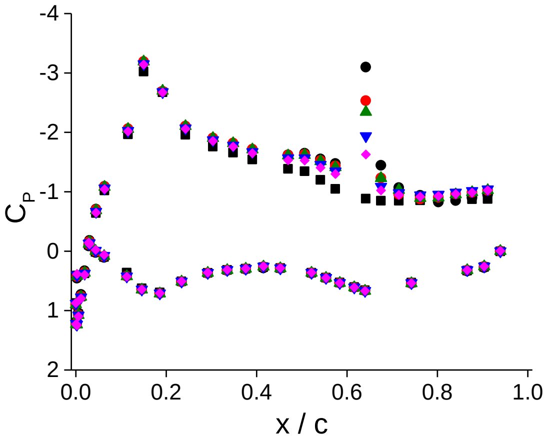

***Figure 8.4.*** *Spanwise-averaged pressure distributions ($\alpha$ = 4°, $Re_c = 5.0 \cdot 10^5$).* (■) *Unactuated,* (●) *$\lambda(1; 1) = 0.012c$,* (●) *$\lambda(2; 1) = 0.023c$,* (▲) *$\lambda(3; 1) = 0.035c$,* (▼) *$\lambda(4; 1) = 0.047c$,* (♦) *$\lambda(6; 1) = 0.070c$.*

The lift increment in Figures 8.1-4 is associated with increased suction along the suction surface of the airfoil, as shown in the spanwise-averaged pressure distributions at $\alpha$ = 4° for $Re_c = 5.0 \cdot 10^5$ (Figure 8.4). Results are shown in the absence of actuation and for actuation configurations $\lambda(1; 1) = 0.012c$, $\lambda(2; 1) = 0.023c$, $\lambda(3; 1) = 0.035c$, $\lambda(4; 1) = 0.047c$ and $\lambda(6; 1) = 0.070c$, with $C_\mu$ = 0.88%, 0.44%, 0.29%, 0.22% and 0.15%, respectively. The suction peak at $x/c$ = 0.15 is primarily an effect of the drooped leading edge and is not influenced by actuation. On the unactuated airfoil, separation occurs at $x/c$ = 0.63, i.e. at the actuator orifice, due to the steeply inclined flap suction surface farther downstream. Because the flow separates instead of turning downward (along the flap surface) there is a substantial loss of lift. By using actuation to mitigate separation near the flap juncture, the flow can be turned toward the flap surface to a greater extent, resulting in increased lift. This effect is manifested in the pressure distribution with the formation of a low pressure domain near the orifice, apparent near $x/c$ = 0.65. In turn, separation moves downstream and suction increases across the suction surface of the main element as far upstream as $x/c$ = 0.10 due to the increased upstream flow speeds that result from reducing blockage. As $\lambda$ decreases the number of active jets is increased. As a result, the suction between the jet and a location 0.05*c* downstream (relative to the unactuated condition) increases, particularly at the suction peak, along with the strength and streamwise extent of the associated adverse pressure gradient. These effects indicate that the improvement in flow attachment and mitigation of separation are dependent on $C_\mu$. Upstream of the orifice there is a small increase in suction relative to the unactuated airfoil which develops even for $\lambda(6; 1) = 0.070c$ ($C_\mu = 0.15\%$; $\Delta C_l = 0.21$) and increases marginally as $\lambda$ is decreased (with $C_\mu$ up to 0.88%), suggesting that the small lift increment at low $C_\mu$ that is invariant with $\lambda$ (cf. Figure 8.1b) may be associated with the upstream suction.

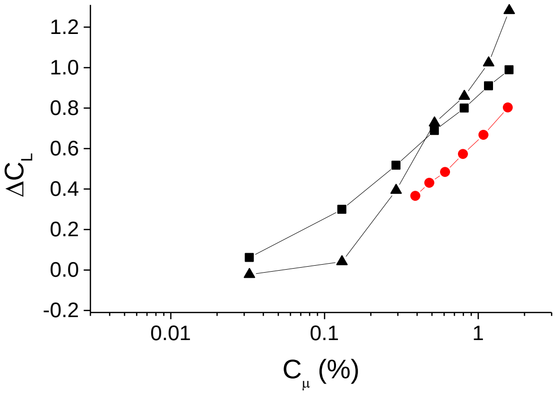

***Figure 8.5.*** *Comparison of $\Delta C_l$ for fluidic oscillators ($Re_c = 6.7\cdot10^5$): $\delta = 20°$ (■) and 40° (▲) and synthetic jets ($3.3\cdot10^5 < Re_c < 1.0\cdot10^6$, $\lambda(1; 1) = 0.012c$): $\delta = 25°$ (●).*

Figure 8.5 contains a comparison between the effects of the synthetic jet array and the array of fluidic oscillators used in the results in Chapter 7. The same ADVINT airfoil configuration is used for both sets of measurements, and in both instances the actuator jets issue tangentially from the surface near the flap-to-main body juncture and have similar spanwise density. The fluidic oscillator measurements are made at $\alpha = 4^\circ$ and

$Re_c = 6.7\cdot10^5$ (adjusting $C_\mu$ by varying the actuator flow rate at fixed $Re_c$) for $\delta = 20^\circ$ and $40^\circ$, and the synthetic jet array is tested at $\alpha = 4^\circ$, $\delta = 25^\circ$, $\lambda(1; 1) = 0.012c$ and $3.3\cdot10^5 < Re_c < 1.0\cdot10^6$ ($C_\mu$ is varied by varying $Re_c$ at fixed actuation power). The data in Figure 8.5 show that within the range $0.4\% < C_\mu < 1.6\%$, the lift increment produced by the synthetic jets for a fixed $C_\mu$ is approximately 70% of the lift increment produced by the fluidic oscillators. Alternatively, for a given $\Delta C_l$ the required $C_\mu$ from the synthetic jets is approximately twice as large as for the fluidic oscillators (of course, the synthetic jets do not require a fluid source unlike the fluidic oscillators). Compared to $\delta = 20^\circ$, at $\delta = 40^\circ$ the lift increment induced by the fluidic oscillator increases more rapidly with $C_\mu$, suggesting that similar results may be achievable with synthetic jets if a sufficiently high momentum coefficient can be realized.

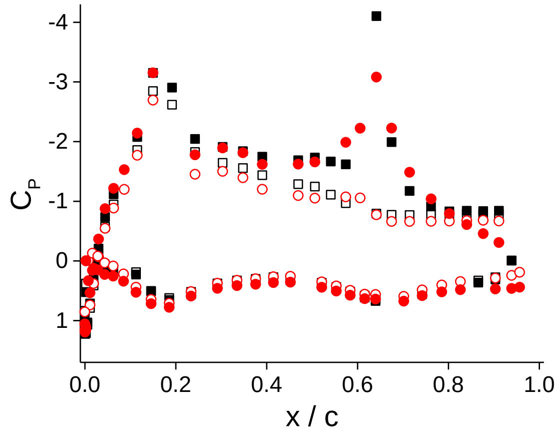

***Figure 8.6.*** *Comparison of actuator types. Synthetic jets ($\delta = 25^\circ$, $Re_c = 3.3\cdot10^5$, $\lambda(1; 1) = 0.012c$, $\alpha = 4^\circ$): (□) Unactuated, (■) Actuated ($C_\mu = 2.0\%$). Fluidic oscillators ($\delta = 20^\circ$, $Re_c = 6.7\cdot10^5$, $\alpha = 4^\circ$): (○) Unactuated, (●) Actuated ($C_\mu = 0.8\%$).*

The corresponding circumferential pressure distributions are shown in Figure 8.6, comparing synthetic jets operated at $C_\mu = 2\%$ ($\delta = 25^\circ$, $\lambda(1; 1) = 0.012c$ and $Re_c = 3.3\cdot10^5$) and fluidic oscillators at $C_\mu = 0.8\%$ ($\delta = 20^\circ$ and $Re_c = 6.7\cdot10^5$), at nearly

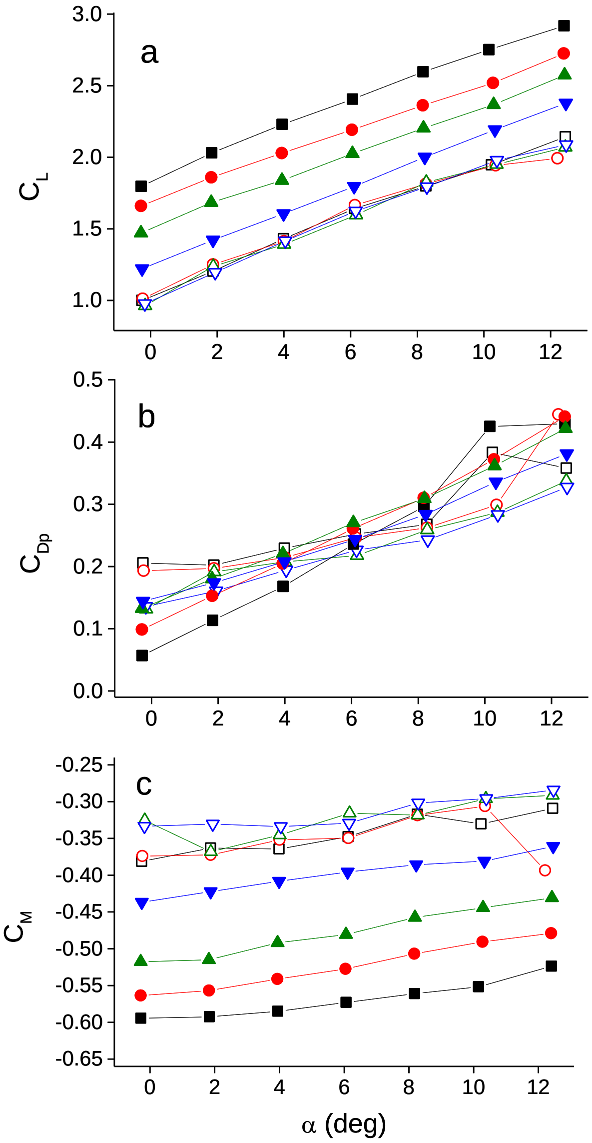

***Figure 8.7.*** *Variation of (a) $C_l$, (b) $C_{dp}$, (c) $C_m$ with $\alpha$; $\lambda(1; 1) = 0.012c$. Unactuated (open symbols), actuated (closed symbols). $Re_c$ = (■) $3.3 \cdot 10^5$ ($C_\mu = 2.0\%$), (●) $5.0 \cdot 10^5$ ($C_\mu = 0.88\%$), (▲) $6.7 \cdot 10^5$ ($C_\mu = 0.49\%$), (▼) $1.0 \cdot 10^6$ ($C_\mu = 0.22\%$).*

equal $\Delta C_l$. It is noteworthy that the synthetic jet produces a stronger suction peak near the orifice than the fluidic oscillator, but the pressure distribution exhibits a stronger adverse pressure gradient downstream, suggesting that the effects of the synthetic jet are more localized to the domain near the orifice. The fluidic oscillator has a larger global effect as is evident from the increased upstream suction and the induced adverse pressure gradient downstream to the trailing edge indicating complete flow attachment (for $\delta = 20^{\circ}$).

Figure 8.7a shows the variation of $C_l$ with angle of attack ($0^{\circ} < \alpha < 12^{\circ}$) for $\lambda(1; 1) = 0.012c$ (all jets active). Results are shown for $Re_c = 3.3 \cdot 10^5$, $5.0 \cdot 10^5$, $6.7 \cdot 10^5$, and $1.0 \cdot 10^6$, with corresponding $C_{\mu}$ = 2.0%, 0.88%, 0.49% and 0.22%, respectively. For each $Re_c$, the lift increment has respective nominal values of 0.79, 0.61, 0.45 and 0.22 with no changes in the lift curve slope and hence is nominally invariant with $\alpha$. At $\alpha = 12^{\circ}$, a slight reduction in the unactuated lift curve slope corresponds to the onset of stall, while the lift curve slope is unchanged for the actuated condition, suggesting that improving flow attachment over the flap may delay stall onset at high $\alpha$. The corresponding pressure drag $C_{dp}$ is shown in Figure 8.7b. Actuation reduces pressure drag at lower $\alpha$ because the extent of separation over the flap is reduced (cf. Figure 8.4). At higher $\alpha$, although separation near the flap is mitigated, $C_{dp}$ increases because $C_l$ is increased to much higher levels, creating significant lift-induced drag. The suction peak near the juncture and increased suction downstream (cf. Figure 8.4) induce a nose-down pitching moment, as shown by the variation of pitching moment $C_m$ (about $c/4$) in Figure 8.7c. The deflected flap ($\delta = 25^{\circ}$) creates a nose-down pitching moment on the unactuated airfoil ($C_m \approx -0.35$) which is enhanced by the actuation to a degree comparable to the increase in lift. Since the largest effect of actuation is an increase in suction on the aft portion of the suction surface in proportion to the lift increment, actuation also generates a corresponding downward pitching moment.

## 8.2. *Flow Attachment Mechanism of the Control Jets*

The aerodynamic effects discussed are consequences of alterations to the global flow field, which occur due to changes in the local flow near the synthetic jet actuator. Therefore, the flow field near a single jet is analyzed using 3-D velocity measurements to assess the structure of the controlled flow and the alteration of the distributions of spanwise and streamwise vorticity.

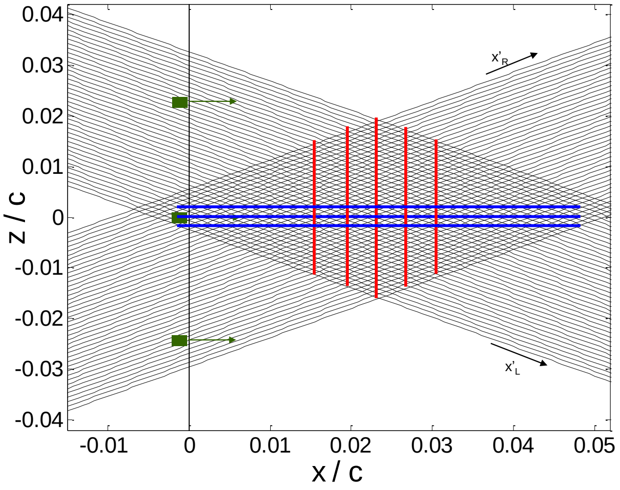

***Figure 8.8.*** *Dual-plane PIV technique; orifice at x / c = 0, arrows denote jets. Measurements in diagonal planes (—), computed results in xy (—) and yz (—) planes.*

The 3-D measurements are obtained by combining groups of 2-D PIV measurements in parallel planes taken along opposite diagonals. The dual-plane PIV is illustrated schematically in Figure 8.8. Planar (2-D) PIV measurements are made in spanwise-normal planes rotated $\pm 30^\circ$ about the cross-stream ($y$) axis. The angle between the planes and free stream, the laser sheet thickness and the time-lapse between laser pulses are selected to ensure measurement accuracy of both the streamwise and spanwise velocity components. Along each diagonal (“left” and “right”) direction, the measurements are made in 41 parallel planes with local planar axes ($x'_{\mathrm{Li}}$, $y'_{\mathrm{Li}}$) and ($x'_{\mathrm{Ri}}$,

$y'_{Ri}$) for $i = 1, \ldots, 41$. Sets of 500 images per plane are obtained for all 82 planes within a field of view measuring 29 x 22 mm with a nominal spatial resolution of 18 μm/pixel. The plane spacing of 0.35 mm is comparable to the spacing between velocity vectors within any ($x'$, $y'$) plane. The groups of left and right planes intersect near one of the actuator jets in the spanwise array forming a rhombus-shaped volume extending from 3 mm upstream to 24 mm downstream of the jet.

In each ($x'_{Li}$, $y'_{Li}$) and ($x'_{Ri}$, $y'_{Ri}$) plane, the 2-D velocities [$u'_{Li}$, $v'_{Li}$] and [$u'_{Ri}$, $v'_{Ri}$] are computed using a conventional processing technique. Each plane is located in 3-D ($x$, $y$, $z$) space according to a reference line ($x$, $y$) = (0, 0) estimated from the overhang edge position in the field of view and the spanwise coordinates $z_{Li}$ and $z_{Ri}$ where the reference line intersects plane $i$ (left or right). Measurement coordinates in the ($x'$, $y'$, $z$) form are converted across the entire data set to the form ($x$, $y$, $z$). To obtain values uniformly spaced along the ($x$, $y$, $z$) axes for $u'_L$, $u'_R$, $v'_L$ and $v'_R$, a 3-D interpolant is constructed using the measurements for each function and interpolated values are computed at the appropriate points. Because the $y'$ and $y$ axes are identical, both measured cross-stream velocity components $v'_L$ and $v'_R$ correspond to the true cross-stream component $v$. Therefore, by comparing the spatial distributions of $v'_L$ and $v'_R$, adjustments can be made to ensure proper alignment of the planes. After aligning the planes by matching $v'_L$ and $v'_R$, velocity components $u$ and $w$ are computed from $u'_L$ and $u'_R$. The resulting velocity values ($u$, $v$, $w$) along grids evenly spaced in ($x$, $y$, $z$) are subsequently used to compute vorticity and produce vector plots along planes parallel to the $xy$ and $yz$ planes.

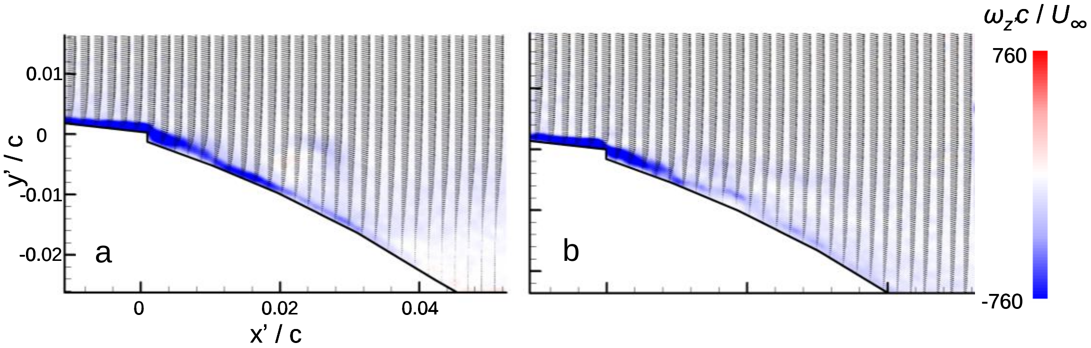

***Figure 8.9.*** *Color raster plots of vorticity concentration and velocity vectors in left diagonal (a) and right diagonal (b) planes.*

Examples of vorticity and velocity distributions in the left and right planes are shown in Figure 8.9. Measurements are made for $\alpha = 4^\circ$ and $Re_c = 5.0 \cdot 10^5$ with $\lambda(2;1) = 0.023c$ ($k/n = 0.5$, $C_\mu = 0.44\%$). Similar features are present in both flow fields, including an attached upstream boundary layer and a downstream flow that remains attached to ~0.04*c* downstream of the orifice ($x = 0$) before beginning to separate again. The diagonal planes shown intersect near the jet centerline 0.02*c* downstream of the orifice, where the flow fields contain off-surface vorticity concentrations that are associated with the intersection between the actuator jet and the plane. Flow in the center of this concentration is oriented away from the surface, while a flow toward the surface is observed upstream of this concentration. By combining the results from all diagonal planes, velocity and vorticity fields of the three-dimensional flow downstream of the actuator jet can be constructed.

Velocity vectors in cross sections of the intersection volume parallel to the *xy* plane are shown in Figure 8.10. The unactuated flow along the jet centerline ($\Delta z/\lambda = 0$; Figure 8.10a) separates at the orifice, forming a detached layer of vorticity downstream. The flow field includes the (attached) upstream boundary layer and separation domain

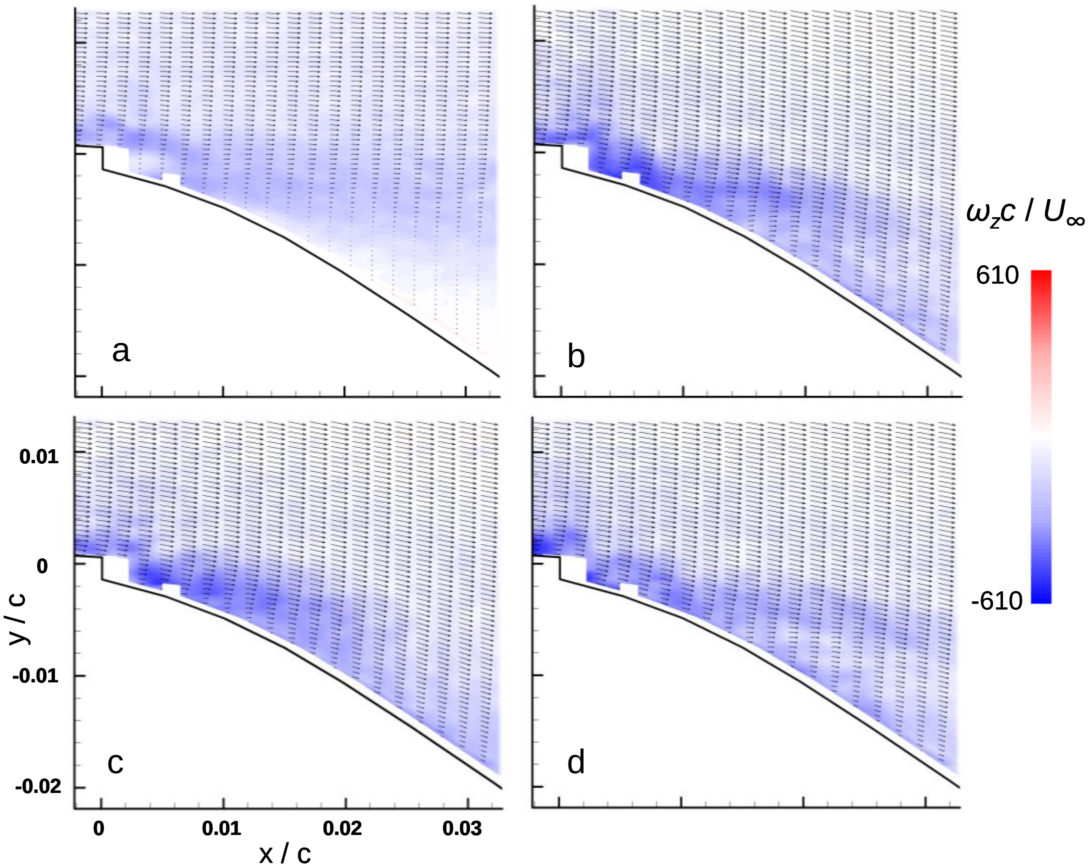

*Figure 8.10. Computed flow fields in the xy (spanwise normal) plane: Jet centerline ($\Delta z$ = 0) unactuated (a) and actuated (b). Actuated off-centerline: $\Delta z$ = −0.07 (c) and 0.07 (d). Color contours denote spanwise vorticity.*

immediately downstream, so vorticity is observed throughout nearly the entire flow field. At $x/c$ = 0.02-0.03 downstream from the orifice, separation leads to reverse flow above the wall. In the presence of actuation (Figure 8.10b) the flow along the surface downstream of the orifice on the jet centerline accelerates and becomes attached. The flow outside of the near-wall region accelerates (compared to the unactuated condition) and is turned toward the surface. From $x/c$ = 0.01 downstream of the orifice, the actuation turns the global flow (away from the jet centerline) toward the wall (cf. Figure 8.9) while the local flow (on the jet centerline) is directed away from the wall, indicating the formation of counter-rotating streamwise vortices adjacent to the wall on either side of the jet. The flow fields off-centerline ($\Delta z/\lambda$ = −0.07 and 0.07; Figures 8.10c-d)

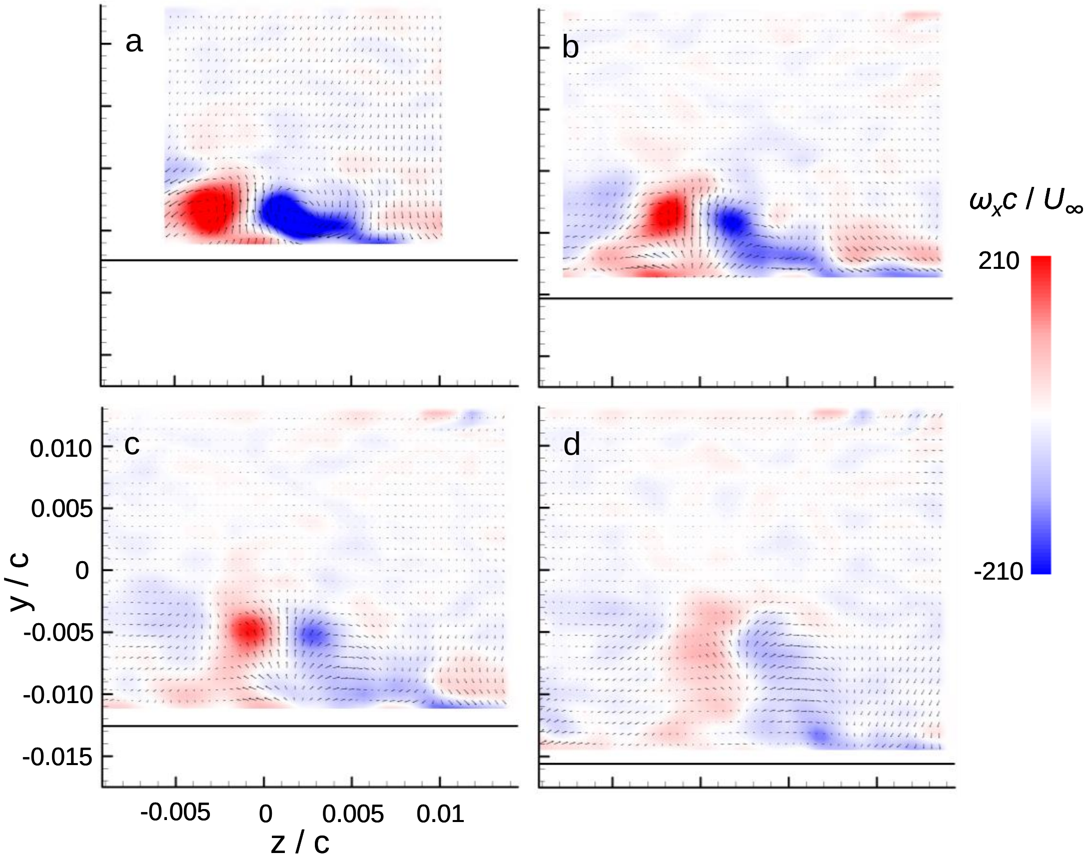

***Figure 8.11.*** *Computed induced flow fields in the yz (streamwise normal) plane: $x / \lambda$ = (a) 0.56, (b) 0.75, (c) 0.94, (d) 1.12. Color contours denote streamwise vorticity.*

indicate that there are also significant spanwise vorticity concentrations away from the wall. It is noteworthy that the off-center flow fields are somewhat asymmetric owing to nonuniformities in the actuation jets. Due to the rhombus-shaped cross section of the intersection volume, flow fields with the same streamwise extent cannot be obtained farther off-centerline as indicated in Figure 8.8.

Streamwise vorticity contours and induced velocity in cross sections of the intersection volume parallel to the *yz* plane are shown in Figures 8.11a-d for the actuated flow at streamwise positions $x/\lambda = 0.56$, 0.75, 0.94 and 1.12 (corresponding to $x/c = 0.013$, 0.017, 0.021 and 0.026, respectively) downstream of the orifice (at $z / c = -0.002$). The induced velocity is computed by subtracting the spanwise-averaged mean velocity profile $v(y)$ from the time-averaged flow field; doing so does not alter $\partial v/\partial z$, and therefore does not affect the streamwise vorticity. The circulating flow domains that are associated with the formation of counter-rotating streamwise vortices downstream of the jet orifice near the wall (as discussed in connection with Figure 8.9) are exhibited more clearly here (note that in the absence of actuation the baseline flow is featureless). At $x/\lambda = 0.56$ (Figure 8.11a) a strong, well organized vortex pair ($0.005c$ distance between centers) is present $0.004c$ above the surface. The streamwise vortices move away from the surface and become less concentrated at $x/\lambda = 0.75$ and 0.94 (Figure 8.11b-c) before they weaken and diffuse at $x/\lambda = 1.12$ (Figure 8.11d). This diffusion may be attributed to the pulsation of the synthetic jet coupled with the strong adverse pressure gradient in this domain (cf. Figure 8.4) that may contribute to loss of coherence owing to vortex core instability and breakdown. Based on the increase in suction upstream of the actuator, the performance of the actuator may improve by using a second jet actuator operating downstream of the first (near $x/\lambda = 1$) to help mitigate the adverse pressure gradient, produce a new system of vortices, and enable the upstream vortices to persist over an extended streamwise domain.

Near the wall, as indicated in Figures 8.11a-b, directly below the centerline of the vortex pair, the streamwise vorticity has opposing senses on either side, which indicates the presence of a streamwise stagnation domain at the wall. Near $z/c = 0.01$ ($z/\lambda = 0.4$) is a domain of increased downward velocity adjacent to the vortex. Similarly, there is another streamwise stagnation domain near $z/c = 0.01$. The rotation induced by these vortices transports higher-momentum flow closer to the surface (to the side of the jet) and lower-momentum flow away from the surface (toward the core of the jet). As the

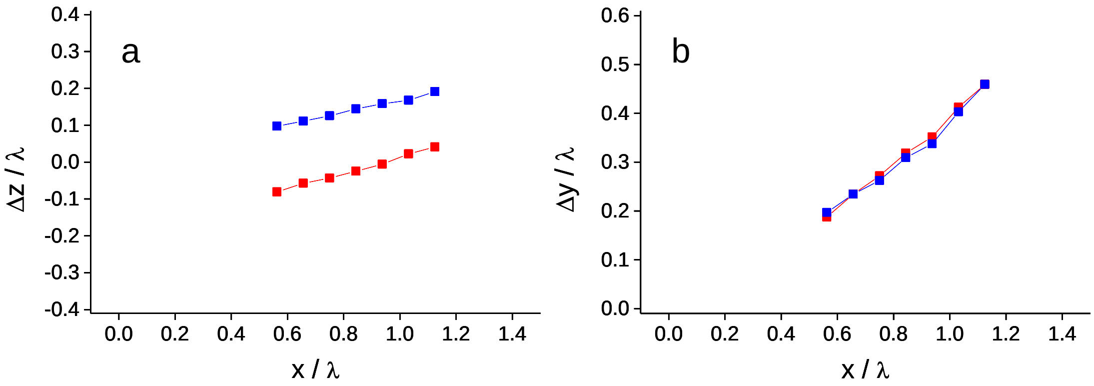

***Figure 8.12.*** *Streamwise vortex migration: (a) spanwise position and (b) cross-stream distance above airfoil surface. Counterclockwise (🟥) and clockwise (🟦) vortices.*

vorticity concentrations weaken and move away from the surface (Figures 8.11b-c), some of the upward flow turns away from the core of the jet below the center of the vorticity concentration. It is noteworthy that the adjacent jet ($z/c = -0.023$) to the left of the center jet ($z/c = 0$) is weaker (Figures 8.11b-c) and therefore the downward velocity domain to the left of the center jet is skewed toward the center jet (presumably due to stronger suction induced by the center jet; cf. Figure 8.4).

The streamwise evolution of the vortex position is shown in Figure 8.12, measured from a series of parallel *yz*-plane cross sections of the intersection volume similar to those in Figure 8.11. These data show some spanwise vortex migration in the *xz* plane (Figure 8.12a). The vortex centers remain separated by the same nominal distance of $0.2\lambda$ and migrate toward the neighboring jet at $z/\lambda = 1$, and may be attributed to slight spanwise nonuniformities in the actuation. Figure 8.12b shows the cross-stream distance of the vortex centers from the wall $\Delta y$ as the adverse streamwise pressure gradient (cf. Figure 8.4) intensifies.

It is evident from Figure 8.11 that the streamwise vorticity concentrations near the wall immediately downstream of the actuator orifice are associated with an exchange of high- and low-momentum fluid near the wall that leads to an increased extent of flow attachment. An improved understanding of the role played by the vorticity concentrations can be gained by comparing the flow near the jet orifice to a three-dimensional turbulent rectangular wall jet, which was investigated in numerous earlier studies (e.g. Newman et al. 1972, Launder and Rodi 1983 and Craft and Launder 2001). These authors investigated the rapid spreading of the jet in the plane parallel to the wall and showed that at the outer edges of the jet (in relation to the symmetry plane), secondary flow structures form that direct the flow outside the jet away from the jet centerline (rather than toward the centerline, as would be expected if the jet expansion were purely due to entrainment). Such secondary structures correspond to streamwise vorticity concentrations of opposite sense near the outer edges of the jet, where flow is directed upward (away from the surface) and away from the jet centerline. The CFD studies of Craft and Launder (2001) show that the streamwise vortices form as a result of the nonuniform distribution of Reynolds stresses created by the jet interaction with the wall. Therefore, an array of low-aspect-ratio three-dimensional wall jets forms a row of closely-spaced streamwise vortices that move higher-momentum fluid toward the wall, in a manner similar to an array of vortex generators. However, by varying the jet momentum the strength of the vortices can be varied without changing the external flow, thereby allowing the extent of the momentum exchange to be varied.

The effects of the actuation on the flow are analyzed by computing the streamwise and cross stream pressure gradients that are induced by the interaction of the actuation jet with the cross flow. The pressure gradients are estimated from the (time-averaged) PIV measurements using the steady Navier-Stokes equations. Figure 8.13 shows the average (spanwise) pressure gradient over all left diagonal planes spanning a

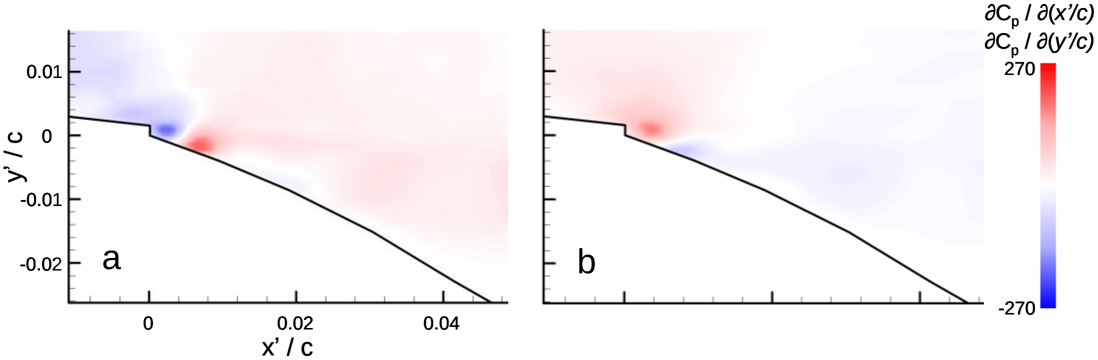

***Figure 8.13.*** *Spanwise-averaged pressure gradient in left diagonal plane: (a) streamwise ($\partial C_p/\partial(x'/c)$) and (b) cross-stream ($\partial C_p/\partial(y'/c)$).*

single period $\lambda$. The streamwise pressure gradient $\partial C_p/\partial(x'/c)$ (Figure 8.13a) is favorable (negative) upstream of the jet array, indicating accelerating flow, and intensifies immediately downstream of the orifice owing to the suction created by the synthetic jet. Farther downstream, the pressure gradient becomes adverse (positive) indicating flow deceleration. Downstream of the actuator the scaled pressure gradients $\partial C_\mathrm{p}/\partial(x/c)$ is on the order of 50 and is comparable to the pressure gradient measured (with considerably less spatial resolution) near the orifice from pressure distributions in Figure 8.4. However, at the wall near $x' / c = 0.02$ there is a small domain of favorable pressure gradient that indicates suction induced by the streamwise vortices (cf. Figure 8.11). The cross-stream gradient $\partial C_p/\partial(y'/c)$ (Figure 8.13b) indicates a positive gradient near the orifice which occurs due to suction by the jet (pressure decreasing toward the wall). The weak negative $\partial C_p/\partial(y'/c)$ downstream of the orifice is associated with the adverse pressure gradient along the deflected surface of the airfoil.

Finally, Figure 8.14 shows the pressure gradient $\partial C_p/\partial(\ell/c)$ along the local tangent to the wall from the computed *xy* plane on the jet centerline (cf. Figure 8.10b). It is remarkable that the pressure gradient in the boundary layer immediately upstream of the orifice is positive (adverse), indicating local blockage and deceleration along the jet

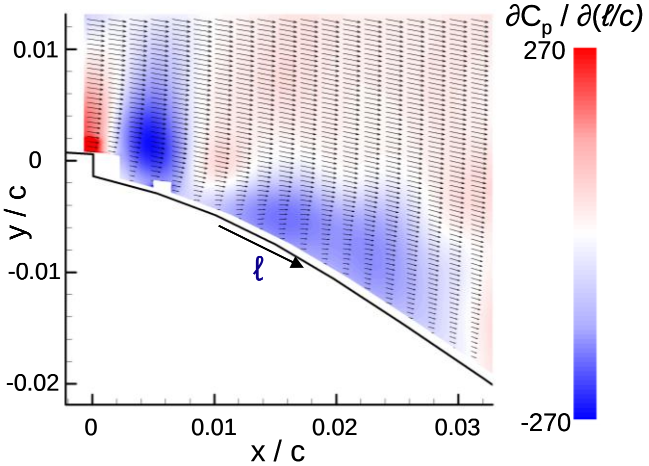

***Figure 8.14.*** *Pressure gradient* $\partial C_p / \partial(\ell/c)$ *along airfoil surface tangent* $\ell$ *in the xy plane along the jet centerline* ($z / c = -0.002$).

centerline, in contrast to the wavelength-averaged data in Figure 8.13. The data in Figure 8.14 indicate that the presence of the jet introduces a local spanwise-periodic blockage in conjunction with spanwise-periodic favorable gradients between the jets that are induced by the low pressure domain created by the actuator. These effects appear to be a manifestation of the local "virtual" change in the apparent shape of the airfoil that mitigate the adverse pressure gradient in the baseline flow and promote attachment.

Within $0.01 < x/c < 0.025$, where the flow away from the surface (induced by the jet) is strongest, there is also a negative (favorable) pressure gradient. This suggests that, as with the streamwise vortices formed by conventional vortex generators, the streamwise vortices engendered by the jet near the surface induce suction that draws the surrounding flow toward the surface and therefore promotes flow attachment. Farther downstream ($x/c = 0.03$) the effect diminishes as the jet weakens and migrates away from the wall (cf. Figure 8.11). The global pressure gradient becomes adverse and the flow eventually separates (cf. Figure 8.4).

Chapter 9 contains an investigation into the use of active flow control to improve the high-lift performance of an airfoil with a Fowler flap. Fluidic oscillators are used to manipulate the flow from the cove between the flap and the main element in a manner that improves its effectiveness at increasing the extent of flow attachment along the flap.

# CHAPTER 9

# SEPARATION CONTROL ON A FOWLER FLAP

A Fowler flap high-lift configuration contains a cove between the flap and the main element through which a 2-D wall jet is formed near the juncture between the elements that substantially increases the extent of attachment on the flap suction surface (Smith 1975). Active flow control can be used on a Fowler flap to manipulate the flow between the elements such that its effectiveness for improving flow attachment over the flap is enhanced. By incorporating a spanwise array of .fluidic oscillators into the leading edge of the flap (as illustrated schematically in Figure 2.3), the cove flow can be directed toward the flap surface, resulting in significantly greater extent of flow attachment (and correspondingly greater lift) than through use of the cove flow alone. Because the flow attachment occurs as a result of interaction between spanwise-periodic structures near the actuator orifices, the effect of varying the spanwise wavelength, i.e. the spacing between actuator jets, is also investigated.

## *9.1. Characterization of the Baseline Flow*

As discussed in Chapter 1, in a multi-element airfoil system successive elements are separated by cross-stream gaps through which a flow is driven by the pressure on the pressure surface of the airfoil. The interactions between these cove flows and the cross flow over the suction surface of the flap lead to reduced adverse pressure gradient, increased circulation on the main body, and improved merging of the boundary layer on the upstream element with a thinner boundary layer on the flap. The effects of the gap on the aerodynamic performance of the present airfoil model were assessed from a series of

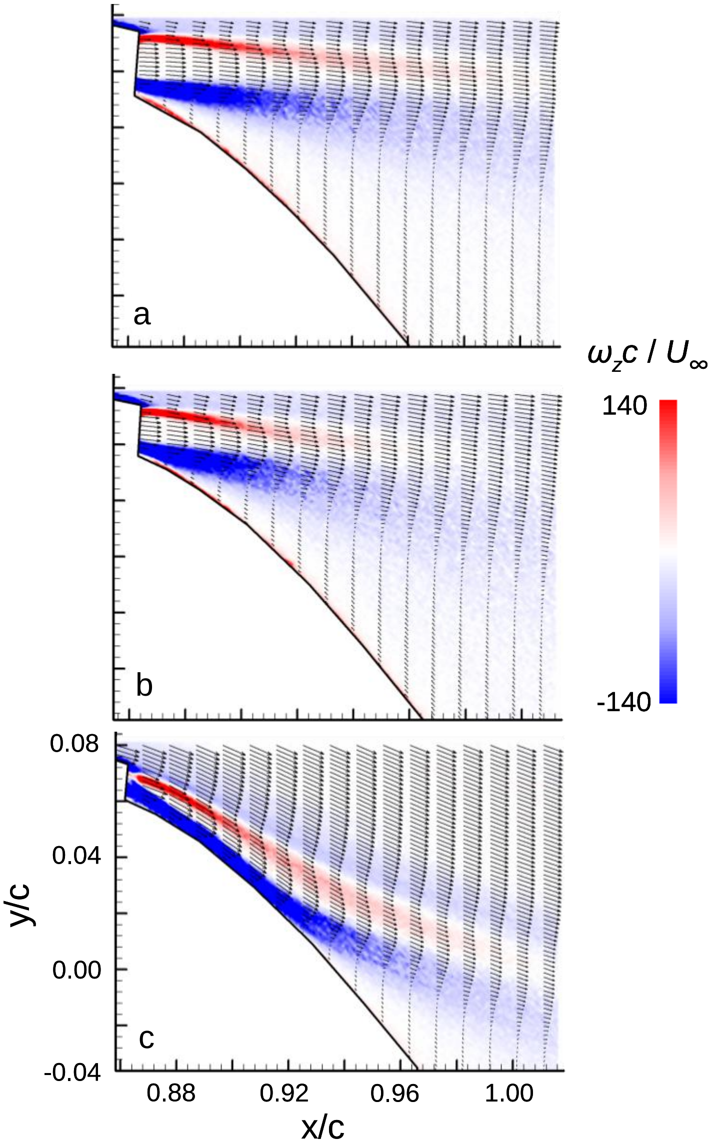

***Figure 9.1**. Flow field downstream of the flap cove ($\delta$ = 42º, $\alpha$ = 4°, $Re_c = 6.7 \cdot 10^5$) for $\gamma/c$ = 1.5% (a), 1.0% (b), and 0.5% (c). Concentrations of clockwise (CW, blue) and counterclockwise (CCW, red) spanwise vorticity are shown using color raster plots.*

measurements over a range of flap deflection ($\delta$) and cross-stream gap ($\gamma$) with emphasis on determination of an optimal configuration.

Using the wind tunnel model shown in Figure 2.3, the flow fields in the vicinity of the cove for three cross stream gaps ($\gamma/c$ = 0.5%, 1%, and 1.5%), were measured using PIV (45 μm/pixel) at midspan ($z$ = 0) and are shown in Figure 9.1 using vorticity color raster plots and cross stream distributions of velocity vectors. These images show the formation and advection of the nominally 2-D “cove jet” that is driven by the flow on the pressure side of the airfoil. The jet is characterized by the formation of clockwise (CW) and counterclockwise (CCW) spanwise vorticity layers at its upper and lower edges. The lower layer interacts with the flow over the surface of the flap while the upper layer merges with the vorticity layer in the boundary layer of the main element. For $\gamma/c = 1.5\%$ (Figure 9.1a), the lower vorticity layer separates from the surface of the flap and a recirculation region is formed downstream of the cove that is accompanied by the formation of a thin layer of CCW vorticity near the surface. The interaction of the upper vorticity layer of the jet with the boundary layer from the main element results in a thinner vorticity layer owing to vorticity diffusion and cancellation and forms a wake-like structure downstream of the trailing edge of the main element. When the cross-stream gap is reduced to $\gamma/c = 1.0\%$ (Figure 9.1b) the flow speed through the cove increases as is evidenced by the thicker lower vorticity layer, and by the intensified interaction of the upper vorticity layer with the main element boundary layer. As a result of the proximity of the flap surface, the cove flow is deflected towards the surface ostensibly owing to enhanced entrainment and lower pressure. As the cross stream gap is reduced to $\gamma/c = 0.5\%$ (Figure 9.1c), the lower vorticity layer remains attached to the surface of the airfoil and the increased momentum of the jet entrains the flow over the main element, resulting in the main element boundary layer turning toward the flap and accelerating. The wake-like structure between the upper vorticity layer in the jet and the main element vorticity layer is somewhat diminished and the attached flow over the flap surface is comprised of three vorticity layers that remain reasonably coherent through separation at about $0.07c$ downstream of the cove. These data indicate that the cove jet does not have

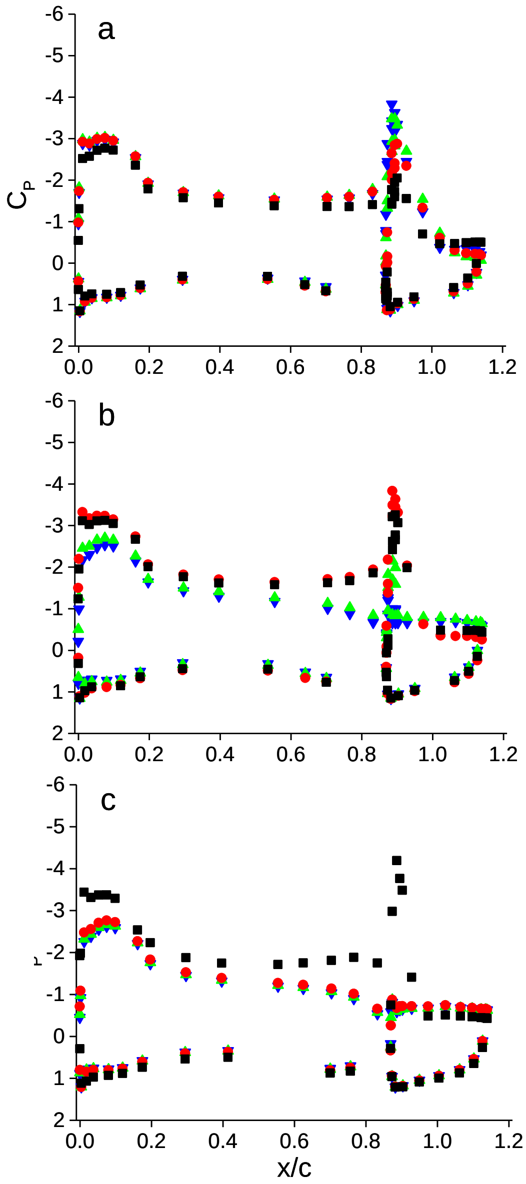

***Figure 9.2.*** *Pressure distribution around the airfoil ($\alpha$ = 4°, $Re_c$ = $6.7 \cdot 10^5$): $\delta$ = 33° (a), 42° (b) and 51° (c). $\gamma/c$ = 0 (■), 0.5% (●), 1.0% (▲), 1.5% (▼).*

sufficient momentum to overcome the adverse pressure gradient over the entire surface of the flap. Because this jet is driven by the flow on the pressure surface, decreasing the jet width results in increased losses within the cove and weakens the cove jet. These interactions of the cove jet with the main element boundary layer and the surface of the flap suggest that a higher momentum control jet close to the surface may be able to effect flow attachment over the flap across a greater streamwise extent.

Pressure distributions for the baseline airfoil are shown in Figure 9.2a-c for $\delta = 33°$, 42° and 51°, respectively, and $0 \leq \gamma/c \leq 1.5\%$. Due to the drooped leading-edge, there is a favorable pressure gradient on the suction surface near the leading edge that culminates in a suction peak near $x/c = 0.1$, the location of which is largely invariant with $\delta$ or $\gamma/c$. As $\gamma/c$ is varied, there are significant differences in the flap suction peak near $x/c = 0.9$ due to changes in the interaction between the flap and main body (cf. Figure 9.1). This is apparent in Figure 9.2a ($\delta = 33°$) where the flap suction peak increases with $\gamma/c$. For $\gamma/c = 0$ the flow appears to separate around $x/c = 1.0$, whereas an increase in $\gamma/c$ results in pressure recovery downstream to the trailing edge. At $\delta = 42°$ (Figure 9.2b), with gaps of $\gamma/c = 0$ and 0.5% the flap suction peak is strongest and separation occurs immediately downstream of the peak, corresponding to the partial attachment shown in Figure 9.2c. The increase in the suction peak strength is accompanied by a significant increase in suction over the main element as far upstream as the leading edge. Of particular note is that the increased suction is also present when the cross-stream gap is nearly absent ($\gamma/c = 0$), indicating that an excessively large gap can result in premature separation (when $\gamma/c = 1.0\%$ and 1.5% separation occurs at the cove, $x/c = 0.9$, Figure 9.1a-b). When $\delta = 51°$ (Figure 9.2c) the suction peak on the flap is only present for $\gamma/c = 0$ and for larger gap settings the separation at the cove also results in significant loss in suction on the main element with corresponding loss in lift.

The variation in the location of separation (Figure 9.3) over a range of flap deflections ($25° \leq \delta \leq 42°$) and cross-stream gap widths ($\gamma/c = 0$, 0.5, 1, and 1.5%) is

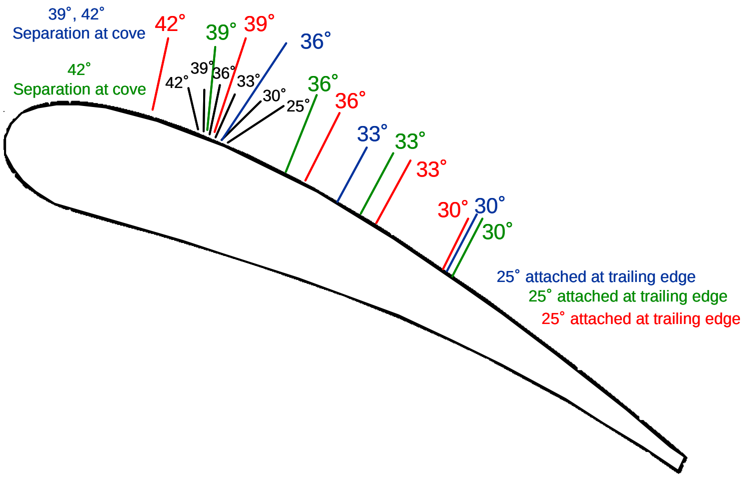

***Figure 9.3.*** *Separation location on the suction surface of the flap for a range of flap deflection angles: $\gamma/c = 0$ (black), 0.5% (red), 1.0% (green), 1.5% (blue).*

measured from PIV flow fields similar to the measurements in Figure 9.1. For $\gamma/c = 0$ (black), when the gap is reduced to a small (O[0.001$c$]) opening to prevent the flap from contacting the main body, the separation locations for all flap angles are clustered near 0.25$c_f$ and move upstream as $\delta$ is increased. Because of the lack of a cove flow, the boundary layer on the flap suction surface is influenced primarily by the relatively thick main body boundary layer which is prone to separation as the turning of the flow at the flap juncture increases with $\delta$. The presence of the cove jet (cf. Figure 9.1) with $\gamma/c = 0.5\%$ (red) results in delay of separation up to near the trailing edge for $\delta = 25°$ but as $\delta$ increases, the separation moves upstream to 0.6$c_f$ at $\delta = 30^{\circ}$, 0.4$c_f$ at $\delta = 36^{\circ}$,and 0.2$c_f$ at $\delta = 42°$. For gaps of $\gamma/c = 1$ (green) and 1.5% (blue) the separation locations are similar to corresponding locations for $\gamma/c = 0.5\%$, but the diminished effectiveness of the cove jet increases the sensitivity of the flow to the adverse pressure gradient and the separation moves up to the cove at $42^{\circ}$. These measurements are used to determine the proper placement of the active flow control actuators as discussed in §9.2.

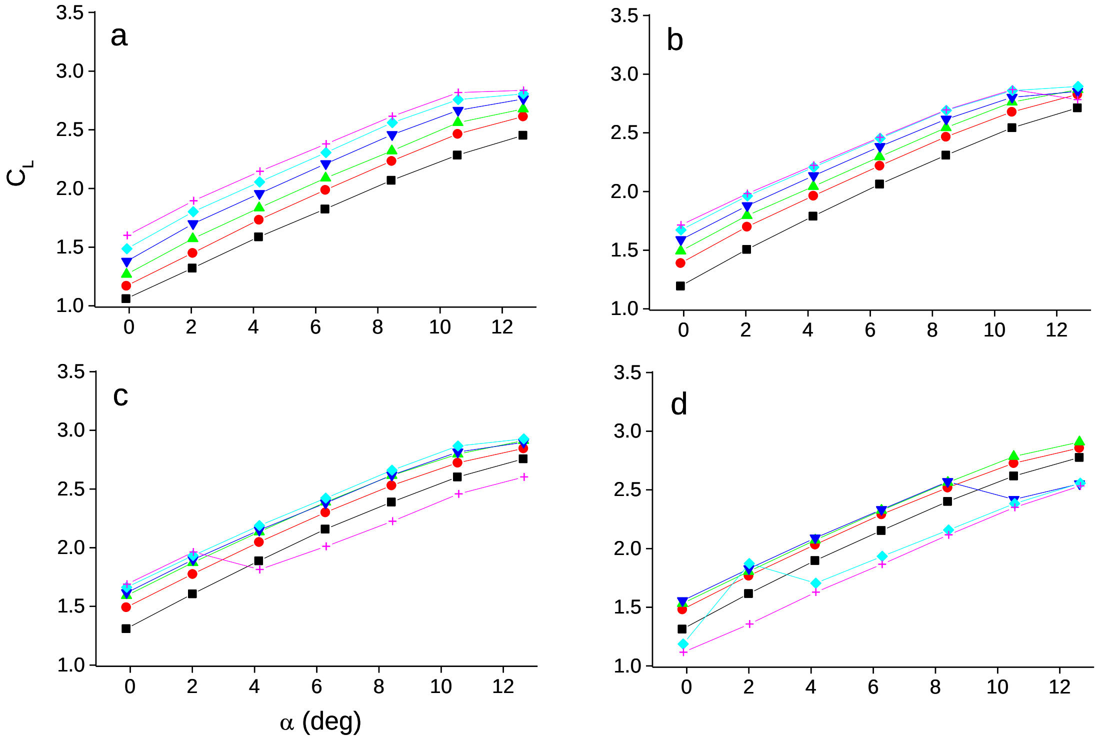

***Figure 9.4.*** *Variation of $C_L$ with $\alpha$ ($Re_c$ = $6.7 \cdot 10^5$): $\gamma/c$ = 0 (a), 0.5% (b), 1.0% (c), and 1.5% (d). $\delta$ = 25° (■), 30° (●), 33° (▲), 36° (▼), 39° (◆), 42°(+).*

The variation in aerodynamic forces with $\delta$ and $\gamma/c$ are assessed from load cell measurements (cf., §2.3). Figure 9.4 shows the variation of $C_L$ with angle of attack for $0^\circ \leq \alpha \leq 12^\circ$. In the absence of a gap ($\gamma/c = 0$; Figure 9.4a) the lift increases monotonically with $\delta$ and there is almost no change in the (nearly linear) slope except at $\alpha = 12^\circ$, where a slight reduction in the lift curve slope (particularly for larger $\delta$) corresponds to the onset of trailing edge stall. With $\gamma/c = 0.5\%$ (Figure 9.4b) there is no change in the lift curve slope and there is an increase in lift (relative to corresponding measurements for $\gamma/c = 0$) on the order of $\Delta C_L \sim 0.1\text{-}0.2$ that is nearly invariant with $\alpha$. However, this increase diminishes as $\delta$ is increased (for example, the differences in $C_L$ between $\gamma/c = 0$ and 0.5% at $\alpha = 4^\circ$ for $\delta = 25^\circ$ and 42° are 0.26 and 0.08, respectively). As the gap is increased to 1.0% (Figure 9.4c) lift continues to increase for $\delta < 36^\circ$ but

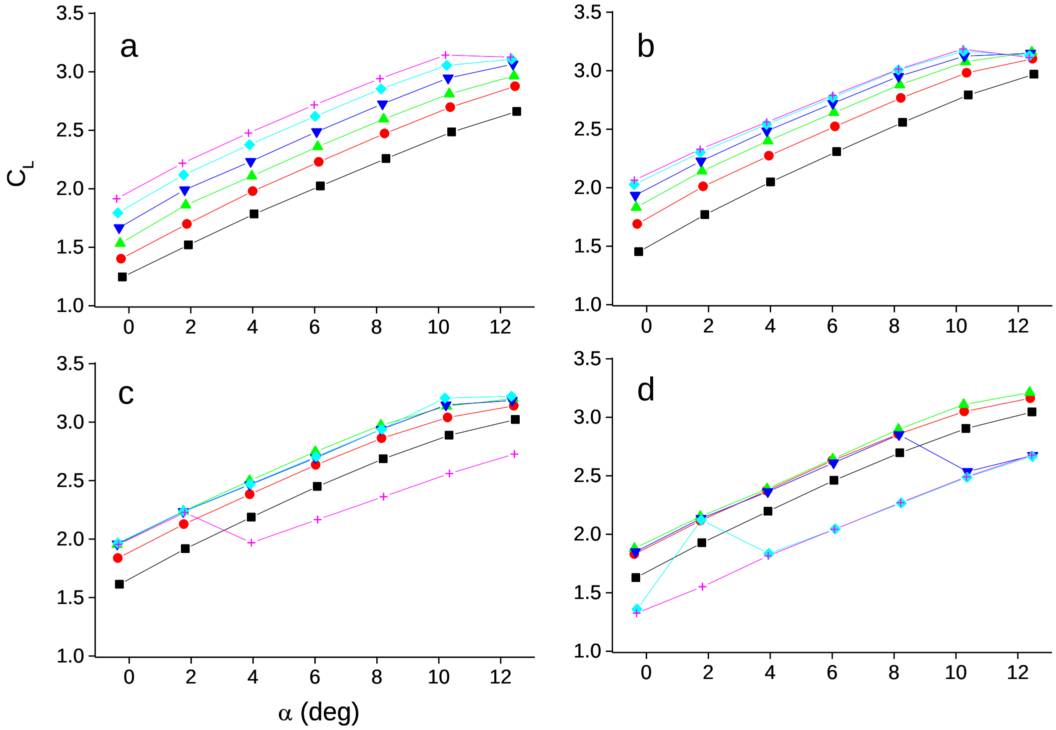

***Figure 9.5.*** *Variation of $C_l$ (computed from centerline $C_p$ distributions) with $\alpha$ ($Re_c = 6.7 \cdot 10^5$): $\gamma/c$ = 0 (a), 0.5% (b), 1.0% (c), and 1.5% (d). $\delta$ = 25° (■), 30° (●), 33° (▲), 36° (▼), 39° (♦), 42°(+).*

appears to reach a limit for larger deflections (for example, at $\alpha = 0°$ $C_L$ never exceeds 1.7 regardless of $\delta$). Most noticeable is the abrupt lift loss at $\delta = 42°$ and $\alpha = 4°$ corresponding to the onset of separation at the cove (cf. Figures 9.1 and 9.3). It is noteworthy that despite this change, the slope of the lift curve remains nearly invariant, indicating that once the flap is fully stalled, its effect on the main element is small and independent of $\alpha$. For $\gamma/c$ = 1.5% (Figure 9.4d) flap stall is observed for $\delta$ = 36° and 39° and the lift decreases as for $\gamma/c$ = 1.0% and $\delta = 42^\circ$.

For comparison, the two-dimensional lift coefficient $C_l$ (computed from the centerline pressure distribution in a similar manner to the results in Chapters 3-6) is shown in Figure 9.5. The centerline $C_l$ values are approximately 20% larger than the

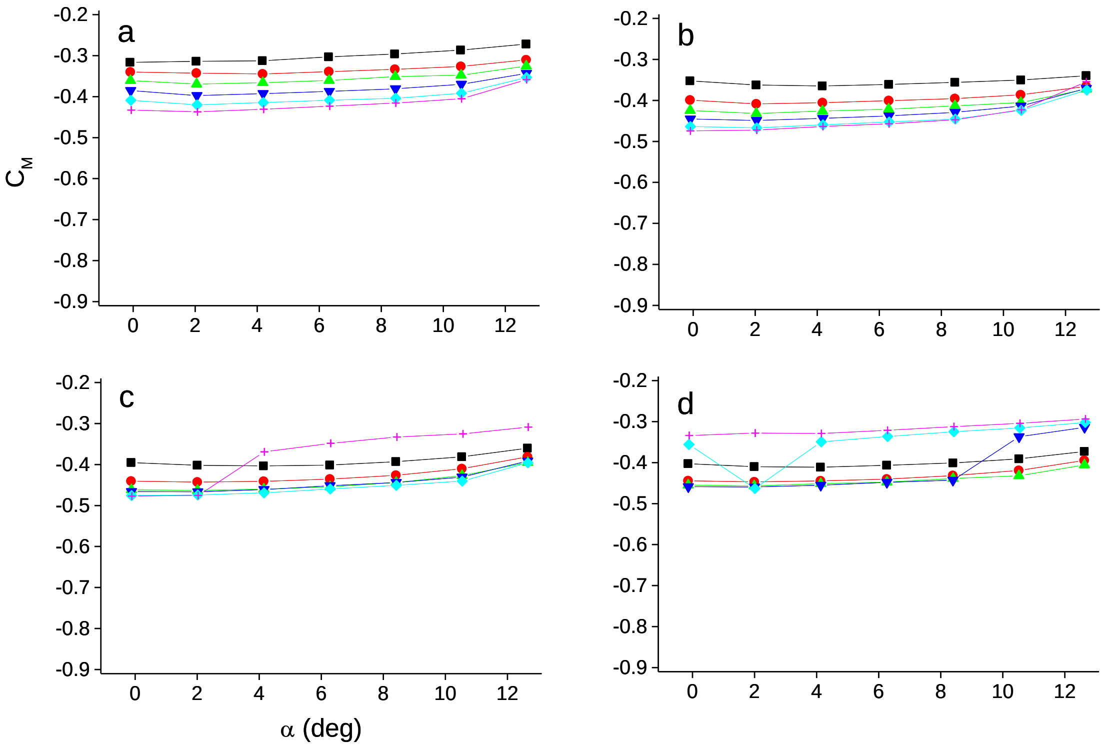

***Figure 9.6.*** *Variation of* $C_M$ *with* $\alpha$ *(*$Re_c = 6.7 \cdot 10^5$*):* $y/c$ *= 0 (a), 0.5% (b), 1.0% (c), and 1.5% (d).* $\delta$ *= 25° (■), 30° (●), 33° (▲), 36° (▼), 39° (◆), 42°(+).*

corresponding three-dimensional $C_L$ values (cf. Figure 9.4) because the flap occupies only a limited portion of the span. The variation of $C_l$ and $C_L$ with $y/c$, $\delta$ and $\alpha$ follows nearly identical trends, indicating that either measurement would be suitable for assessing changes in the aerodynamic characteristics of the airfoil. The three-dimensional aerodynamic quantities (e.g., $C_L$, $C_D$, $C_M$ etc.) are measured directly by the load cells and account for effects of spanwise variation in the flow near the outer span of the flap. Therefore, three-dimensional quantities are used in the subsequent assessments of aerodynamic performance.

The suction peak near the leading edge of the flap and increased suction downstream (cf. Figure 9.2) induce a nose-down pitching moment, as shown by the variation of pitching moment $C_M$ (about $c/4$) in Figure 9.6. The flap creates a nose-down pitching moment ($C_M \sim -0.3$–$-0.4$ at $y/c = 0$; Figure 9.6a) which becomes more nose-

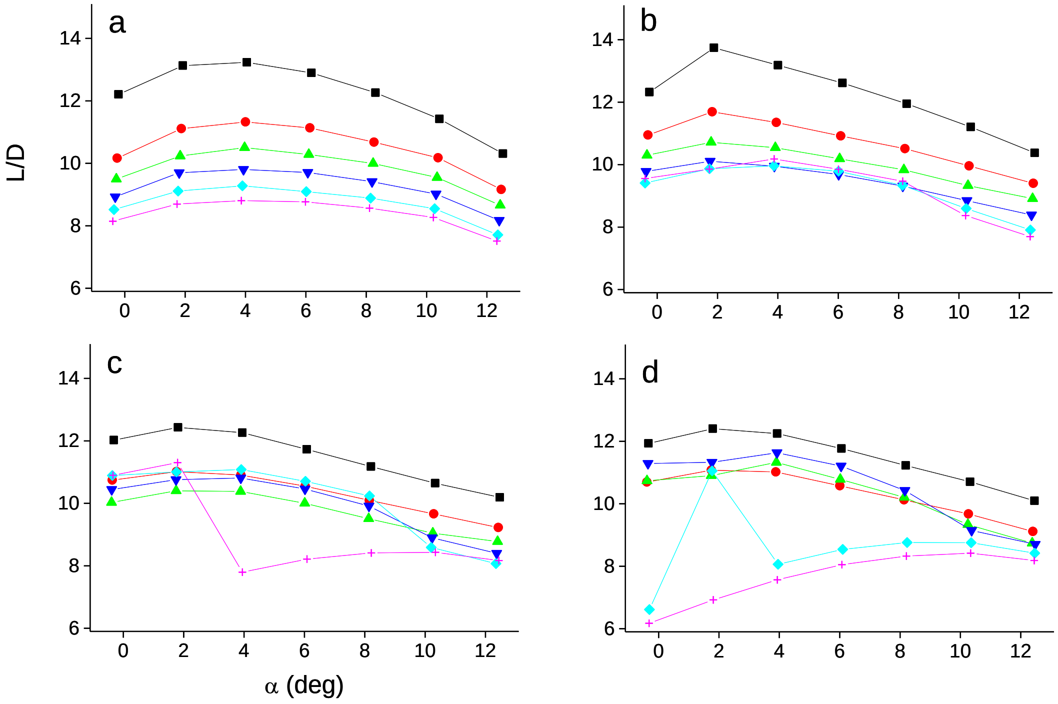

***Figure 9.7.*** *Variation of L/D with* $\alpha$ *(*$Re_c$ *=* $6.7{\cdot}10^5$*):* $y/c$ *= (a) 0, (b) 0.5%, (c) 1.0%, (d) 1.5%.* $\delta$ *= 25° (■), 30° (●), 33° (▲), 36° (▼), 39° (◆), 42°(+).*

down with increasing $\delta$. As $y/c$ is increased, $C_M$ becomes more nose-down (Figures 9.6b-d) as suction increases on the flap. Similarly, for conditions for which the flap becomes fully stalled (cove separation), the lift decreases (cf. Figure 9.4), and suction on the flap is reduced (cf. Figure 9.2) the pitching moment becomes less nose-down.

The corresponding lift-to-drag ratios (*L/D)* are shown in Figure 9.7. For $y/c = 0$ (Figure 9.7a) the maximum *L/D* occurs at $\alpha = 4°$ and decreases with increasing $\delta$ (from 13 at $\delta = 25°$ to 8.5 at $\delta = 42°$). Figure 9.7b shows that using a gap of $y/c = 0.5\%$ increases *L/D*, particularly for $\delta \geq 36°$. For $\delta = 42°$, *L/D* increases ~20% (for $\alpha < 10°$) from $y/c = 0$ to 0.5%, while the corresponding lift increases by less than 10%, indicating a reduction in drag. For larger gaps (Figures 9.7c-d) *L/D* decreases, particularly for conditions where the flow separates in the cove, resulting in reduced lift and increased drag. Because it represents a combination of high lift and high *L/D*, the condition of $\delta = 42°$ and $\gamma/c = 0.5\%$ ($C_L = 2.22$) is selected as a reference to which the aerodynamic performance of the active flow control-enhanced airfoil is compared in §9.2.

### *9.2. High-Lift Performance Improvement using Aerodynamic Flow Control*

As discussed in §9.1, the performance a high-lift system with a Fowler-type flap can be enhanced by the formation of a jet through a cross-stream gap between the flap and the main element. The presence of the flow through the gap can mitigate the effects of the adverse pressure gradient that is associated with flow turning over the flap. The interaction of the cove jet with the main element boundary layer and flap boundary layer is governed by the cross stream scale of the gap that also affects the jet momentum, and, under some conditions, can result in enhanced flow attachment on the flap and increased lift. However, because the jet is driven by the flow over the pressure side of the airfoil, its momentum diminishes when the width of the gap is reduced. The present work demonstrates that the functionality of the cove jet can be enhanced and perhaps even replaced by distributed actuation using spanwise arrays of fluidic oscillators near the leading edge of the flap to achieve flow attachment with comparable or greater streamwise extent than an optimized Fowler flap by engendering streamwise vorticity concentrations within in the boundary layer upstream of the "natural" separation point. *An important objective of the present investigations is to demonstrate that the presence of the fluidic actuation can replace the Fowler gap altogether and enable the use of a simple flap configuration that avoids the mechanical complexity of a multi-element (e.g. Fowler flap) configuration*.

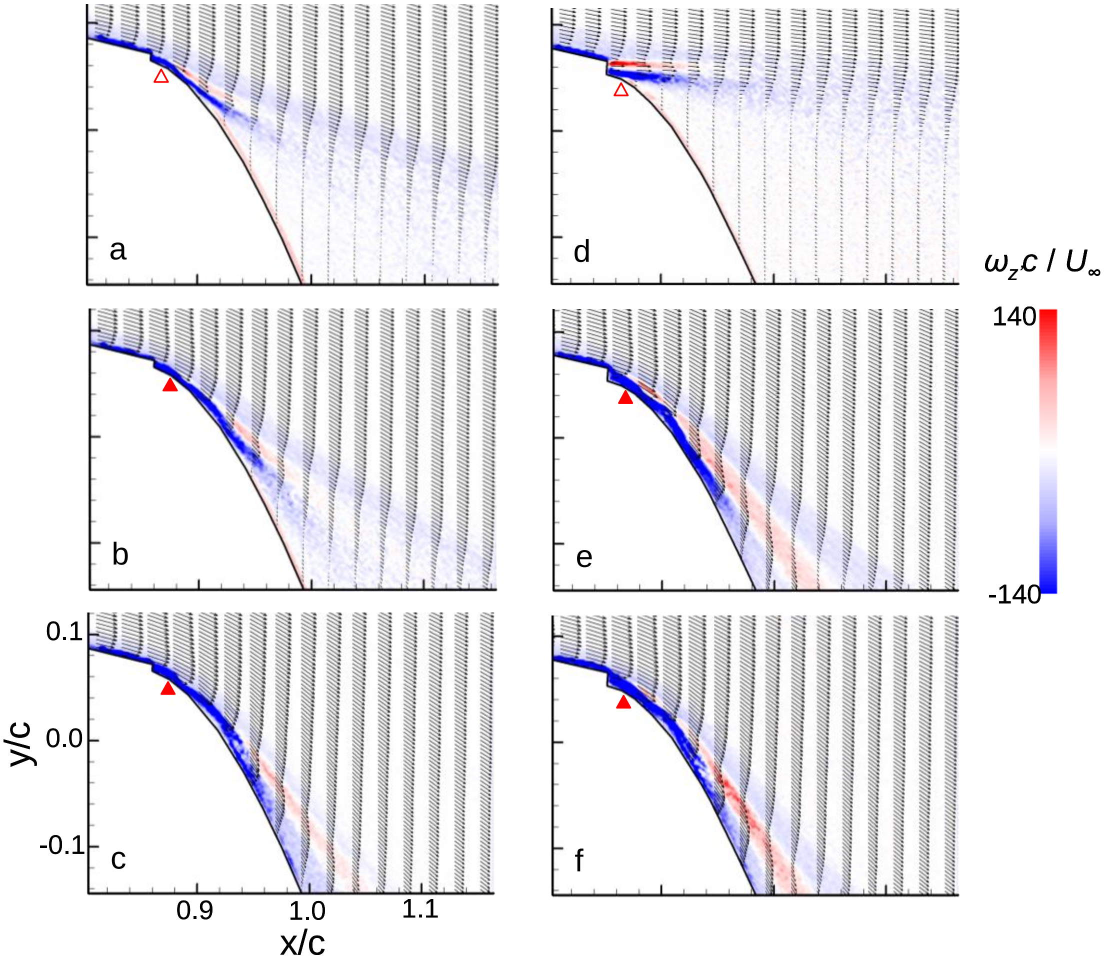

***Figure 9.8.*** *Color raster plots of the spanwise vorticity and cross stream distributions of velocity vectors in the flow field downstream of the flap cove ($\delta = 51°$, $\alpha = 4°$, $Re_c = 6.7 \cdot 10^5$) in the presence of actuation for $\gamma/c = 0$ [$C_\mu = 0$ (a), 0.5% (b), and 1.3% (c)], and $\gamma/c = 0.5\%$ [$C_\mu = 0$ (d), 0.5% (e), and 1.3% (f)].*

Based on the measurements of the separation locations for a range of flap angles and cross-stream gap settings (cf. Figure 9.3) a suitable location was identified for installation of the fluidic actuators on the suction surface, as shown in Figure 2.3b. The spanwise actuator array is located $0.08c_f$ downstream of the leading edge of the flap across nearly the entire span of the flap. In most of the investigations reported in this section, the (spanwise) actuation wavelength (i.e. the spacing between jets) is $\lambda/c = 0.015$. As noted in §2.2, the jet actuators oscillate in the spanwise plane at a nominal frequency of 6 kHz with a maximum momentum coefficient $C_\mu$ of 1.9% at $Re_c = 6.7 \cdot 10^5$. The jet orifices are recessed into the airfoil surface to minimize losses associated with their presence.

The effect of the actuation is demonstrated in a sequence of PIV measurements (with a camera resolution of 109 μm/pixel) of the flow field in the vicinity of the juncture between the flap and the main element ($\delta = 51°$), measured at midspan ($z = 0$) in the absence of a cross-stream gap ($\gamma/c = 0$; Figures 9.8a-c) and presence of a cross-stream gap ($\gamma/c = 0.5\%$, Figures 9.8d-f). In the absence of the gap when the actuators are inactive ($C_\mu = 0$, Figure 9.8a), the vorticity layer from the main element boundary layer curves over the flap juncture and separates near $0.1c_f$. The vorticity layer is bifurcated by a weak leakage jet through the small (O[$0.001c$]) opening between the flap and main element that is marked by a thin layer of CCW vorticity (from the upper edge). The separated domain is marked by recirculating flow that induces the formation of CCW vorticity near the surface of the flap.

The presence of actuation ($C_\mu = 0.5\%$, Figure 9.8b) causes the flow to turn toward the flap surface and accelerates the upstream flow over the main element, moving separation downstream toward the middle of the flap ($0.4c_f$). Actuation leads to the formation of spanwise-periodic concentrations of streamwise vorticity between actuator jets that are accompanied by low pressure domains near the surface, and in effect, a "virtual" change in the shape of the surface (e.g., DeSalvo and Glezer 2011). Even in the presence of actuation, the alternating CW/CCW/CW vorticity layers near the surface remain apparent indicating that the jets primarily affect the inner boundary layer close to the surface. The downward turning of the flow and upstream acceleration are more

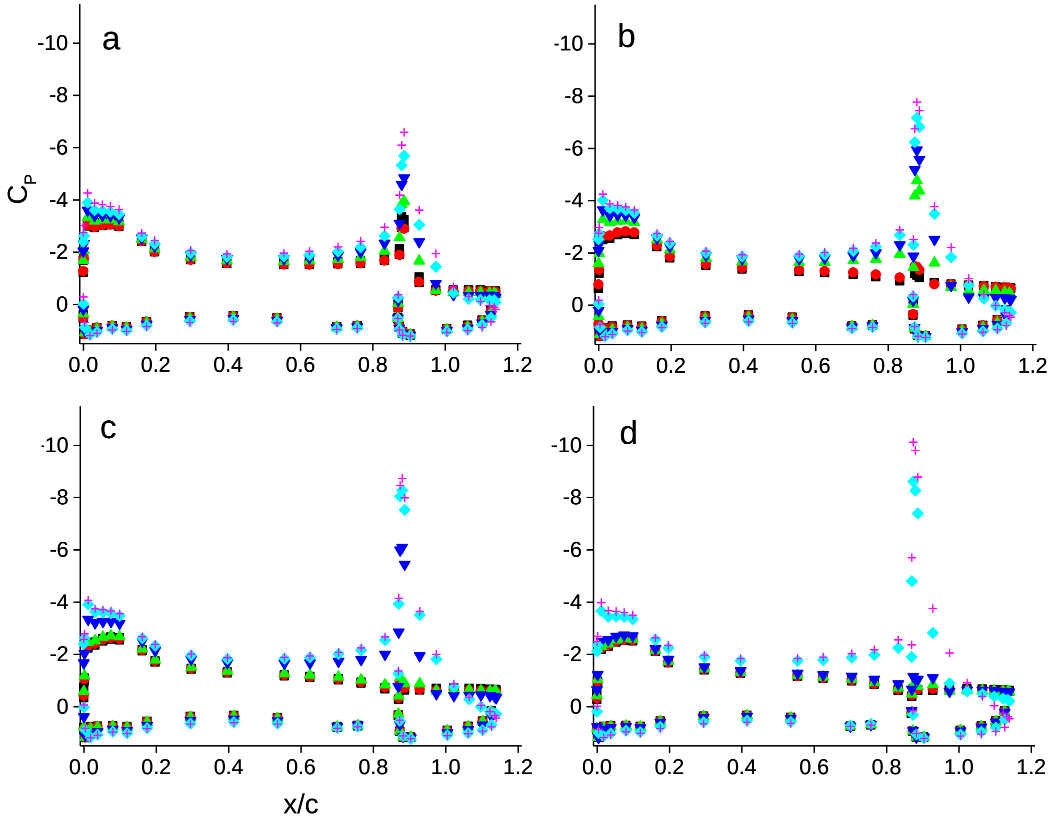

***Figure 9.9.*** *Pressure distributions around the airfoil with actuation ($\delta = 51°$, $\alpha = 4°$, $Re_c = 6.7\cdot 10^5$): $\gamma/c = 0$ (a), 0.5% (b), 1.0% (c), 1.5% (d): $C_\mu = 0$ (■), 0.05% (●), 0.2% (▲), 0.5% (▼), 0.8% (◆), and 1.3% (+).*

pronounced when $C_\mu = 1.3\%$ (Figure 9.8c) where the *flow attachment is extended through the trailing edge of the flap* indicating that the cross-section of the flap could be optimized for improved performance in the presence of actuation. It is remarkable that when the flow becomes fully attached to the flap, the traces of the CCW vorticity layer from the leakage flow through the opening between the flap and the main element remain present indicating that the leakage flow may be merely a passive attendant in the attachment process.

In the presence of a cross-stream gap ($\gamma/c = 0.5\%$, Figure 9.8d), a cove jet forms and the flow separates at the cove (cf., Figures 9.1a-b), and mixes rapidly with the cross flow. With actuation ($C_\mu = 0.5\%$, Figure 9.8e), the separation is suppressed nearly entirely, and the flow is somewhat better attached than in the absence of the gap (Figure 9.8b). The improved attachment is characterized by a stronger CW vorticity layer near the flap surface and a stronger CCW vorticity layer (from the upper edge of the cove jet). When the strength of the actuation is increased ($C_\mu = 1.3\%$, Figure 9.8f) attachment is enhanced and the outer flow is further vectored towards the surface of the flap. The similarity of the flow fields in the absence and presence of the gap (Figures 9.8c and f, with $C_\mu = 1.3\%$) indicates that fluidic actuation can lead to considerable simplification of the flap configuration, including elimination of the cross-stream gap, while still achieving comparable (or better) performance.

The effects of the strength of the actuation (in terms of $C_\mu$) on the pressure distribution over the airfoil across the range of cove gaps are shown in Figure 9.9 ($\delta = 51°$ and $Re_c = 6.7 \cdot 10^5$). For $\gamma/c = 0$ (Figure 9.9a) in the absence of actuation a suction peak forms near the flap cove ($x/c = 0.9$) and an adverse pressure gradient is present along a small portion of the suction surface until the flow separates near $x/c = 1.0$. The suction peak strength and extent of flow attachment increase monotonically with $C_\mu$. For $C_\mu = 1.3\%$, the suction peak reaches $C_p = -6.6$ and an adverse pressure gradient persists as far downstream as the trailing edge. Concomitantly, the actuation leads to increased suction over the main element as far upstream as the leading edge, leading to an increase in lift. With a cross-stream gap of $\gamma/c = 0.5\%$ (Figure 9.9b) a suction peak does not form at the cove for $C_\mu < 0.2\%$ and the flow separates at the cove. The increased extent of separation also diminishes the main body suction. For $C_\mu \geq 0.2\%$, actuation forms a suction peak that leads to improved flow attachment. Increasing the cross-stream

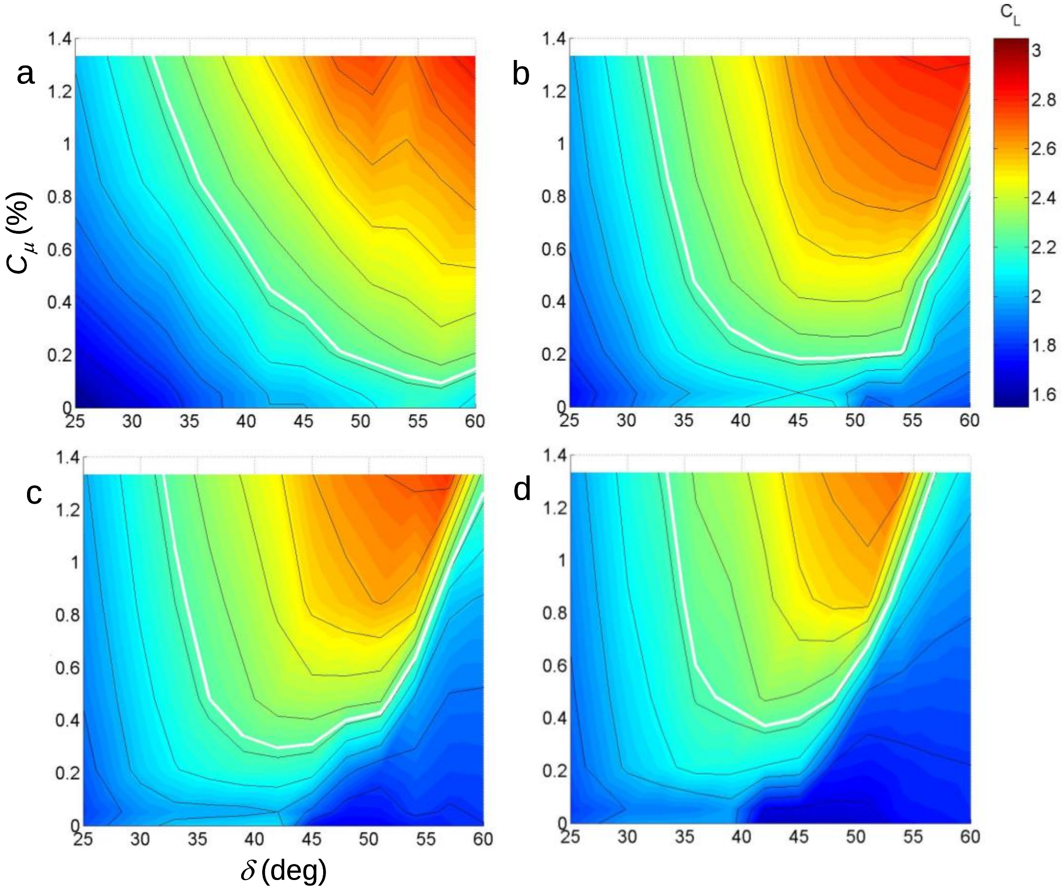

***Figure 9.10.*** *Contour plot showing variation of* $C_L$ *with* $C_{\mu}$ *and* $\delta$ *in the presence of actuation (*$\alpha = 4°$*,* $Re_c = 6.7 \cdot 10^5$*):* $\gamma/c = 0$ *(a), 0.5% (b), 1.0% (c), 1.5% (d). Contour increment is* $\Delta C_L = 0.1$*. White contour (*$C_L = 2.22$*) denotes* $C_L$ *of the reference baseline configuration (*$\delta = 42°$*).*

gap to $\gamma/c = 1.0\%$ (Figure 9.8c) requires $C_{\mu} \geq 0.5\%$ to overcome the adverse effects of the oversize gap, and for $\gamma/c = 1.5\%$ (Figure 9.9d) flow attachment only occurs for $C_{\mu} \geq 0.85\%$. Although the increased gap results in a slight reduction in suction over both the flap and the main element, it is noteworthy that the magnitude of the suction peak near the cove increases with gap width. The suction peaks for $C_{\mu} = 1.3\%$ reach values of $C_p = -6.6$, $-7.8$, $-8.7$ and $-10.1$ for $\gamma/c = 0$, 0.5%, 1.0% and 1.5%, respectively, suggesting that the actuation is capable of locally turning the cove jet toward the flap surface, and while the vectoring effect increases with jet width, for larger cross-stream gaps it is insufficient to interact with and turn the boundary layer of the main element.

The effect of actuation on lift is shown in color raster plots of $C_L$ with respect to $\delta$ and $C_\mu$ for $\gamma/c = 0$, 0.5%, 1.0% and 1.5% (Figures 9.10a-d, respectively). In these plots, a given contour indicates all combinations of $C_\mu$ and $\delta$ that yield a specific $C_L$ (note that $C_L$ for the baseline airfoil at $\alpha = 4^o$, $\delta = 42^o$ and $\gamma/c = 0.5\%$ is indicated for reference by a white contour). The lowest point on each $C_L$ contour corresponds to the minimum level of $C_\mu$ required to achieve $C_L$ and the corresponding flap deflection. For a given value of $\delta$, $C_L$ always increases monotonically with $C_\mu$. In the absence of a gap (Figure 9.10a) only a subset of contours (for $C_L < 2.5$) exhibits a minimum $C_\mu$ within the range of flap angles that was investigated. Within the range of measurements, the maximum lift $C_L = 2.83$ is achieved for $C_\mu = 1.3\%$ and $\delta = 60°$, with a corresponding lift increment of $\Delta C_L = 0.61$ relative to the baseline reference condition. As the gap is increased, the contours exhibit a more clearly defined minimum required $C_\mu$ and the maximum lift attained at high flap angles decreases appreciably. At $\gamma/c = 0.5\%$ (Figure 9.10b), the deflection for which minimum $C_\mu$ is required increases from $\delta = 45°$ for $C_L = 2.1$ ($C_\mu = 0.1\%$) to $\delta = 57°$ for $C_L = 2.7$ ($C_\mu = 0.9\%$), and the maximum measured lift is $C_L = 2.83$ at $\delta = 57°$ and $C_\mu = 1.3\%$ (equal to the maximum lift for $\gamma/c = 0$). Similar variation occurs for larger gaps (Figures 9.10c-d), although the maximum lift is lower and the $C_\mu$ required for a given $C_L$ is minimized at a lower deflection.

It is instructive to consider the variation of $C_L$ with flap angle for fixed levels of $C_\mu$ (Figure 9.11). For the baseline airfoil (Figure 9.11a), lift increases monotonically with $\delta$ before decreasing due to separation at the cove. As $\gamma/c$ is increased to 0.5%, the onset of cove separation occurs at $\delta = 48°$; however, for deflections below this level lift is

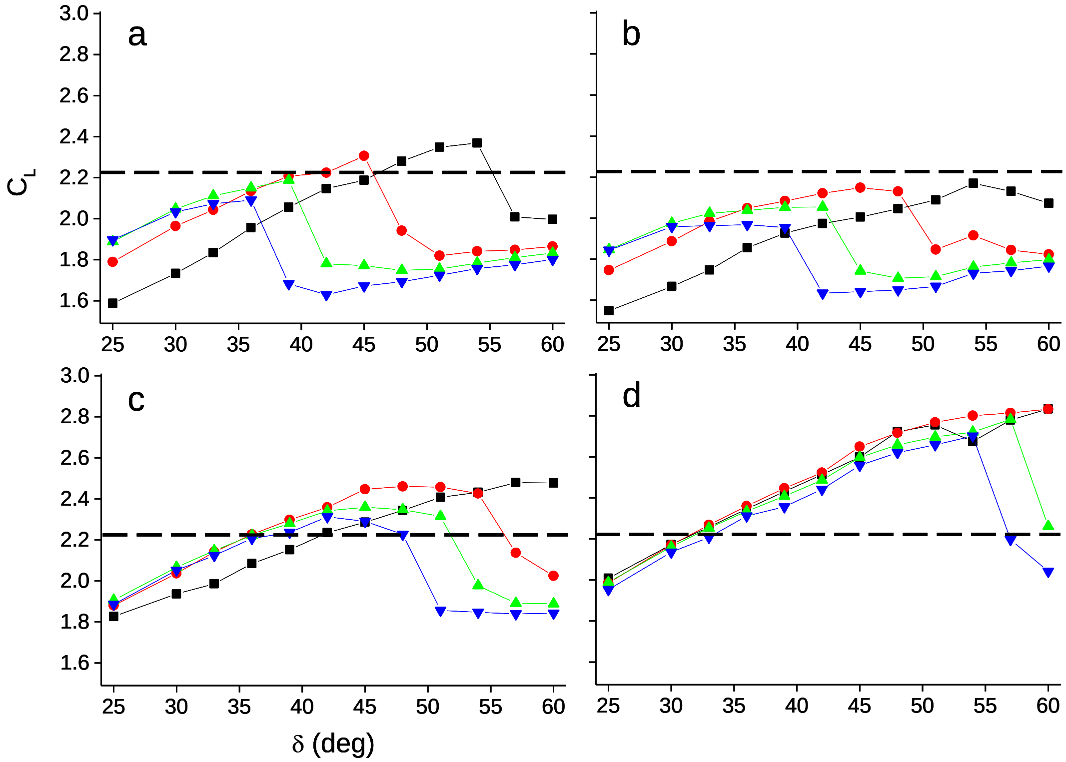

***Figure 9.11.*** *Variation of $C_L$ with flap deflection $\delta$ for baseline airfoil (a), airfoil with actuator installed and $C_\mu = 0$ (b), 0.5% (c), and 1.3% (d). Dashed line denotes reference $C_L$ (baseline, $\delta = 42°$, $\gamma/c = 0.5\%$). Flap-to-main body gap $\gamma/c = 0$ (■), 0.5% (●), 1.0% (▲), 1.5% (▼).*

increased by $\Delta C_L \sim 0.1\text{-}0.2$. Lift loss occurs at lower deflections ($\delta = 42°$ and $\delta = 39°$, respectively, for $\gamma/c = 1.0\%$ and 1.5%) with little further lift increase below these deflection levels. Also noteworthy is that for deflections above the onset of lift loss, lift decreases with $\gamma/c$. With the actuator installed and in the absence of actuation (Figure 9.11b) $C_L$ varies with $\delta$ and $\gamma/c$ in a similar manner to the baseline airfoil, though with a small ($\Delta C_L \sim 0.1$) decrease in lift. As $C_\mu$ increases to 0.5% (Figure 9.11c), cove separation occurs at larger deflections and $C_L$ increases, varying relatively little with cross-stream gap (except for $\gamma/c = 0$) indicating a trend in which for a given $\delta$, as long as the flow remains attached to the flap $C_L$ is insensitive to $\gamma/c$. This trend becomes more apparent for $C_\mu = 1.3\%$ (Figure 9.11d) where $C_L$ increases up to a maximum of $C_L = 2.83$ ($\gamma/c = 0.5\%$, $\delta = 60°$; $\Delta C_L = 0.61$) and has nearly the same value for $\gamma/c = 0$. There is

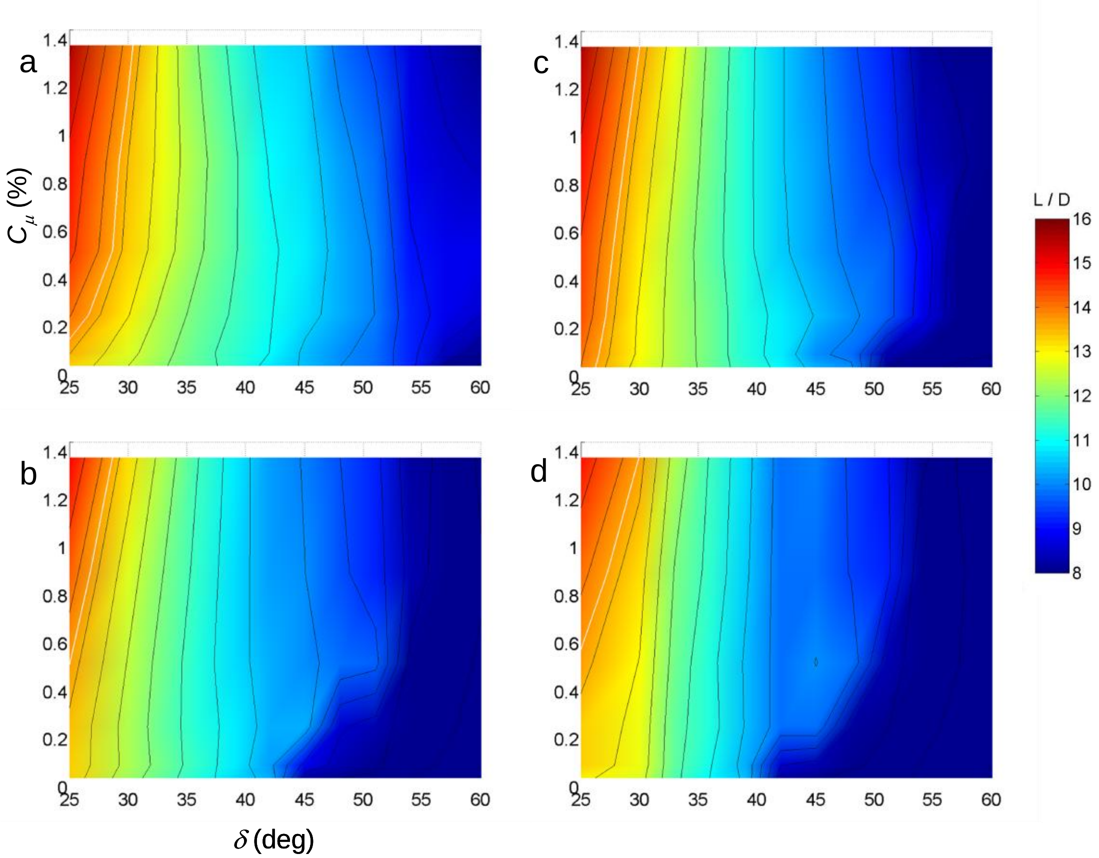

*Figure 9.12.* *Contour plot showing variation of L/D with $C_\mu$ and $\delta$ in the presence of actuation ($\alpha = 4°$, $Re_c = 6.7 \cdot 10^5$): $\gamma/c = 0$ (a), 0.5% (b), 1.0% (c), 1.5% (d). Contour increment is $\Delta(L/D) = 0.5$. White Contour ($L/D = 13.7$) denotes L/D of the reference baseline configuration ($\delta = 42°$).*

little variation with $\gamma/c$ for a given $\delta$ (for $\delta < 55°$) indicating that for a given $\delta$, the same aerodynamic performance can be attained in the absence of a gap and potentially with a simple flap.

It is also instructive to consider the variations of the lift-to-drag ratio *L/D* with respect to $\delta$ and $C_\mu$ for the various cross-stream gaps as shown in Figure 9.12 using contour plots similar to Figure 9.10. Perhaps the most important feature of these data is that there is little variation in *L/D* with increasing $C_\mu$, indicating that the increase in lift due to actuation (cf. Figure 9.10) is also accompanied by an increase in lift-induced drag, particularly for larger flap deflections. It is noteworthy that for smaller cross-stream

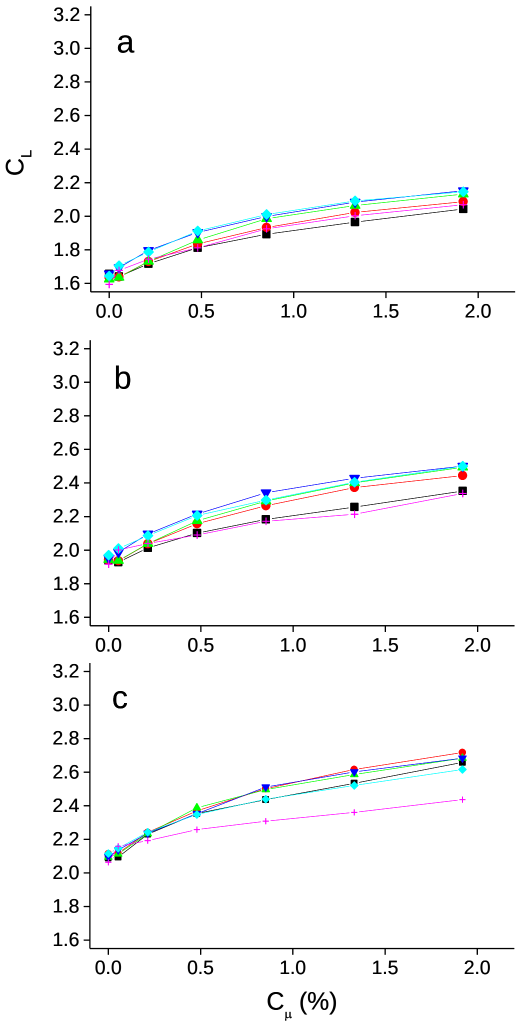

***Figure 9.13.*** *Effect of the actuation spanwise wavelength* $\lambda$ *on* $C_L$ *(*$\gamma/c = 0$, $\alpha = 4°$, $Re_c = 6.7\cdot10^5$*):* $\delta = 30°$ *(a), 42° (b), 54° (c).* $\lambda/c = 0.015$ *(■), 0.020 (●), 0.026 (▲), 0.035 (▼), 0.046 (◆), 0.079 (+).*

gaps, levels of *L*/*D* that are considerably higher than the reference level can be attained. For example, at $\gamma/c = 0$ the maximum *L*/*D* is attained is 15.6 (with $C_L = 2.01$) at $\delta = 25^o$ (which is more appropriate for takeoff conditions) and $C_\mu = 1.3\%$ (compared to *L*/*D* = 16.1 and $C_L = 1.59$ at the same deflection for the baseline airfoil).

The investigation also considered the effects of the spanwise actuation wavelength $\lambda$ on the aerodynamic performance in the absence of the cross-stream gap. In these measurements, $\lambda/c$ was increased from 0.015 (as in Figures 9.8-9.12) to 0.079 (a factor of 5.2) by reducing the number of active jets, while adjusting the mass flow rate through the actuators to maintain the same $C_\mu$ between the different configurations (in these measurements the maximum $C_\mu$ was increased to 1.9%). Figures 9.13a-c show the variation of $C_L$ with $C_\mu$ for $\delta = 30°$, 42° and 54°, respectively. For $\delta = 30°$ (Figure 9.13a), $C_L$ increases with $\lambda/c$ up to a maximum at $\lambda/c = 0.035$ ($\Delta C_L \sim 0.2$) before decreasing at larger $\lambda/c$ as the jets become more sparsely spaced across the span of the flap. A similar trend is present for $\delta = 42°$ (Figure 9.13b), with a slightly larger increment ($\Delta C_L \sim 0.3$) between $\lambda/c = 0.015$ and the maximum at $\lambda/c = 0.035$. For $\delta = 54°$ (Figure 9.13c), there is little difference in $C_L$ as the spanwise wavelength is varied across the range $0.015 \leq \lambda/c \leq 0.035$ (maximum lift occurs for $\lambda/c = 0.020$), whereas for larger $\lambda/c$ the lift increment decreases (particularly for $\lambda/c = 0.079$, where the actuators become less effective at increasing lift). The data in Figures 9.13a-c indicate that the aerodynamic performance of the actuation varies relatively little with spanwise wavelength as long as the same $C_\mu$ is maintained. In fact, the data suggest that for larger spanwise wavelengths, comparable performance may be achieved by increasing $C_\mu$. This is noteworthy because even though $C_\mu$ may increase, the actuation mass flow decreases significantly for larger spanwise wavelengths. For example, for the same $C_\mu$, increasing $\lambda/c$ from 0.015 to 0.079 decreases the mass flow rate by a factor of 2.3.

To investigate the actuation effectiveness at large $\lambda/c$, the flow field downstream of the cove for $\delta = 54°$ and $\lambda/c = 0.079$ was measured using PIV (with a camera resolution of 109 mm/pixel) in 17 equally-spaced cross stream planes spanning $\pm 0.5\lambda$ around the center of an active actuator (Figure 9.14). Figures 9.14b and e show the flow

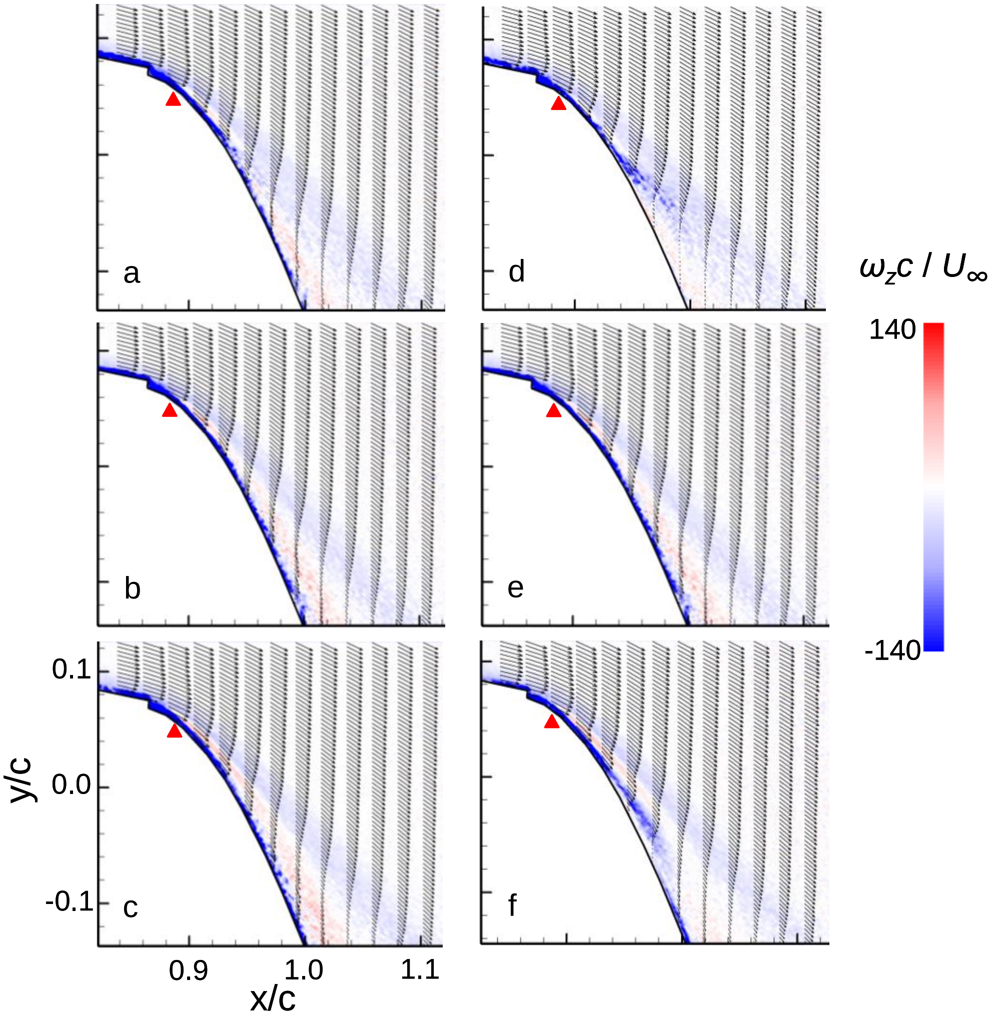

***Figure 9.14.*** *Color raster plots of the spanwise vorticity and cross stream distributions of velocity vectors in the flow field downstream of the flap cove ($\delta$ = 54°, $\alpha$ = 4°, $Re_c = 6.7 \cdot 10^5$) in the presence of fluidic actuation with $\lambda/c$ = 0.079: z = −0.16$\lambda$ (a), 0 (b), +0.16$\lambda$ (c), and z = −0.5$\lambda$ (d), 0 (e), +0.5$\lambda$ (f).*

field on the actuator centerline ($z$ = 0) where the flow is fully attached to the flap (similar to $\lambda/c$ = 0.015, cf. Figure 9.8c). The measurements in Figures 9.14a and c are taken in the cross stream planes $z$ = −0.16$\lambda$ and +0.16$\lambda$, respectively (symmetric about the centerline) and show relatively little difference compared to the flow downstream of the centerline of the actuator. However, the measurements farther from the centerline (Figures 9.14d and f, $z$ = −0.5$\lambda$ and +0.5$\lambda$, respectively) show some separation at $z$ = −0.5$\lambda$ ($x/c$ = 0.95) but not at $z$ = +0.5$\lambda$. This asymmetry indicates that the magnitude of the actuation at this spanwise wavelength is probably marginal as is evidenced by the fact that at the shorter wavelength ($\lambda/c = 0.046$, Figure 9.13), the aerodynamic performance suggests that the flow is nearly fully attached. As noted above, the small reduction in aerodynamic performance is attained with a significantly smaller mass flow coefficient and can probably be improved at higher $C_\mu$.

# CHAPTER 10
# CONCLUSIONS

## *10.1. Summary of Findings: Aerodynamic Flow Control in the Absence of Large-Scale Flow Separation*

In this part of the dissertation it is shown how the global aerodynamic characteristics of the flow over a lifting surface that is predominantly attached (i.e. an airfoil in cruise conditions) can be effectively altered using active flow control. Control is implemented using hybrid synthetic jet-based actuators consisting of an obstruction having a characteristic height of 0.01*c* with an integral synthetic jet actuator having a momentum coefficient of $C_\mu \sim 10^{-3}$. Downstream of the obstruction a concentration of trapped vorticity forms (the size of which scales with the height of the obstruction) and the synthetic jet is used to regulate the vorticity flux within the upstream boundary layer, thereby manipulating the strength and size of the vorticity concentration in a manner leading to global changes in the flow around the entire lifting surface. Measurements were made at $Re_c = 6.7 \cdot 10^5$, $1.0 \cdot 10^6$, and $1.3 \cdot 10^6$ with jet momentum coefficients up to $C_\mu = 2 \cdot 10^{-3}$ and reduced frequency $St_{act} \sim 30$.

Aerodynamic control by creation and manipulation of trapped vorticity has been demonstrated in this dissertation using three different configurations. In one configuration, where the hybrid actuator was placed on the pressure surface near 0.25*c* (to reduce any changes in pitching moment that may occur due to the presence and operation of the actuator), the manipulation of the vorticity concentration alters the boundary layer characteristics in a manner leading to a reduction in pressure drag with no significant effect on skin friction drag. When a second hybrid actuator is positioned on the pressure surface near the trailing edge, the trapped vortex that forms downstream of the obstruction interacts with the flow around the trailing edge and manipulation of the trapped vortex modifies the Kutta condition, altering the flow on both the suction and pressure surfaces of the airfoil and leading to a change in pitching moment. It is also demonstrated how the required actuation power to the trailing edge actuator can be reduced through pulse modulation of the actuation waveform at a frequency corresponding to the unstable frequency of the near wake of the airfoil. A configuration with hybrid actuators on both the pressure and suction surfaces near the trailing edge is also tested, enabling bi-directional control of the pitching moment.

The presence of the hybrid actuator on the pressure surface near the leading edge and the formation of the trapped vorticity concentration (located near 0.25*c*), i.e. a locally separated flow, immediately downstream of the obstruction lead to a local acceleration of the flow over the surface of the airfoil upstream of the obstruction, as indicated by static pressure distributions and high-resolution PIV measurements near the airfoil surface. Operation of the actuator creates an intense low-pressure domain that re-orients the flow toward the wall, reduces the size of the trapped vortex and resulting in pressure recovery on the downstream-facing segment of the hybrid actuator and additional flow acceleration upstream of the jet. As a result, the thickness of the airfoil wake and the boundary layer near the trailing edge is reduced and there is a substantial reduction in drag with minimal penalty in lift.

These changes in drag due to actuation on the pressure surface near the leading edge have been verified using multiple distinct measurement techniques. A reduction in pressure drag $C_{dp}$ of ~50% was measured by integration of the pressure distribution around the airfoil. An estimate of the skin friction drag $C_{df}$ was computed from high-resolution PIV measurements of the velocity distribution in the airfoil boundary layer and showed that changes in skin friction on the airfoil in the presence of actuation are negligible, and occur mainly due to the greater streamwise extent of a laminar boundary layer along the pressure surface of the baseline airfoil (i.e. in the absence of the hybrid actuator). These differences are expected to diminish at higher $Re_c$ where the boundary layer turbulent transition location is located farther upstream. When the changes in pressure drag and skin friction are combined, the estimated changes in total drag (relative to the baseline airfoil) are $\Delta C_d = 0.0022$ with an inactive actuator and $-0.0049$ in the presence of jet actuation. These estimates were confirmed by using high-resolution PIV to measure the momentum flux in the near wake of the airfoil for the actuated and unactuated configurations. The difference in *total* drag $\Delta C_d$ between the actuated and unactuated configurations was computed from these measurements, showing a difference in drag of $\Delta C_d = 0.0067$, in close agreement with the estimate from pressure and wall friction measurements of $\Delta C_d = 0.0071$. As a result, it is shown that for $Re_c = 6.7 \cdot 10^5$ the actuation leads to a 29% reduction of the total drag relative to the baseline airfoil and an increase of 27% in $l/d$ from 28.3 to 35.8. It is noteworthy that the magnitude of the momentum increase in the airfoil wake, as measured by the change in drag coefficient, of $\Delta C_d = 0.0071$ is significantly greater than the magnitude of the momentum from the actuator of $C_\mu = 0.0021$ (note that both $C_d$ and $C_\mu$ are scaled according to the free stream dynamic pressure and airfoil area).

Assessing the sensitivity of the aerodynamic performance modification to changes in the jet momentum coefficient $C_\mu$ indicates that the lift and pressure drag can be varied *continuously* with $C_\mu$. While the decrease in $C_l$ due to the actuation is minimal (less than 10%, regardless of $C_\mu$) the corresponding variations in $C_{dp}$ are far greater. For $Re_c = 6.7 \cdot 10^5$, $1.0 \cdot 10^6$, and $1.3 \cdot 10^6$, actuation at the maximum attainable $C_\mu$ of $2.05 \cdot 10^{-3}$, $0.91 \cdot 10^{-3}$ and $0.51 \cdot 10^{-3}$, respectively results in pressure drag reductions of 55%, 40%, and 45%, respectively, relative to the baseline airfoil.

In order to achieve changes in pitching moment using active flow control, a second hybrid actuator was installed on the pressure surface near the trailing edge. By using the synthetic jet to manipulate the trapped vortex (having characteristic height $0.01c$ and located $\sim 0.02c$ upstream of the trailing edge) that forms on the downstream edge of the obstruction, the airfoil Kutta condition can be manipulated in a manner leading to changes in the pressure distribution on both the suction and pressure surfaces. In particular, the increase in pressure downstream of the actuator, i.e. at the trailing edge, extends around the trailing edge to the suction surface. As a result, there is a corresponding change in spanwise pitching moment (due to the changes in pressure near the trailing edge) in addition to a reduction in pressure drag. The trailing edge actuator is operated in conjunction with the actuator near $0.25c$, and it is shown that the effects of the two actuators are mutually independent, and that the resulting aerodynamic changes that occur due to each individual actuator are effectively superposed.

It was also shown how varying the (time-averaged) jet momentum coefficient of the hybrid actuator on the pressure surface near the trailing edge using a pulse-modulated waveform (e.g. Amitay and Glezer 2002) at a frequency that couples to an instability of the near wake enables aerodynamic changes to be achieved with substantially lower power input. Phase-locked PIV measurements of time-varying circulation and vorticity flux under pulse modulated actuation have shown that initiation and termination of continuous or pulse modulated actuation lead to changes in the circulation on the timescale of 1-2$\tau$ along with more rapid variations on the timescale of 0.15$\tau$, corresponding to a reduced frequency of $St = 6.7$ which is the characteristic frequency of the unstable wake. By pulse-modulating the actuator driving waveform at the same frequency ($St = 6.7$) with a duty cycle of 0.25 the drag is reduced to the same level as with continuous actuation at full power, with only a minimal lift penalty in both cases. Additional drag reduction occurs when the actuator is operated at $St = 6.7$ and duty cycle 0.9.

Alternating pulse modulated actuation using two trailing-edge-mounted actuators enables proportional *bi-directional* control of the pitching moment relative to some desirable trim condition where the transitory effects of actuator activation and deactivation are exploited to maximize the control authority over a broad range of angles of attack. Because the variation in the aerodynamic characteristics depend nonlinearly on $C_\mu$ it is useful to operate the actuator using pulse width modulation with variable duty cycle and modulation frequency but fixed (unmodulated) $C_\mu$ to achieve the desired controllable variation in aerodynamic performance. An almost linear variation in pitching moment with modulation frequency has been demonstrated over a nominal range of $1.28|C_{m0}|$ (at $\alpha = 4^\circ$), with corresponding linear changes in lift. The drag reduction achieved by operating either actuator enables $C_m$ to be varied over nearly the same range of levels as with continuous actuation but with lower drag penalty.

The flow fields in the vicinity of an actuator undergoing initiation and termination of actuation have been studied to identify the mechanism behind the observed aerodynamic changes. Initiation of actuation creates a disruption in the separated vorticity layer at the actuator orifice that causes a large vorticity concentration to be shed into the wake. The actuator generates pairs of vorticity concentrations of opposite sense which are subsequently advected downstream; the concentration of opposite sense to the boundary layer diminishes rapidly, while the other concentration remains attached to the wall before being shed into the wake downstream of the actuator. This causes the separation point along the wall to move downstream, reducing the extent of the recirculating flow domain near the actuator thus altering the aerodynamic characteristics of the entire airfoil. Deactivation of the actuator causes a vorticity cluster to be shed into the wake before a stable detached layer of vorticity is reestablished near the actuator orifice.

### *10.2. Summary of Findings: Aerodynamic Flow Control in the Presence of Large-Scale Flow Separation*

The flow over an aerodynamic surface containing large-scale domains of flow separation can be manipulated using active flow control in order to achieve a significant change in aerodynamic performance, as shown in Chapters 7-9 of the dissertation. This was demonstrated using an airfoil with a deployed high-lift system (containing both simple and Fowler flaps). In one series of experiments, the performance of an airfoil with a simple trailing-edge flap was improved using active flow control actuation consisting of a spanwise array of high-frequency fluidic oscillators issuing tangentially to the local surface near the leading edge of the flap. Actuation engenders concentrations of vorticity near the surface in a manner causing the “apparent” shape of the flap to be altered. A substantial increase in the extent of flow attachment along the flap occurs as a result, leading to increased suction over the suction surfaces of the flap and the main element and hence increased lift. A second series of experiments was conducted using the simple flap with an active flow control implementation consisting of a spanwise array of synthetic jet actuators in the same position and orientation as the fluidic oscillators. The increases in flow attachment extent, suction and lift are comparable to what were achieved using fluidic oscillators, though greater actuation power is required. It was also shown in these studies how actuation mitigates separation by inducing the formation of arrays of counter rotating streamwise vortices near the airfoil surface that enhance transport of high-speed fluid toward the surface. A third series of studies using an airfoil with a Fowler flap have shown how active flow control enables significantly higher lift to be achieved than optimization of a conventional high-lift system (i.e. with a Fowler-type flap), indicating that comparable or better high-lift performance can be attained using a simplified high-lift system that does not require a cross-stream gap (as with a Fowler-type flap) and can operate at larger flap deflections.

For the simple flap configuration, it was shown how flow control actuation having a maximum momentum coefficient of $C_\mu = 1.6\%$ can be employed to increase lift by a significant margin. In the absence of actuation, separation occurs near the juncture between the flap and the main element on the baseline airfoil. Actuation leads to the development of a suction peak near the shoulder, the strength of which increases with the actuation power level. This, in turn, leads to increased suction along the surface of the main element and increases in the extent of flow attachment along the flap, resulting in substantially higher $C_l$. In particular, actuation at $C_\mu = 1.6\%$ results in lift increases of $\Delta C_l = 0.78$ and 1.05 for flap deflections of $\delta = 20°$ and 40°, respectively, relative to the baseline airfoil. The increased extent of flow attachment also leads to reduced pressure drag at lower $C_l$. However, at higher $C_l$ the increase of lift-induced pressure drag due to increased $C_l$ becomes significant. Because the increased suction is located primarily on the aft portion of the airfoil, actuation also leads to a substantial nose-down pitching moment. The lift increment is sensitive to the inclination angle of the oscillating jet relative to the free stream. Optimal performance is observed at inclination angles between 26° and 37° above the local surface tangent. However, it is also shown that it is possible to achieve significant lift enhancement with jets oriented normally to the local surface at considerably lower $C_\mu$.

Experiments were also conducted using a synthetic-jet-based array of flow control actuators on the same simple flap configuration, with the actuator jets issuing from the juncture between the flap and main element and oriented downstream along the surface of the flap. Actuation results in increases in suction and lift (as with the configuration using fluidic oscillators); in particular, a lift increment of $\Delta C_l = 0.82$ was achieved at $Re_c = 3.3 \cdot 10^5$ and $\delta = 25°$ for $\alpha = 4°$ that is relatively invariant with $\alpha$. The effects of synthetic jet actuation are comparable to the effects of a similarly configured array of fluidic oscillator, though higher $C_\mu$ is required. By operating the jet actuators in spanwise-periodic patterns of variable wavelength and duty cycle, the actuator momentum required for a given lift increment can be reduced. At lift increments $\Delta C_l$ above 0.3, the highest $\Delta C_l$ for a given $C_\mu$ is achieved using a spanwise period of $0.035c < \lambda < 0.04c$ with a single active jet. At lower actuation power levels ($C_\mu < 0.15\%$)

lift increments of $\Delta C_l \sim 0.1\text{-}0.2$ are achievable and are relatively invariant with actuator spacing.

The 3-D flow field associated with the interaction of the actuation jets with the cross flow is investigated using high-resolution PIV measurements in the near field of the jet. These three-dimensional measurements enable extraction of spatial distributions of spanwise and streamwise vorticity concentrations. The interaction of the jet with the wall leads to the formation of counterrotating concentrations of streamwise vorticity on both sides of the jet, between which an upward flow (away from the surface) is induced. This results in the formation of a low pressure domain downstream of the orifice near the surface and moves higher-momentum flow from the flow above the surface toward the surface, promoting enhanced flow attachment that leads to increased lift. Pressure gradient measurements show that actuation introduces spanwise-periodic variations in the streamwise and cross stream pressure gradients. Downstream of the jet orifice there is an adverse pressure gradient (i.e. a localized blockage) while areas between the jets are subjected to a favorable pressure gradient that is induced by the low pressure created by the interaction of the streamwise vortices with the surface. These effects appear to constitute a local change in the “apparent” shape of the airfoil that mitigates the adverse pressure gradient in the baseline flow and promotes attachment.

Active flow control was also tested on a high-lift airfoil based on a commercial aircraft configuration containing a Fowler flap (with a cross-stream gap between the main element and the flap), in which a nominally 2-D cove jet, driven by the flow on the pressure side of the airfoil, forms in the gap and interacts with the flow over the surface of the flap and with the boundary layer of the main element. When the scale of the cross-stream gap is sufficiently small ($\gamma/c = 0.5\%$), the flow through the cove can lead to increased flow attachment on the flap with an increase in overall lift (even in the absence of active flow control). However, the cove flow does not have sufficient momentum to overcome the adverse pressure gradient over the entire surface of the flap. Because the jet is driven by the flow on the pressure surface of the main element, decreasing the jet width reduces its momentum. These interactions of the flow through the cove with the main element boundary layer and the surface of the flap indicate that a control jet close to the surface having sufficient momentum may be able to improve flow attachment on the flap over a greater streamwise extent. Because such a control jet functions independently of the flow through the cross-stream gap, it can also be effective in the absence of a cross-stream gap (i.e. a simple flap), for which separation occurs near the flap shoulder.

The incorporation of active flow control near the leading edge of the flap provides an alternate mechanism for improving flow attachment that does not rely on the presence of a cross-stream gap, and allows comparable (or better) high-lift performance to be achieved, even in the absence of a gap. The fluidic actuators function by engendering concentrations of streamwise vorticity in the boundary layer that induce suction near the juncture between the main element and the flap, altering the “apparent” shape of the surface. These effects lead to a reduction in the extent of flow separation and increased suction and lift that compare to what was shown using the simple flap configurations.

The maximum lift obtained with the configuration containing the Fowler flap using fluidic actuation in the absence of the cross-stream gap ($\gamma/c = 0$) is $C_L = 2.83$ ($C_\mu = 1.3\%$, $\delta = 60°$), in comparison to a maximum $C_L = 2.37$ ($\delta = 54°$) for the baseline airfoil. The effects of varying the spanwise wavelength of the actuation $\lambda$, i.e. the spanwise spacing between actuator jets, on the aerodynamic performance were investigated in the absence of the cross-stream gap. By reducing the number of active jets, $\lambda/c$ was increased from 0.015 to 0.079 while the same $C_\mu$ was maintained by adjusting the mass flow rate through the actuators. These measurements indicate that the aerodynamic performance of the actuation is only mildly sensitive to the spanwise wavelength as long as the same $C_\mu$ is be maintained. In fact, the data suggest that the performance at higher spanwise wavelengths may be matched at higher $C_\mu$ but at significantly lower actuation mass flow rate.

### *10.3. Discussion of Findings*

The processes through which active flow control can be employed in aerodynamic flows around airfoils to create and manipulate vorticity near the boundary layer, leading to significant changes in the airfoil aerodynamic characteristics, have been investigated in detail in this dissertation. In particular, it has been demonstrated that by using fluidic actuation to introduce small, localized concentrations of vorticity of opposing sense (emanating from the actuator orifice) into the flow adjacent to domain of flow separation, the size and scale of the separation can be reduced, or even eliminated entirely. In turn, altering the size and scale of separation, whether in a larger-scale separated flow or in a trapped vorticity concentration within a predominantly non-separated flow, alters the global flow field around the entire airfoil. Changes in the pressure distribution around the airfoil occur as a result, along with changes in the aerodynamic characteristics including lift, drag and pitching moment.

One key focus of the investigation has been on the mechanism through which active flow control actuation alters the scale of trapped vorticity concentrations within a predominantly attached aerodynamic flow. Flow control actuation (implemented using downstream-oriented synthetic jet actuators) generates a counterrotating vortex pair which emanates from the jet orifice toward the vorticity concentration. The half of the vortex pair having opposite sense to the boundary layer is convected downstream, while the half of the pair having the same sense as the boundary layer remains bound to the airfoil surface immediately downstream of the actuator, turning the boundary layer toward the airfoil surface. This process reduces the scale of the trapped vorticity concentration and re-directs higher-momentum flow from outside the boundary layer toward the wall, leading to changes in the flow around the entire airfoil.

The effects on the global flow field that result from fluidic alteration of trapped vorticity concentrations were studied in detail. It is shown how aerodynamic control can be achieved in the absence of moving control surfaces and how aerodynamic performance can be improved, enabling the possibility of simplifying (or even eliminating) mechanical aerodynamic control devices. Manipulation of trapped vorticity near the leading edge alters the characteristics of the airfoil boundary layer such that drag is reduced. In particular, higher-momentum fluid is re-directed toward the airfoil surface, resulting in a narrower wake and hence reduced pressure drag. By manipulating trapped vorticity concentrations near the trailing edge, the flow near the trailing edge can be turned upward or downward, leading to changes in the airfoil pressure distribution near the trailing edge and corresponding changes to the pitching moment in addition to reducing drag. It is noteworthy that, in the presence of multiple vorticity concentrations, manipulation of one vorticity concentration has no significant effect on other vorticity concentrations while simultaneously altering the global flow.

Optimization of the active flow control configuration to minimize the actuation authority required to change the airfoil aerodynamic characteristics has also been investigated. Actuation is most effective when the jet orifice is located near separation, whether the separated domain is small (i.e. a trapped vorticity concentration) or large-scale. The actuation momentum required for a given aerodynamic effect can be reduced when the actuation is coupled to the instability of the near wake, as demonstrated using synthetic jet actuation with a pulse-modulated driving waveform. It is also found that the aerodynamic effects of active flow control can be maximized by varying the spacing of the actuator jets, which influences how the vortex pairs that form near the actuator orifice interact with the surrounding flow.

Significant insight has been gained into the process through which active flow control can be used to reduce the extent of larger-scale separation in aerodynamic flows. A spanwise array of three-dimensional wall jets (issuing from nominally-square orifices having a length scale comparable to the boundary layer thickness) is created using active flow control and injected into the airfoil boundary layer immediately upstream of a large separated flow domain. The interaction of an actuator jet with the wall leads to a nonuniform distribution of Reynolds stresses within the jet, causing concentrations of streamwise vorticity to form in a process described by Craft and Launder (2001). The streamwise vortices turn the flow toward the wall near the jet centerline, directing higher-momentum fluid from outside the boundary layer toward the wall, and hence toward the separated flow. By this process the extent of separation can be diminished substantially.

Significant aerodynamic effects can be achieved as a consequence of mitigating (or eliminating) large-scale separation, as demonstrated using an airfoil in a high-lift configuration. Reducing the extent of separation over the suction surface of the deployed flap reduces blockage on the suction surface, resulting in increased suction and hence greater circulation and lift. These effects are manifested by a strengthened suction peak near the leading edge of the flap as well as a reduced airfoil wake width. As a result, a substantial improvement in high-lift performance is realized that allows for a significant simplification of the design of aircraft high-lift systems. In particular, it was shown how similar high-lift performance to an optimized Fowler flap (with a cross-stream gap between elements) can be achieved in the *absence* of a gap through the use of active flow control near the juncture between the elements. Finally, the effects of synthetic jet actuation have been shown to be comparable to the effects of a similarly configured array of fluidic oscillators, though higher $C_\mu$ is required.

### 10.4. Recommendations for Future Work

Based on the findings of this dissertation, further investigation is warranted into the process through which the introduction of streamwise vorticity from active flow control actuation into the airfoil boundary layer causes an adjacent large-scale separation domain to be diminished. In particular, it is desirable to investigate how the scale and spacing of the streamwise vorticity pairs for various upstream boundary layer conditions affects the effectiveness of the flow control actuation, as well as to identify the physical mechanisms associated with the actuation and its effects. Since the streamwise vorticity diminishes a short distance from the actuator orifice (which is believed to occur due to vortex bursting), it is also desirable to investigate the effectiveness of alternate actuation configurations where streamwise vorticity is present over a greater extent of the airfoil surface.

In consideration of the aerodynamic performance improvements demonstrated on a high-lift airfoil with a Fowler flap, alternate high-lift geometries employing active flow control are another potential future research topic. Because it has been shown how active flow control can be employed to eliminate the cross-stream gap between elements with no loss in high-lift performance, it is worth investigating the possibility of using active flow control to achieve comparable (or better) high-lift performance using a mechanically simplified high-lift system, i.e. a simple flap rotating about a fixed hinge point, that does not require a cross-stream gap and can operate at larger flap deflections. Such simplification of a high-lift system can lead to substantial reductions in weight, complexity, part count and fabrication and operation costs.

Future work may also concern whether the use of active flow control based on streamwise vorticity is effective at manipulating predominantly attached aerodynamic flows. Because it has been found that streamwise vorticity is formed as a result of the interaction of an actuator jet with the adjacent wall and not necessarily due to interaction with the nearby separated flow, it is worth investigating whether active flow control based on streamwise vorticity is effective in the absence of separation at convecting higher-momentum fluid from outside the boundary layer toward the wall. Such an active flow control technique could enable aerodynamic control to be accomplished without the use of surface obstructions (and the resulting local separation that occurs as a result) because streamwise vorticity-based actuators are mounted below the airfoil surface.

# APPENDIX A

# MEASUREMENT LOCATIONS

Listed in this section are the (*x/c*, *y/c*) coordinates of the pressure ports and skin friction measurement locations on the swept model (Tables A.1 and A.2, respectively), the coordinates of the main element and flap pressure ports on the ADVINT model (Tables A.3 and A.4, respectively), and the coordinates of the main element and flap pressure ports on the MD 30P-30N model (Tables A.5 and A.6, respectively). All measurements are taken on the spanwise centerline of the model.

***Table A.1.*** *Swept airfoil model pressure port locations.*

| *x/c* | *y/c* | *x/c* | *y/c* | *x/c* | *y/c* |
|---|---|---|---|---|---|
| 1.000 | 0.000 | 0.228 | 0.059 | 0.224 | -0.035 |
| 0.980 | 0.006 | 0.204 | 0.057 | 0.251 | -0.037 |
| 0.952 | 0.012 | 0.182 | 0.055 | 0.279 | -0.039 |
| 0.919 | 0.020 | 0.162 | 0.052 | 0.310 | -0.041 |
| 0.879 | 0.028 | 0.143 | 0.050 | 0.343 | -0.042 |
| 0.836 | 0.035 | 0.125 | 0.047 | 0.383 | -0.042 |
| 0.790 | 0.042 | 0.108 | 0.044 | 0.421 | -0.042 |
| 0.748 | 0.047 | 0.092 | 0.041 | 0.457 | -0.041 |
| 0.706 | 0.052 | 0.077 | 0.038 | 0.497 | -0.040 |
| 0.661 | 0.056 | 0.062 | 0.034 | 0.538 | -0.038 |
| 0.618 | 0.059 | 0.048 | 0.030 | 0.578 | -0.035 |
| 0.576 | 0.061 | 0.022 | 0.019 | 0.619 | -0.031 |
| 0.497 | 0.064 | 0.000 | 0.000 | 0.657 | -0.027 |
| 0.459 | 0.065 | 0.011 | -0.009 | 0.698 | -0.023 |
| 0.421 | 0.065 | 0.039 | -0.016 | 0.739 | -0.018 |
| 0.383 | 0.065 | 0.068 | -0.019 | 0.822 | -0.009 |
| 0.347 | 0.065 | 0.133 | -0.027 | 0.854 | -0.006 |
| 0.312 | 0.064 | 0.152 | -0.029 | 0.885 | -0.004 |
| 0.282 | 0.063 | 0.171 | -0.031 | 0.963 | -0.001 |
| 0.254 | 0.061 | 0.199 | -0.033 | 0.977 | -0.001 |

***Table A.2.*** *Swept airfoil model skin friction measurement locations.*

| *x/c* | *y/c* | *x/c* | *y/c* | *x/c* | *y/c* |
|---|---|---|---|---|---|
| 0.980 | 0.011 | 0.228 | 0.064 | 0.467 | -0.046 |
| 0.879 | 0.033 | 0.092 | 0.046 | 0.624 | -0.036 |
| 0.743 | 0.053 | 0.046 | -0.022 | 0.739 | -0.023 |
| 0.661 | 0.061 | 0.150 | -0.033 | 0.832 | -0.013 |
| 0.532 | 0.068 | 0.253 | -0.042 | 0.910 | -0.007 |
| 0.383 | 0.070 | 0.343 | -0.047 | 0.990 | -0.006 |

***Table A.3.*** *ADVINT model main element pressure ports.*

| *x/c* | *y/c* | *x/c* | *y/c* | *x/c* | *y/c* |
|---|---|---|---|---|---|
| 0.584 | -0.049 | 0.044 | -0.033 | 0.115 | 0.076 |
| 0.553 | -0.052 | 0.029 | -0.028 | 0.150 | 0.082 |
| 0.521 | -0.056 | 0.017 | -0.022 | 0.192 | 0.088 |
| 0.488 | -0.059 | 0.008 | -0.015 | 0.243 | 0.092 |
| 0.452 | -0.061 | 0.003 | -0.008 | 0.303 | 0.096 |
| 0.415 | -0.062 | 0.000 | -0.002 | 0.348 | 0.097 |
| 0.376 | -0.063 | 0.000 | 0.006 | 0.391 | 0.097 |
| 0.335 | -0.063 | 0.002 | 0.012 | 0.431 | 0.097 |
| 0.292 | -0.062 | 0.006 | 0.020 | 0.470 | 0.096 |
| 0.234 | -0.060 | 0.011 | 0.028 | 0.506 | 0.094 |
| 0.186 | -0.056 | 0.019 | 0.036 | 0.541 | 0.091 |
| 0.146 | -0.053 | 0.030 | 0.045 | 0.574 | 0.088 |
| 0.113 | -0.048 | 0.045 | 0.054 | 0.606 | 0.085 |
| 0.085 | -0.044 | 0.063 | 0.062 | | |
| 0.062 | -0.039 | 0.087 | 0.070 | | |

***Table A.4.*** *ADVINT model flap pressure ports. Flap is deflected to angle $\delta$ by rotation about (x/c, y/c) = (0.6495, -0.0135) and ports within outer mold line are not used.*

| *x/c* | *y/c* | *x/c* | *y/c* | *x/c* | *y/c* |
|---|---|---|---|---|---|
| 0.616 | -0.040 | 0.957 | 0.003 | 0.642 | 0.077 |
| 0.640 | -0.040 | 0.969 | 0.008 | 0.614 | 0.070 |
| 0.668 | -0.036 | 0.944 | 0.014 | 0.594 | 0.059 |
| 0.702 | -0.030 | 0.911 | 0.022 | 0.580 | 0.045 |
| 0.742 | -0.023 | 0.877 | 0.030 | 0.571 | 0.032 |
| 0.786 | -0.016 | 0.840 | 0.039 | 0.565 | 0.020 |
| 0.827 | -0.009 | 0.802 | 0.048 | 0.561 | 0.009 |
| 0.866 | -0.003 | 0.762 | 0.057 | 0.560 | 0.000 |
| 0.903 | 0.001 | 0.715 | 0.067 | | |
| 0.939 | 0.003 | 0.675 | 0.074 | | |

***Table A.5.*** *MD 30P-30N main element pressure ports.*

| x/c | y/c | x/c | y/c | x/c | y/c |
|---|---|---|---|---|---|
| 0.832 | 0.038 | 0.075 | 0.029 | 0.119 | -0.042 |
| 0.766 | 0.046 | 0.053 | 0.020 | 0.175 | -0.047 |
| 0.704 | 0.052 | 0.031 | 0.007 | 0.294 | -0.054 |
| 0.625 | 0.057 | 0.012 | -0.009 | 0.414 | -0.054 |
| 0.554 | 0.060 | 0.001 | -0.024 | 0.535 | -0.044 |
| 0.397 | 0.061 | 0.000 | -0.032 | 0.641 | -0.028 |
| 0.297 | 0.058 | 0.000 | -0.039 | 0.700 | -0.004 |
| 0.197 | 0.052 | 0.004 | -0.048 | 0.700 | 0.022 |
| 0.161 | 0.048 | 0.018 | -0.050 | 0.757 | 0.031 |
| 0.127 | 0.044 | 0.038 | -0.048 | | |
| 0.099 | 0.037 | 0.080 | -0.042 | | |

***Table A.6.*** *MD 30P-30N flap pressure ports (Fowler flap, $\delta = 25^o$ and $\gamma/c = 0$).*

| x/c | y/c | x/c | y/c | x/c | y/c |
|---|---|---|---|---|---|
| 1.139 | -0.116 | 0.902 | 0.028 | 0.882 | -0.007 |
| 1.135 | -0.110 | 0.895 | 0.029 | 0.903 | -0.016 |
| 1.122 | -0.097 | 0.887 | 0.028 | 0.950 | -0.029 |
| 1.097 | -0.078 | 0.880 | 0.027 | 1.004 | -0.047 |
| 1.065 | -0.053 | 0.874 | 0.023 | 1.062 | -0.072 |
| 1.023 | -0.024 | 0.870 | 0.017 | 1.102 | -0.094 |
| 0.974 | 0.004 | 0.869 | 0.010 | 1.127 | -0.110 |
| 0.928 | 0.022 | 0.873 | 0.001 | | |

# REFERENCES

Abbott, I. and von Doenhoff, A., *Theory of Wing Sections*, Dover Publications Inc., New York, 1959.

Ahuja, K. K. and Burrin, R. H., "Control of Flow Separation by Sound," AIAA 84-2298, Oct. 1984.

Amitay, M. and Glezer, A., "Role of Actuation Frequency in Controlled Flow Reattachment over a Stalled Airfoil," *AIAA Journal*, Vol. 40, pp. 209-216, February 2002.

Amitay M. and Glezer, A., "Controlled Transients of Flow Reattachment over Stalled Airfoils," *International Journal of Heat and Fluid Flow*, Vol. 23, No. 5, pp. 690-699, October 2002.

Amitay, M. and Glezer, A., "Flow Transients Induced on a 2-D Airfoil by Pulse-Modulated Actuation," *Experiments in Fluids*, Vol. 40, pp. 329-331, February 2006.

Amitay, M., Horvath, M. Michaux, M. and Glezer, A., "Virtual Aerodynamic Shape Modification at Low Angles of Attack using Synthetic Jet Actuators," AIAA 2001-2975, June 2001.

Amitay, M., Smith, B. L. and Glezer, A. "Aerodynamic Flow Control using Synthetic Jet Technology," AIAA 98-0208, January 1998.

Bower, W. and Kibens, V., "An Overview of Active Flow Control Applications at the Boeing Company," AIAA 2004-2624, June 2004.

Carrannanto, P., Storms, B., Ross, J. and Cummings, R., "Navier-Stokes Analysis of Lift-Enhancing Tabs on Multi-Element Airfoils," *Aircraft Design*, Vol. 1, No. 3, pp. 145-158, September 1998.

Cater, J. E. and Soria, J., "The Evolution of Round Zero-Net-Mass-Flux Jets," *Journal of. Fluid Mechanics*, Vol. 472, pp. 167-200, December 2002.

Cattafesta, L. and Sheplak, M., "Actuators for Active Flow Control," *Annual Review of Fluid Mechanics*, Vol. 43, pp. 247-272, January 2011.

Cerretelli, C., Gharaibah, E., Toplack, G., Gupta, A. and Wuerz, W., "Unsteady Separation Control for Wind Turbine Applications at Full Scale Reynolds Number," AIAA 2009-0380, January 2009.

Cerretelli, C. and Kirtley, K., "Boundary Layer Separation Control with Fluidic Oscillators," *Journal of Turbomachinery*, Vol. 131, No. 4, pp. 1-9, Oct. 2009.

Chang, P. K., *Control of Flow Separation*. McGraw-Hill, New York, 1976.

Chatlynne, E., Rumigny, N., Amitay, M. and Glezer, A., "Virtual Aero-Shaping of a Clark-Y Airfoil using Synthetic Jet Actuators," AIAA 2001-0732, Jan. 2001.

Ciobaca, V., Kühn, T., Rudnik, R., Bauer, B., Gölling, B. and Breitenstein, W., "Active Flow-Separation Control on a High-Lift Wing-Body Configuration," *Journal of Aircraft,* Vol. 50, No. 1, pp. 56-72, Feb. 2013.

Clauser, F. H., "Turbulent Boundary Layers in Adverse Pressure Gradients," *Journal of the Aeronautical Sciences,* Vol. 21, No. 2, pp. 91-108, February 1954.

Craft, T. J. and Launder, B. E., "On the Spreading Mechanism of the Three-Dimensional Turbulent Wall Jet," *Journal of Fluid Mechanics,* Vol. 435, pp. 305-326, May 2001.

Crowther, W., "Separation Control on a Trailing-Edge Flap Using Air Jet Vortex Generators," *Journal of Aircraft,* Vol. 43, No. 5, pp. 1589-1593, September 2006.

DeSalvo, M., Amitay, M. and Glezer, A., "Modification of the Aerodynamic Performance of Airfoils at Low Angles of Attack: Trailing Edge Trapped Vortices," AIAA 2002-3165, June 2002.

DeSalvo, M. and Glezer, A., "Aerodynamic Performance Modification at Low Angles of Attack by Trailing Edge Vortices," AIAA 2004-2118, June 2004.

DeSalvo, M. and Glezer, A., "Airfoil Aerodynamic Performance Modification using Hybrid Surface Actuators," AIAA 2005-0872, Jan. 2005.

DeSalvo, M. and Glezer, A., "Aerodynamic Control at Low Angles of Attack using Trapped Vorticity Concentrations," AIAA 2006-0100, Jan. 2006.

DeSalvo, M. and Glezer, A., "Control of Airfoil Aerodynamic Performance using Distributed Trapped Vorticity," AIAA 2007-0708, Jan. 2007.

DeSalvo, M., Whalen, E. and Glezer, A., "High-Lift Enhancement using Fluidic Actuation," AIAA 2010-0863, January 2010.

DeSalvo, M., Whalen, E. and Glezer, A., "Enhancement of a High-Lift Airfoil using Low-Power Fluidic Actuators," AIAA 2010-4248, June 2010.

DeSalvo, M., Whalen, E. and Glezer, A., "High-lift Enhancement Using Active Flow Control," AIAA 2011-3355, June 2011.

DeSalvo, M., Whalen, E. and Glezer, A., "High-Lift Enhancement using Active Flow Control," AIAA 2012-3245, June 2012.

DeSalvo, M., Whalen, E. and Glezer, A., "Enhancement of a Fowler Flap High-Lift System using Active Flow Control," AIAA 2014-0198, January 2014.

Gad-el-Hak, M.. "Flow Control: The Future," *Journal of Aircraft,* Vol. 38, No. 3, pp. 402-418, May-June 2001.

Gilarranz, J. L., Traub, L. W. and Rediniotis, O. K., "A New Class of Synthetic Jet Actuators – Part II: Application to Flow Separation Control," *Journal of Fluids Engineering,* Vol. 127, pp. 377-387, March 2005.

Glezer, A., "Some Aspects of Aerodynamic Flow Control using Synthetic Jet Actuation," *Philosophical Transactions of the Royal Society A,* Vol. 369, pp. 1476-1494, April 2011.

Glezer, A. and Amitay, M., "Synthetic Jets," *Annual Review of Fluid Mechanics,* Vol. 34, pp. 503-529, January 2002.

Glezer, A., Amitay, M. and Honohan, A., “Aspects of Low- and High-Frequency Actuation for Aerodynamic Flow Control,” *AIAA Journal,* Vol. 43, No. 7, pp. 1501-1511, July 2005.

Gokoglu, S., Kuczmarski, M., Culley, D. and Raghu, S., “Numerical Studies of a Fluidic Diverter for Flow Control,” AIAA 2009-4012, June 2009.

Gomes, L., Crowther, W. and Wood, N., “Towards a Practical Synthetic Jet Actuator for Industrial Scale Flow Control Applications,” IUTAM Symposium on Flow Control and MEMS: Proceedings of the IUTAM Symposium Held at the Royal Geographical Society, September 2006.

Greenblatt, D., “Managing Flap Vortices via Separation Control,” *AIAA Journal,* Vol. 44, pp. 2755–2764, November 2006.

Greenblatt, D. and Wygnanski, I. J., “Use of Periodic Excitation to Enhance Airfoil Performance at Low Reynolds Numbers,” *Journal of Aircraft*, Vol. 38, pp. 190-192, January-February 2001.

Gregory, J., Sullivan, J., Raman, G. and Raghu, S., “Characterization of the Microfluidic Oscillator,” *AIAA Journal,* Vol. 45, No. 3, pp. 568-576, March 2007.

Honohan, A. M. “The Interaction of Synthetic Jets with Cross Flow and the Modification of Aerodynamic Surfaces,” Ph.D. Dissertation, Georgia Institute of Technology, April 2003.

Honohan, A. M., Amitay, M. and Glezer, A., “Aerodynamic Control using Synthetic Jets,” AIAA 2000-2401, June 2000.

Hsiao, F.-B., Liu, C. F., and Shyu, J. Y., “Control of Wall-Separated Flow by Internal Acoustic Excitation,”. *AIAA Journal,* Vol. 28, pp. 1440-1446, August 1990.

Hurley, D. G., “The Use of Boundary Layer Control to Establish Free Stream Line Flows,” *Advances in Aeronautical Scences,* Vol. 2, Pergamon Press, New York, pp. 662-708, 1959.

Khodadoust, A., andWashburn, A., “Active Control of Flow Separation on a High-Lift System with Slotted Flap at High Reynolds Number,” AIAA 2007-4424, June 2007.

Kim, S. H. and Kim, C., “Separation Control on NACA23012 Using Synthetic Jet,” AIAA 2006-2853, June 2006.

Kotapati, R., Mittal, R. and Cattafesta, L., “Numerical Study of a Transitional Synthetic Jet in Quiescent External Flow,” *Journal of Fluid Mechanics*, Vol. 581, pp. 287-321, June 2007.

Launder, B. E. and Rodi, W., “The Turbulent Wall Jet – Measurements and Modeling,” *Annual Review of Fluid Mechanics,* Vol. 15, pp. 429-459, January 1983.

Lee, C. Y. and Goldstein, D. B., “Two-Dimensional Synthetic Jet Simulation,” *AIAA Journal,* Vol. 40, No. 3, pp. 510–516, March 2002.

Margalit, S., Greenblatt, D., Seifert, A., and Wygnanski, I., “Delta Wing Stall and Roll Control using Segmented Piezoelectric Fluidic Actuators,” *Journal of Aircraft,* Vol. 42, pp. 698-709, May-June 2005.

McLean, J.D., Crouch, J.D., Stoner, R.C., Sakurai, S. and Seidel, G.E., "Study of the Application of Separation Control by Unsteady Excitation to Civil Transport Aircraft," NASA/CR-1999-209338, June 1999.

Mittal, R. and Rampunggoon, P., "On the Virtual Aeroshaping Effect of Synthetic Jets," *Physics of Fluids,* Vol. 14, pp. 1533-1536, April 2002.

Nagib, H., Kiedaisch, J., Reinhard, P. and Demanett, B., "Control Techniques for Flows with Large Separated Regions: A New Look at Scaling Parameters," AIAA 2006-2857, June 2006.

Newman, B. G., Patel, R. P., Savage, S. B. and Tjio, H. K., "Three-Dimensional Wall Jet Originating from a Circular Orifice," *Aeronautical Quarterly,* Vol. 23, Part 3, pp. 188-200, August 1972.

Nishri, B. and Wygnanski, I., "Effects of Periodic Excitation on Turbulent Flow Separation from a Flap," *AIAA Journal,* Vol. 36, No. 4, pp. 547-556, April 1998.

Perkins, C. D. and Hazen, D., "Some Recent Advances in Boundary Layer and Circulation Control," *Fourth Anglo-American Aeronautical Conference,* Royal Aeronautical Society, London, pp. 189-224, 1953.

Raju, R., Mittal, R. and Cattafesta, L., "Dynamics of Airfoil Separation Control using Zero-Net-Mass-Flux Forcing," *AIAA Journal,* Vol. 46, pp. 3103-3115, December 2008.

Raman, G., Raghu, S. and Bencic, T., "Cavity Resonance Suppression using Miniature Fluidic Oscillators," AIAA 99-1900, May 1999.

Rehman, A. and Kontis, K., "Synthetic Jet Control Effectiveness on Stationary and Pitching Airfoils," *Journal of Aircraft,* Vol. 43, pp. 1782-1789, November-December 2006.

Ringleb, F. O., "Separation Control by Trapped Vortices," *Boundary Layer Flow Control, Vol. I,* G. V. Lachmann, editor, Pergamon Press, New York, pp. 265-294, 1961.

Rizzetta, D. P., Visbal, M. R. and Stanek, M. J., "Numerical Investigation of Synthetic-Jet Flow Fields," *AIAA Journal,* Vol. 37**,** No. 8, pp. 919–927, August 1999.

Scarano, F. and Riethmuller, M. L., "Advances in Iterative Multigrid PIV Image Processing," *Experiments in Fluids,* Vol. 29, No. 1 Supplement, pp. S051-S060, December 2000.

Schatz, M., Thiele, F., Petz, R. and Nitsche, W., "Separation Control by Periodic Excitation and its Application to a High-Lift Configuration," AIAA 2004-2507, June 2004.

Seele, R., Graff, E., Lin, J. and Wygnanski, I., "Performance Enhancement of a Vertical Tail Model with Sweeping Jet Actuators," AIAA 2013-0411, January 2013.

Seele, R., Tewes, P., Woszidlo, R., McVeigh, M., Lucas, N. and Wygnanski, I., "Discrete Sweep Jets as Tools for Improving the Performance of the V-22," *Journal of Aircraft,* Vol. 46, No. 6, pp. 2098-2106, November 2009.

Seifert, A., Bachar, T., Koss, D., Shepshelovich, M., and Wygnanski, I., "Oscillatory Blowing: A Tool to Delay Boundary Layer Separation," *AIAA Journal,* Vol. 31, pp. 2052-2060, November 1993.

Seifert, A., Darabi, A. and Wygnanski, I., "Delay of Airfoil Stall by Periodic Excitation," *Journal of Aircraft*, Vol. 33, No. 4, pp. 691-698, July 1996.

Shmilovich, A. and Yadlin, Y., "Flow Control for the Systematic Buildup of High Lift Systems," AIAA 2006-2855, June 2006.

Shmilovich, A., and Yadlin, Y., "Active Flow Control for Practical High-Lift Systems," *Journal of Aircraft*, Vol. 46, No. 4, pp. 1354–1364, Aug. 2009.

Shuster, J. M. and Smith, D. R., "Experimental Study of the Formation and Scaling of a Round Synthetic Jet," *Physics of Fluids*, Vol. 19, pp. 045109, April 2007.

Smith, A. M. O., "High-Lift Aerodynamics," *Journal of Aircraft*, Vol. 12, No. 6, pp. 501-530, June 1975.

Smith, B. L. and Glezer A., "The Formation and Evolution of Synthetic Jets," *Physics of Fluids*, Vol. 10, pp. 2281-2297, September 1998.

Smith, D.M., Dickey, E. and VonKlein, T., "The ADVINT Program," AIAA 2006-2854, June 2006.

Timor, I., Ben-Hamou, E., Guy, Y. and Seifert, A., "Maneuvering Aspects and 3-D Effects of Active Airfoil Flow Control," AIAA 2004-2614, June 2004.

Viets, H., "Flip-Flop Jet Nozzle," *AIAA Journal*, Vol. 13, No. 10, pp. 1375-1379, October 1975.

Watson, M., Jaworski, A. J. and Wood, N. J., "Application of Synthetic Jet Actuators for the Modification of the Characteristics of Separated Shear Layers on Slender Wings," *Aeronautical Journal*, Vol. 111, pp. 519-530, August 2007.

Woszidlo, R., Nawroth, H., Raghu, S. and Wygnanski, I., "Parametric Study of Sweeping Jet Actuators for Separation Control," AIAA 2010-4247, June 2010.

Wu, J.–Z., Lu, X.-Y., Denny, A. G., Fan, M. and Wu, J.-M., "Post Stall Flow Control on an Airfoil by Local Unsteady Forcing," *Journal of Fluid Mechanics*, Vol. 371, pp. 21-58, September 1998.

Yao, C. S., Chen, F. J., and Neuhart, D., "Synthetic Jet Flowfield Database for Computational Fluid Dynamics Validation," *AIAA J*ournal, Vol. 44, No. 12, pp. 3153-3157, December 2006.

You, D., Ham, F. and Moin, P., "Discrete Conservation Principles in Large-Eddy Simulation with Application to Separation Control over an Airfoil," *Physics of Fluids*, Vol. 20, 101515, October 2008.

# VITA

Michael Edward DeSalvo was born in Creve Coeur, MO. He grew up in Marrero, LA, and attended Isidore Newman School in New Orleans, LA. He attended the California Institute of Technology, Pasadena, CA, graduating with a B.S. in Engineering and Applied Science in 2001. Subsequently, he moved to Georgia Tech, and received a M.S. in Mechanical Engineering in 2003 before pursuing a doctorate in Mechanical Engineering. Since 2008, he has continued to be employed at Georgia Tech in the Fluid Mechanics Research Laboratory. When he is not working on research, DeSalvo enjoys working on his converted electric-powered pickup truck.